Date of Report: <December 20, 2018>

Contract Number: <DTPH56-15-H-CAAP06>

Prepared for: <Government Agency: U. S. DOT PHMSA >

Project Title: <Mitigating Pipeline Corrosion Using A Smart Thermal Spraying Coating System>

Prepared by: <North Dakota State University>

Contact Information: <Dr. Fardad Azarmi, Email: fardad.azarmi@ndsu.edu, Phone: 701.231.9784; Dr. Ying Huang, Email: ying.huang@ndsu.edu, Phone: 701.231.7651.>

For CAAP Final Report period ending: <*December 31, 2018*>

Business and Activity Section

(a) Generated Commitments

No changes to the existing agreement.

No equipment purchased over this reporting period.

No materials purchased during this reporting period:

(b) Draft Final Report

1 Introduction (Task 1, Completed)

1.1 Coating Techniques for Corrosion Mitigation

Deposition of a protective coating (soft or hard) has been recoganized as a major method for corrosion prevention and mitigation in pipeline industry. Two major coating materials were widely produced to assist corrosion mitigation for steel pipes as followings,

1.1.1 Polymeric Coatings

Polymer based coatings showed good performances on corrosion mitigation by separating the metal pipes from the surrounding corrosive environments. Polymeric coatings using coal tar[1] were applied to pipelines before 1970s. However, since the coal tar coatings were not environmental friendly and difficult to apply in practice, they were replaced by Solid Rigid Polyurethane (SRP) coatings[2] after 1970s. The SRP coatings provided relatively safer, faster, stronger, and easier to apply coatings, but thin SRP layers may fail at long-term service. Therefore, thicker layered polymer based coatings were developed in 1990s using polychloroprene[3], Fusion-Bonded Epoxy-(FBE)[4], and 3-layer-polyurethane (3LPE) [5]. Combined with concrete, the FBE or 3LPE coatings were widely deployed in off-shore pipeline industry. Although mitigate corrosion effectively, these thick polymer coatings have a high cost and high potential for initial defects in the polymer layer. These initial defects would degrade over

time and fail the corrosion protection of the coating. These limitations of polymeric coatings open potentials for the development of metallic coatings.

1.1.2 Metallic Coatings

Metallic coatings deposited by thermal spraying techniques have already exhibited excellent corrosion protection in advanced manufacturing such as electronics and aerospace[6]. Gaining interests in thermal spraying of metallic coatings were expanded to the corrosion mitigation for off-shore pipelines [7, 8] and successfully applied to waste related structures such as Mormon Flat dam[9, 10]. The thermally sprayed metallic coatings can act both as cathodic protection and separation layer. The cathodic measures of these metallic coating drastically reduced the dependence on external supplemental anodes. In addition, the thermal sprayed metallic coating could also significantly enhance the service time of the pipelines in harsh environments. Although the equipment for thermal spraying seems to be expensive, in long term, the high performance of the developed coating makes this process to be a cost-effective corrosion mitigation method. Generally, the thermally sprayed coatings have shown better protection and longevity compared to the other traditional coating technology. Although under development by this research team[11], more investigations on thermal sprayed coatings to effectively mitigate the onshore buried pipelines are still in great needs before their potential field applications.

1.2 Mechanism of Corrosion on Buried Pipeline

Several types of corrosion can occur in buried steel pipelines including bimetallic corrosion, general corrosion, pitting corrosion, hydrogen embrittlement, and stress corrosion cracking (SCC). The most common corrosion mechanism in buried pipelines is galvanic corrosion (bimetallic corrosion) and hydrogen embrittlement which requires special attention.

1.2.1 Galvanic Corrosion

Bimetallic corrosion occurs when two metals, with different potentials are in electrical contact while immersed in an electrically conducting corrosive environment[12, 13]. The basic requirements to initiate bimetallic corrosion are an electrolyte bridging the two metals, electrical connection between the two metals, a sufficient difference in potential between the two metals to provide galvanic current, and a sustained cathodic reaction. In the case bimetallic corrosion, the potential difference is created by the presence of dissimilar metals. Due to the dissimilar natural potentials, a current will flow from the anode (more electronegative) metal to the cathode (more electropositive) which will increase the corrosion on the anode. Since the materials of coating and the pipe could have dissimilar electronegativity, likelihood of the bimetallic corrosion should be considered during materials selection process. The schematic of the bimetallic corrosion is shown in Figure 1[14].

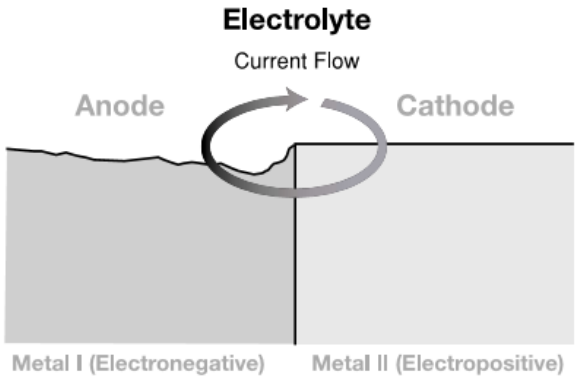

Figure.1. Bimetallic corrosion.[14]

In general, the formation and growth of corrosion cells are similar to uncoupled metals, but the rate of attack can drastically increase. An appropriate materials selection process can play an important role in maximize the service life of pipelines. In the case of using a coupled material (bimetallic) system, combination of some metals with different electronegativity can alter the total electrical balance of the system resulting in induce of corrosion that would not have occurred in the uncoupled state (e.g. pitting). List of the galvanic series is shown in Table 1. Although the ranking in this table was derived for seawater, it is very similar for many other near neutral aerated aqueous solutions.

Table. 1. List of galvanic series.[12]

Electro Positive	Graphite	
	Platinum	
	Gold	
	High Alloy Stainless Steels	(Super Austenitic) (Super Duplex)
	Titanium	
	Nickel Chrome Molybdenum Alloys	(625; C-276)
	Low alloy stainless steels (eg 316)	(PASSIVE)
	Alloy 400/Alloy K-500	
	Silver	
	Nickel Aluminium Bronze	
	Copper nickel (70/30; 90/10)	
	Gunmetals/Tin Bronzes	
	Brasses	
	Tin	
	Lead	
	Austenitic Cast Iron	
	Low alloy stainless steels (eg 316)	(ACTIVE)
	Cast Iron	
	Carbon Steel	
	Aluminium alloys	
Electro Negative	Zinc	
	Magnesium	

As shown in the Table 1, some materials like stainless steel (e.g. 316) have a thin protective layer (passive state) which maintains while the corrosion rate is very low. Figure 2 shows two different types of coatings that can be selected for steel pipes for providing anodic and cathodic protections[15]. In the first case no discontinuity in the coating can be tolerated, while it has no importance with cathodic coating, as illustrated in Figure 2. The coating material and its microstructure play an important role in this type of corrosion. Anodic coatings such as austenitic stainless steels, aluminum bronze, nickel-base alloys, super-alloys MCrAlY materials, Cermet (metal matrix re-enforced with WC), Cr2C3, and Ni or Co based composites are used against corrosion, often when it is associated with wear. However, such coatings, presenting no galvanic protection, will never protect the substrate if connected porosities and oxide networks exist, which is the case in most of thermal-sprayed coatings[16]. Therefore, the substrate protection requires using a protective bond coat or producing dense coatings, or sealing them.

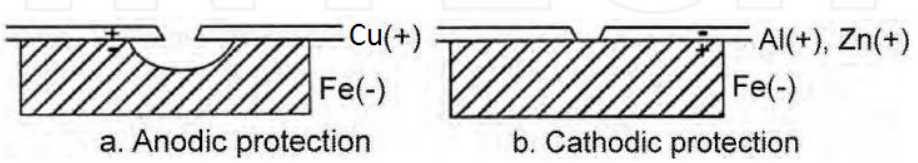

Figure 2. Examples of protective coatings; a) Anodic (no discontinuity possible in the coating), and b) Cathodic (discontinuity possible in the coating, resulting in no corrosion of iron).[15]

On the other hand, cathodic coatings acts like sacrificial anode due to their higher electronegativity respect to the steel. Hence, if the coating breaks and steel pipe be exposed to the corrosive environment, steel will act as cathode and remains un-corroded. In the case of coating steel for corrosion protection, it is recommended that the coating material with higher electronegativity state be selected. Thus, in this

case coating will act as sacrificial anode and will protect the steel pipe against corrosion. As sacrificial coatings (cathodic behavior relatively to ions, for example Zn or Al on steel): the thicker they are, the longer protection they provide (typical thickness varies between 50 and 500 µm, the most frequent one being around 230 µm)[15].

A general idea of the qualitative risk of bimetallic corrosion can be gained by putting these effects together into a form as shown in Figure 3. According to Figure 3, alloys that are coupled to metals with more electropositive potentials are the ones, which suffer bimetallic corrosion. In other words, to avoid motivation of the bimetallic corrosion of a metal, the couple with higher electronegativity should be selected. As it can be seen in Figure 3, coupling the steel with Zinc, Aluminum, and Magnesium will not increase the additional corrosion in steel. Using copper might slightly increase the chance of the additional corrosion in steel as its electronegativity is slightly lower than steel. However, copper proved to be much Nobel metal with higher stability in corrosive area once it is used alone (uncoupled).

Notwithstanding, the potential difference is not the sufficient factor to predict the risk of bimetallic corrosion, and it provides no information on the kinetic of bimetallic corrosion. There are some crucial factors including area ratio, temperature, flow rate, composition of the electrolyte, etc., which define if the bimetallic corrosion is possible for any combined metallic system[17]. For instance, it has been reported that in the case of magnesium and its alloys, even though they have higher electronegativity state compared to steel, there is a possibility of a significant amount of hydrogen evolution at the cathode in neutral solutions. This resulted in hydrogen embrittlement and disbanding of the coating and failure of the pipe[18].

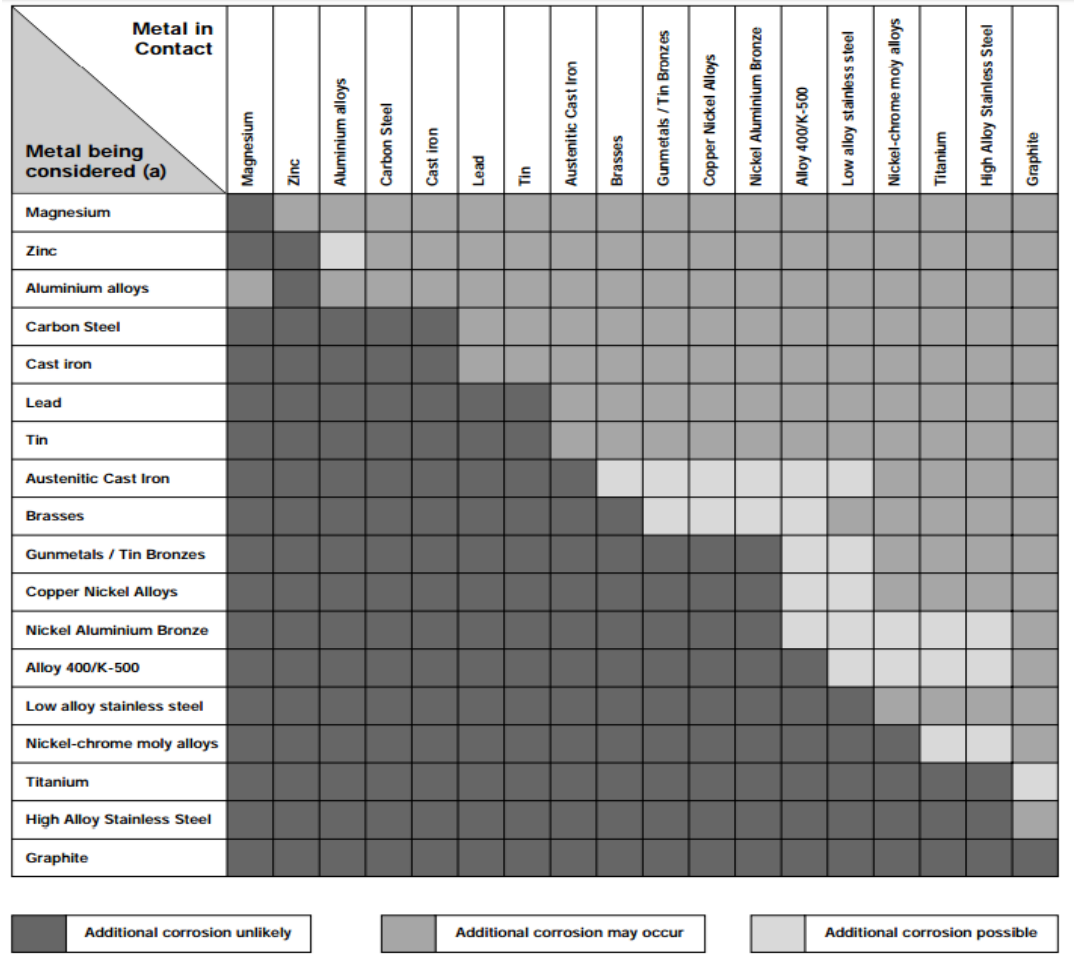

Figure 3. Risk of additional corrosion from bimetallic contact in neutral aqueous electrolytes.

1.2.2 Hydrogen embrittlement

Locally excessive cathodic protection potentials known as “overprotection” is possible to occur in a pipe with a large accumulation of external coating defects[19-23]. Overprotection in the CP system is generally contribute to two possible damages which are cathodic debinding and hydrogen-related damages to the pipeline body due to the production of hydroxide at the cathode and the release of hydrogen. The actual generation of hydrogen gas takes place only at fairly high-negative potentials but, under rare conditions, it could literally strip off a coating in a matter of hours whilst hydrogen production may cause hydrogen embrittlement in the carbon steel[24].

The important parameter that is required to be considered in materials selection is the change of potential due to exposure to some environments, which might introduce new problems including hydrogen embrittlement[24]. The effect of PH is even far-reaching and depends upon the composition of both metals forming the couple. For instance, by using magnesium and its alloys, considerable amount of hydrogen evolution at the cathode in neutral solution might cause failure. Hence, extra care is required for selecting a suitable material to avoid severe hydrogen evolution. One of the methods of preventing SCC on pipeline structures include minimizing the operation temperature and controlling the CP levels to values more negative than -850mV CSE[12]. The other method is selecting a material with lower possibility of hydrogen embrittlement. Metallic thin films can hinder hydrogen penetration into the metallic substrate by virtue of their low solubility, diffusivity, or surface effects involving adsorption of hydrogen or combination of these mechanism[25]. Pressouyer[25]compiled permeability data for hydrogen through a number of metals and compared these value to those for hydrogen through low alloy austenitic steels. a large number of these data were originally published by Tison et al. The summary of their results, in decreasing order of hydrogen permeability, are listed as follow: Nickel (Ni), Platinum (Pt), Copper (Cu), Molybdenum (Mo), Aluminum (Al), Silver (Ag), Gold (Au), and Tungsten (W). Except for Nickel, all the mentioned metals had less hydrogen permeability compared to steel at temperature less than 300^{o}C. According to ISO 4964[26, 27], the risk of hydrogen induced cracking mainly exists with a local tensile strength>1200 N/mm^2, a hardness>34 HRC or a surface hardness>340 HV. Notches, present in the microstructure of the surface, or material inhomogeneity increase the risk of damage.

1.3 Pipeline Risk Management system

Risk management plays a vital role in both government regulators and pipeline industry as a successful risk management plan does not only serve as a long-term decision-making tool for optimized pipeline operation, but also ensure the public safety in the relatively close range of a pipeline. Most commonly, a risk management process would include several steps: reviewing inherent risk of the defined pipeline system, constructing risk model and evaluating risk model with available data, and then utilizing the risk model to conduct risk assessment and support decision making. A comprehensive risk model generally constructs its detailed risk structure with consideration of every possible type of incidents that could happen to the pipeline system. With the support from available data, it provides information useful for decision making in a timely manner.

Before 1990s, risk management concepts in engineering field were generally exercised informally and based on the experience of engineers, not on mathematical computation or any probability model, due to the complex of interaction between structure and environments, and lack of computational power. Early attempts to achieve risk management of pipelines either focused more on management or financial aspect, lacking details in engineering, or were case by case studies, lacking general applicable rules[28-31]. After 1990s, with exponentially increased in computation power and capabilities and the

more advanced statistical studies, the risk management methodology in pipeline industry could be significantly developed.

By applying the basic idea of "risk equals probabilities times consequences", multiple risk assessment and management model had been proposed[32-41]. Pate-Cornell proposed a probabilistic risk analysis framework for offshore platform in 1993 that taking human factors into consideration[32]. This model considered not only the incidents and corresponding hazardous results, but also the possible prevention methods. As a result, this model could be used in proactive risk management applications. In 1996, Muhlbauer proposed an index-based risk management model[35]. Instead of going from the probability of failure types, this model started from the reliability of basic components in a pipeline system. By taking into account the severity of failure of different components, this model had different maximum possible index points for different components, ranging from 0 to 100. Then based on the current status of the components, an index score would be assigned to that component. The higher score indicates higher probability of failure of that specific component. By simply adding all the index together, one could get an index reflecting pipeline overall operation risk. This model was very easy to use and quickly gained attention from pipeline industry, but its drawback also came from its simplicity: oversimplifying the cross-effects of different components. Diller proposed a quantitative risk model by constructing a matrix with risk frequency index and the severity of accident[36]. By considering casualties, environmental impact, and damage done to the equipment, this model differentiates three levels of accident severity. By combining the risk frequency index and severity of one specific type of accident, the risk of the accident could be decided. Nevertheless, this model failed to provide a comprehensive decision-making procedure, as it lacks the ability to consider every possible accident all together.

In 2004, with significant improvement of risk assessment in corrosion and adding leakage impact factor, Muhlbauer introduced the most widely used pipeline risk management framework in pipeline industry[42]. This framework model considered five major parts during the pipeline operation: third-party damage, corrosion, design, incorrect operation, and leak impact factor. In the first four parts, each part has a comprehensive list of events or components that may contribute to a pipeline failure incident, and the leak impact factor is served as an overall multiplier to control the risk related to a possible leakage. In this model, detailed component scoring table was provided and supported with historical data. The flowchart in Figure 4 shows the risk management model.

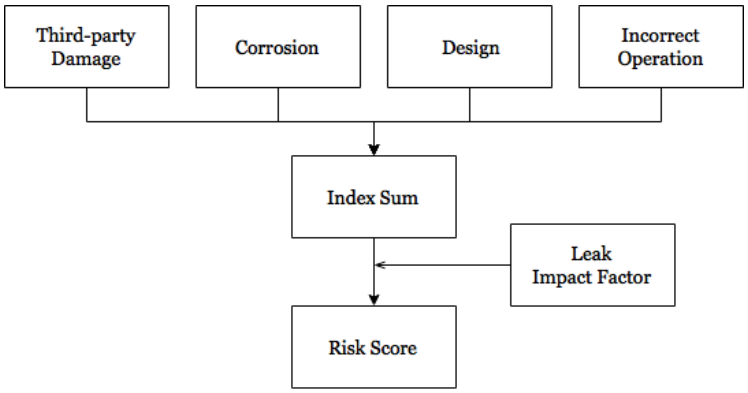

Figure 4. Risk assessment model flowchart[42].

To develop a model for risk assessment in curding components, the contributing factors include coating, environment corrosiveness, type of pipeline material, cathodic protection effectiveness, corrosiveness of the product that is transporting, etc. More recently in 2010s, with more information technology developments of big data technology, more updated risk management models have been proposed[43-51]. Most of them promised a better risk handling performance. Though they are not widely

accepted as all other newly developed technologies, the ideas of using comprehensive data to dig information behind the numbers and to make objective judgement of the condition of an operating pipeline emerged. Our research goal is to integrate proposed corrosion monitoring system into this widely accepted model in industry and to make it data-driven.

2 *Deposition of the Optimum HVOF Deposited Coatings for Corrosion Mitigation (Task 2, Completed)*

Several factors including galvanic series, hydrogen embrittlement which has already discussed in last section, alongside with corrosion rate and cost of the process were considered to propose a suitable material as coating being compatible with the pipeline and the soil environment.

2.1 Development of Automatic Rotational Fixture (Task 2.1)

To develop a more convenient spraying process for round objects such as pipes, two undergraduate students, Alan Perrault and Caio Molina Ferreira, from Mechanical Engineering department, NDSU, designed a rotating fixture to hold pipe samples in front of spraying nozzle for coating deposition. Figure 5 shows the spraying set-up for spraying process. It includes several parts: an adjustable pipe fixing holder, a rotational axle connected to a speed-control instrument, and a manually movable spraying gun holder. Pipes with inner diameter from 1 inches to 12 inches can be placed on the holder for spraying. The pipe can rotate at various speeds which is adjustable from low to high speed during the spraying process to meet the requirement for different spraying thickness. The spraying gun holder is designed to move horizontally at constant speed to provide a uniform deposition on the surface of the pipe samples.

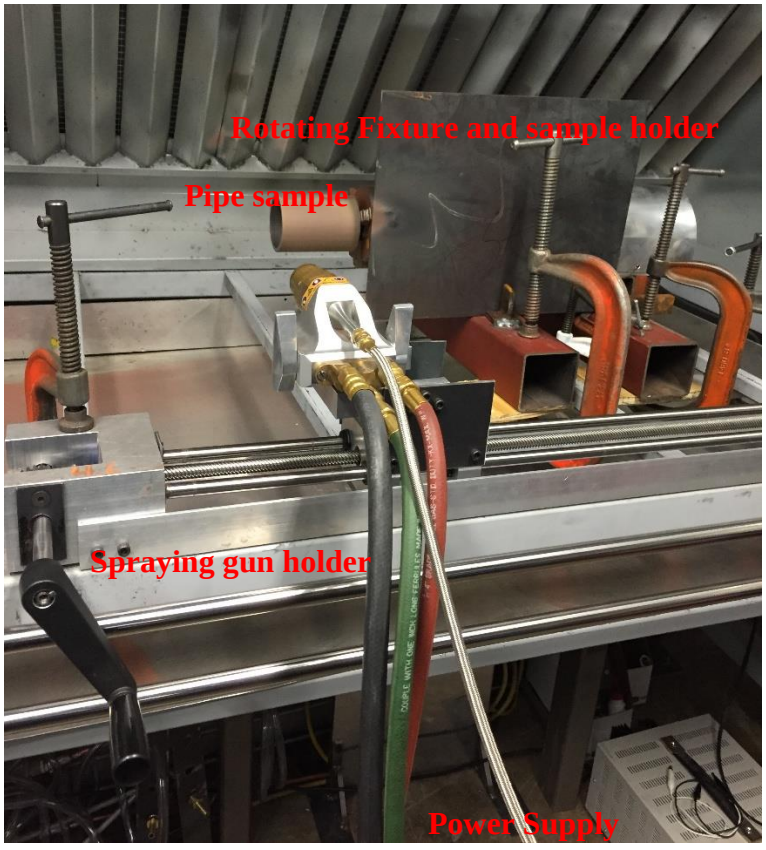

Figure 5. Automatic rotational fixture for pipe samples.

2.2 Material Selection of Optimum Coating Material for Pipeline Corrosion Mitigation (Task 2.2)

2.2.2 Materials Selection of Appropriate Coatings

From Section 1, it can be seen that zinc and aluminum alloys could be considered as very suitable candidates to be used as protective coating for steel pipe due to their good corrosion resistance, low possibility of inducing additional bimetallic corrosion on steel, and low hydrogen permeability. It is speculated that application of these two metals are economically justified due to relatively low cost of materials. Here are some information about the zinc and aluminum alloys.

2.2.2.1 Zinc-alloy

Galvanized steel has been used for more than 100 years and it is still remains in high demand. Zinc has inherently good corrosion resistance to normally prevailing atmosphere. Addition of approximately 0.1% Al to the zinc, used for galvanizing iron and steel, greatly reduces the formation of a brittle intermediate layer of zinc-iron compound. Adding aluminum to hot-dip galvanizing has shown significant increase in ductility. This also improves the strength with reducing the grain size. Adding 0.01 to 0.06% Mg prevents intergranular corrosion in zinc-aluminum alloys. However, the optimum amount of recommended aluminum to zinc is between 3.5 to 4.3% to achieve the best impact strength and surface finish[18, 52~54].

2.2.2.2 Aluminum-alloy

Aluminum perhaps is the most important non-ferrous metal due to its good corrosion resistance along with low density, reasonable high strength, and relative low cost. Aluminum-coated steel requires a more difficult process compared to zinc, but is used in major applications including chain links, roofing panels, and automotive exhaust components. The good corrosion resistance of the aluminum is due to almost instantaneous formation of protective oxide (Al_2O_3) film when the metal is exposed to the air or any other oxidizing medium. When first formed, this film at approximately 0.25nm thickness acts as a protective barrier to oxidation. Aluminum-zinc alloy coated steel provides a combination of galvanic protection and low corrosion rate. Iron, silicon, and copper are the major alloying elements being used in aluminum alloys. However, because copper reduces the corrosion resistance of the aluminum more than the other alloying elements, it usually is added in very small amount (usually less than 0.2%) to improve the strength and fabrication characteristics without appreciably affecting the corrosion resistance. Addition of manganese to aluminum alloy may result in formation of manganese aluminide ($MnAl_6$) which hold iron impurity in solid solution, thus avoiding the adverse effect on corrosion resistance[18, 52~54].

2.2.2.3 Cost estimation and corrosion rate

Table 2 shows the estimation of the material cost and the experimentally measured corrosion rates in quiet seawater. Melting point of the materials was also taken to the account to estimate the energy (cost) required for thermal spraying each of listed materials.

Table.2. Selected important properties of the Al and Zn alloy coating materials. [15]

Material	*Melting point ^oF*	*Price USD/kg*[52]	*Corrosion rate in quiet seawater mm/year [16-18]*	*Electronegativity*
Al-alloy	*1060-1240*	*1.5-1.6*	*<0.03*	*1.61*
Zinc-alloy	*707-917*	*1.7-1.9*	*<0.031*	*1.65*

As seen in Table 2, both Zinc and Aluminum alloys expected to be suitable materials to be coupled with steel pipe in order to corrosion protection. Both of these metals are more electronegative with respect to the steel. This makes them as sacrificial anode to steel resulting in its protection. Considering

their relative low price range, these two materials can be considered as an economical protective coating. However, the melting point range of the zinc is less than aluminum, which may result in the lower total cost of the deposition process since it may require lower energy for thermal spraying process. Zinc performs better than aluminum in alkaline conditions, while aluminum is better in acidic conditions. The aluminum-zinc coating with high zinc content and the zinc coating possessed the best anti-corrosion and anti-fouling properties [15]. According to Davis (2004) the lifetime of a 255-µm thick zinc or zinc aluminum coating is about 25 years and it can be extended by 15 years by sealing it with vinyl paint[18]. Besides painting, impregnation with special compositions (epoxy resin, silicon resin, etc.) is also one of common sealer materials that is used currently.

2.2.3 Material Optimization of Thermal Sprayed Al- or Zn-based Coating

Since Zinc and Aluminum have been selected as the major coating material, consideration should also be made about their alloys to optimize corrosion mitigation of Al- and Zn-based coating. Table 3 summarizes and compares the corrosion performances of thermally sprayed Al- and Zn-based coatings. Effect of addition of other supplemental elements, such as Mg, Si, and RE, on corrosion durability of these alloys in harsh environment was also considered here for an optimal corrosion protection.

Table 3 Corrosion behavior of thermal sprayed Al- and Zn-based coatings on steel at (25°C).[55-93]

Coating material	*Coating technique*	*Corrosive solution*	*Observations*
Al-based			
99% aluminum	*Arc spray*	*3.5% NaCl*	*Formation of passive layer by increasing the exposure time made of Al_2O_3 and $Al(OH)_3$*
Al- Al_2O_3	*Arc spray+ PEO*	*3.5% NaCl*	*Dense coating and excellent corrosion behavior*
Al-5%Mg	*Arc spray*	*3.5% NaCl*	*Better corrosion resistance even that Zn-Al alloys*
Al-Zn-Si	*HVAS*	*3.5% NaCl*	*Self-sealing nature and good cathodic protection*
Al−Zn−Si−RE	*HVAS and arc spray*	*3.5% NaCl*	*5 steps during the corrosion: pitting-dissolution-re-deposition, activation corrosion, cathodic protection, physical barriers formed by corrosion products, and failure of coating*
Zn-based			
Zn-15Al	*Flame spray*	*Marine environment, 30 days*	*Improved cathodic protection, but lower long-term durability compared to pure Al coating*
Zn-15Al	*HVAS*	*SRB*	*Corrosion of surface at first place, formation of ZnS and plugging the pores at second stage*
ZnMgAl	*Wire arc*	*5% NaCl*	*Formation of dense corrosion products, clogging the pores and slowing corrosion*
Zn-Al-Mg-RE	*HVAS*	*5% NaCl*	*Better corrosion behavior than Zn-Al-Mg due to the microstructural refinement of coating by adding RE*
Zn-Al-Mg-RE-Si	*Arc spraying*	*3.5% NaCl*	*Self-sealing behavior due to formation of Al3.21Si0.47 and Mg3Al2(SiO4)3*

2.2.3.1 Aluminum-based Coatings

As mentioned before, aluminum is one of the most commonly used metals for corrosion protection due to its anodic nature that eliminate the need for formation of flawless coating. In fact, aluminum coatings act as sacrificial protection to the steel substrate and forms passive layer made of Al_2O_3 and $Al(OH)_3$ which protect both coating and substrate from further corrosion[55-73]. It has been reported that arc sprayed Al coating showed better corrosion performance than flame sprayed since the aluminum oxide/hydroxide persisted for longer sputtering time on the lamella (coating layers) than that of flame sprayed[55]. Increase in the thickness of the arc sprayed Al coating deposited on steel could increase its durability in sea water[56]. Passive nature of alumina (Al_2O_3) made it one of the most interesting and common-used coating materials to protect steel from pitting corrosion and provide more uniform corrosion[57-68]. The addition of Al_2O_3, up to 30%, to Al powders helps improving the coating deposition and bonding strength between Al and Al2O3[57]. Magnesium is also considered a common element to be added to Al-based alloys to enhance the long-term corrosion resistance as well as mechanical properties such as hardness[59-61]. It has been shown from previous studies that the weight loss of arc sprayed Al-Mg alloy on a mild steel in seawater, at room temperature after 90 days, was significantly less than that of pure Al coating[59]. Arc sprayed Al-5%Mg shown to successfully protect steel after 14,000 h exposure to salt water, even better than Zn–35%Sn and Zn-27%Al (by mass fraction) [60]. Zinc is another important element added to Al-based coating due to its high sacrificial nature providing cathodic protection especially to steel substrate[62]. Al-Zn alloys, even without sealing, exposed in marine and industrial environment, provide very high galvanic corrosion protection to steel substrate[63]. Al-Zn-Si-based alloys are known as self-sealing material in corrosive environment due to their capability to produce components to clog the pores and prohibit further penetration of corrosive solution in to the coating62[-66]. Al-Zn-Si-RE (where RE is Rare Earth) coatings, among Al-Zn based alloys shown excellent corrosion resistance performance [64]. It has been reported that the corrosion mechanism of this alloy is very similar to Zn-15%Al, in which five distinct stages were observed: pitting-dissolution-re-deposition, activation corrosion, cathodic protection, physical barriers formed by corrosion products, and the failure of the coating. The RE in the coating does not affect the phase compositions of the corrosion products, but it can improve the formation of fine, continuous and uniform corrosion product layer, which acts as stable self-sealing process.

2.2.3.2 Zinc-based Coatings

Thermally sprayed zinc-based alloys have also been widely used to protect steel constructions due to its high stability in the sea water and also lower electronegativity respect to steel which makes it acts as sacrificial anode[74-93]. However, if the coating is exposed to high humidity or mediums containing aggressive species such as chloride or sulfate ions, the Zn will dissolve in the solution and result in localized corrosion. This problem has not been observed in Al-based coatings. Twin wire arc is one of the most common thermal spray techniques used to deposit Zn. It has been shown that corrosion resistance of pure Al coating deposited by wire arc spray technique was higher than that of pure Zn coating[74-77]. Zn-15%Al showed the higher corrosion resistance than both Zn and Al coating since it possesses combination of two protection mechanisms: (1) creating a stable oxide, like Al coating, and (2) acting as sacrificial anode, similar to Zn coating[74-79]. Different percentages of Al content also could significantly effects on the corrosion resistance of Zn-Al-based alloys. It is reported that the porosity of arc sprayed Zn-30%Al coatings was higher than that of Zn-15%Al. Thus, 85%-15% ratio of Zn and Al showed better corrosion resistance in short-term immersion in corrosive medium such as 3.5%NaCl[77]. However, the long-term corrosion durability of pure arc sprayed aluminum coating was still higher than those of both pure Zn- and Zn-15%Al coatings deposited with the same technique[74,77,82,83]. Magnesium can also be added to Zn alloy to work as the sacrificial anode. The addition of magnesium to Zn-Al-

based alloy could significantly enhance the corrosion due to self-sealing nature of Zn-Al-Mg alloys[87-90]. This was attributed to formation of intermetallic phases such as MgZn2 and MgZn11 and, in some cases, Zn5(OH)8Cl2.H2O, which plug the pores and protect the substrate against corrosive electrolyte. That makes Zn-Al-Mg coating showing even better corrosion resistance than that of pure Zn and Zn-Al coatings. It has been reported that the time for red rust to appear in the neutral salt spray test of Zn-Al-Mg coating is 4-20 times higher than that of pure Zn coatings[87-88]. Zn-Al-Mg-RE alloys are also commonly used as corrosion protection coating due to their self-sealing nature. They possessed better corrosion resistance than Zn-Al-Mg coating which is believed is due to the formation of denser, more compact, and uniform corrosion products as result of coating refinement by addition of RE elements[91-93]. Zn-Al-Mg-RE-Si coating is yet shown superior corrosion resistance than Zn-Al-Mg-RE due to presence of glass-like state phase attributed to Mg3Al2(SiO4)3 formed on the external surface of Zn-Al-Mg-RE-Si coating which acted as self-sealing barrier, depressed the porosity of coating, and hindered reaching the electrolyte to the substrate.

2.2.3.3 Optimized Thermal Sprayed Coating Material

Taking all the above reviews into consideration, the Al-Zn alloys can be considered as good candidates for optimal corrosion protection of steel, due to their cathodic protection nature that could significantly reduce the rate of corrosion.

2.3 Arc Spray Techniques and Microstructural Characterization of Deposited Coatings (Task 2.3)

As it could be seen in the Table 3, the most commonly used thermal spray method for deposition of Al- and Zn-based coatings is Arc spray technique. In fact, combustible nature of Al- and Zn-based alloys at high temperature provided by thermal spray techniques such as wire arc, HVOF, and cold spraying limits using of them to deposit Al-Zn alloys. In this study, the microstructural properties of all three thermal spraying methods had been studied, including the wire arc spraying, HVOF, and cold spraying methods. HVOF technology, Cu and Al-Brane were used to coat the steel and please refer to our previous project (Project No. DTPH56-13-H-CAAP05) final report for more details.

For wire arc spraying technology, also known as electric arc spray, was commercially acceptant in early 1960s[27]. Unlike the other thermal spray techniques, feedstock particles of which indirectly get heated by using heated gas jet, in electric arc spray process direct current (DC) is used to strike between two consumable electrode wires to effect direct melting. As shown in Figure 6, an electric arc is formed in the gap between the wire tips as the two wires are continuously fed together. It is worth mentioning that thermal efficiency of electric arc spray process is significantly higher than that of other thermal spray processes. There is a high velocity air jet located behind the intersection of the wires which shears away the molten particles and projects it toward the substrate. The velocity of in-flight particles in arc spray technique is ranged within 0.8-1.8 m/min which is much lower than HVOF (over 8 m/min) technique and consequently less harsh for the substrate [27]. Electric arc spray also transfers less heat to the substrate per unit of material sprayed compared to any other conventional thermal spray methods because there is no flame or plasma jet used in this technique. Materials to be used for arc spray should be electrical conductive in the form of wire. Using cord wires, however, expanded the range of the materials including cermet and amorphous materials. Cored wires, in fact, are made of a tubular metallic sheath with powder in the core which is usually consisted of carbide or amorphous alloys. Figure 7 shows two samples coated using wire arc technology using Al-Zn materials with different thicknesses.

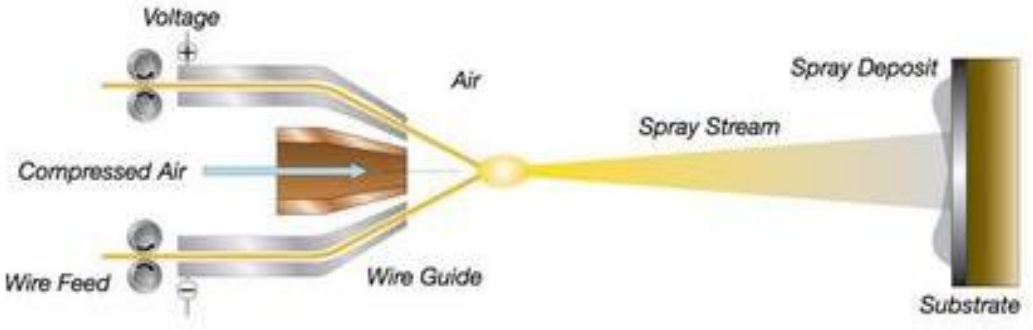

Figure 6. Schematic of arc spray technique.[27]

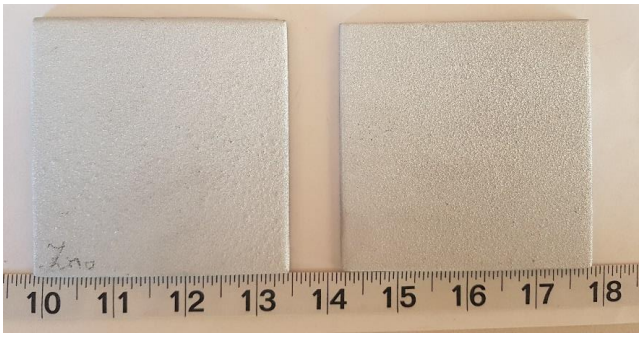

Figure 7. Wire Arc deposited Al-Zn coating on steel substrate, left 2 mm, and right 0.1 mm.

As an alternative approach to coating deposition, cold spraying technology was aslo studied to deposit coatings. The cold spraying technology heated the coating powders to a semi-molten state and shot towards the substrate at a speed of up to 1200 m/s. This technology is one the newest members of thermal spraying techniques and it can produce high quality coatings consisting of low porosities. To increase the flexibility in on site coating of components, in this study, cold spraying technology was used to coat the optimized material (Al-Zn). Low pressure cold spray is the only deposition technique with high mobility possibilities. Cold Spraying equipment developed in Europe are relatively small and light weight with capability of being carried by single operator which can apply coating on site. If the high quality (high corrosion resistance and mechanical strength) of the cold sprayed Al-Zn is proven, then it can improve flexibility of the proposed work and reduce down time of the system. Cold spraying Compared with the arc wire coating technology, cold spraying requires much less energy input and very mobile, and thus is more easily to be applied on site. Al-Zn with composition as defined in previous tasks was deposited by Plasma Giken Co, Japan, on an aluminum substrate with dimension of 1.5 in × 1.5 in × 0.5 in (3.8 cm × 3.8 cm × 1.3 cm) as shown in Figure 8 and Figure 9. The thickness of the Al-Zn deposited coating was 0.05 in (0.13 cm) as shown in Figure 10.

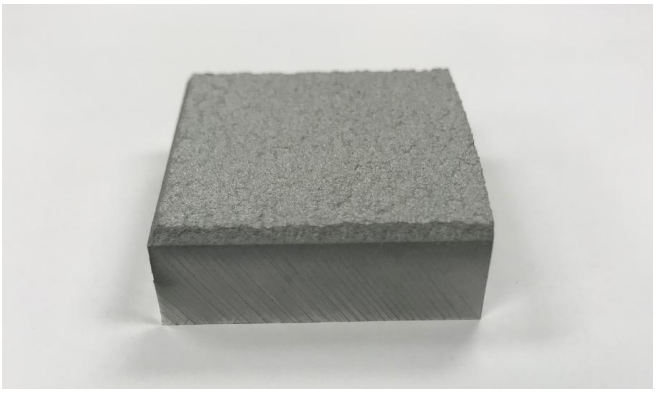

Figure 8. Sample with cold sprayed Al-Zn coating.

Figure 9. Dimensions of the sample to be tested.

Figure 10. Measurement of coating thickness.

2.3.1 Mechanical Properties

The mechanical properties of different coatings were examined in this study. The mechanical properties investigated include wear, hardness, and porosity. Wear test determines the behavior of the coating in physical contact with other objects which may result in friction and abrasion and material loss over time. Hardness test can show the resistance of the coating to any indentation and deformation. Porosity measurement is a method of estimation of quality of metallic coatings.

2.3.1.1 Wear Test

The wear test was performed in the UMT DFH20G Bruker machine, which can apply force up to 200 N. This device can measure Sliding Wear and Friction Behavior between a Static Pin (Area Contact) and Ball (Point Contact) and a Rotating Surface. For this experiment, the indenter applies a load of 10 N, rotating on a circle with a diameter of 2 cm at 265 rpm for 80 min, corresponding to a total distance of 1,332 m. The wear test was performed on the Al-15Zn wire arc coating.

Table 4. Coefficient of friction resulted from wear test on Al-15Zn wire arc coating

Surface of Wear Test	*Fx*	*Fz*	*COF*
Al-Zn Coating	*4.186±1.018*	*10.18±1.787*	*0.4121±0.071*
Aluminum Substrate	*4.87±0.6088*	*9.966±0.635*	*0.4883±0.501*

The results of wear test listed in Table 4 show an improvement of the surface after applying the Al-15Zn wire arc coating as coefficient of friction has dropped and causes less material damage and loss over certain period of time. On the other hand, hardness test results imply that R2 which suffers from salts caused by corrosion test has less hardness than aluminum, while R1 which is as-deposited coating has better hardness behavior compared to bare aluminum. Considering the results of both tests, it can be concluded that applying Al-15Zn wire arc coating improved mechanical properties of the surface.

2.3.1.2 Hardness Test

The Vickers hardness test creates square-shape indents on the surface. Both diagonal lengths should be measured, and a mean value will be used for hardness calculation. It is worth mentioning that the diagonal lengths have a small difference in size due to the anisotropic nature of coatings. Indents were made under a load of 1kgf and a dwell time of 15sec. To achieve a better accuracy, 15 indents were made with respect to ASTM E92-17 and ASTM E384-17. Figure 11(a) shows a SEM image of a Vickers indentation on cold sprayed sample. Knoop indenter has a long major diagonal, which is perfect for anisotropic structures such as coatings, covering a large area including pores and voids. The major diagonal of indentation is measured and used for hardness calculation. Nine indentations were performed to increase the accuracy of the results. Figure 11(b) shows a SEM image of a Knoop indentation on cold spray deposit.

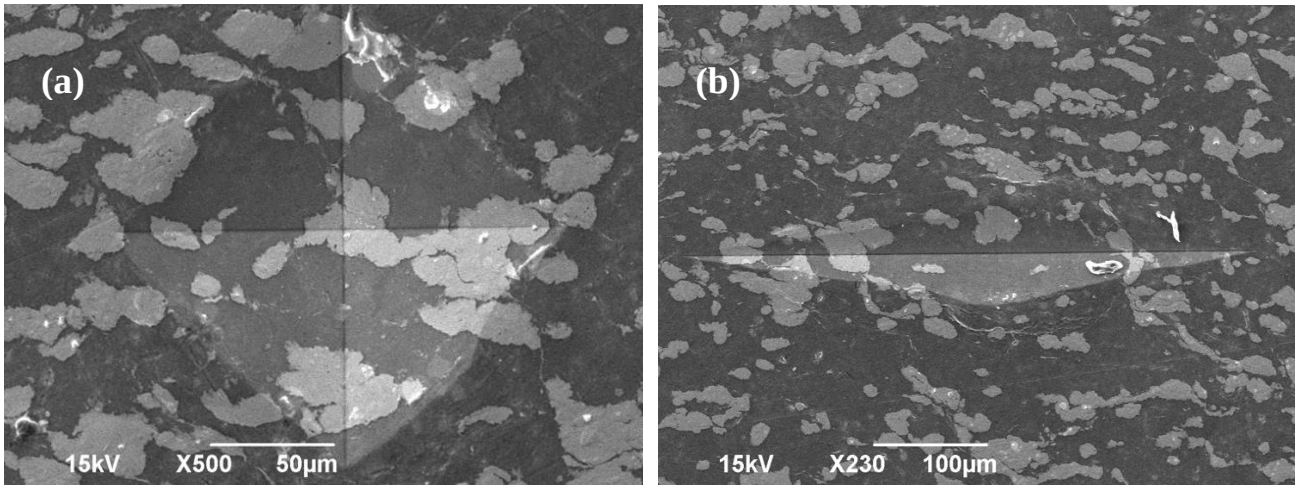

Figure 11. (a) SEM image of a Vickers indentation. (b) SEM image of a Knoop indentation.

Table 5(a) shows the measured results of hardness from the Vickers hardness test and Table 5(b) shows the measured results of hardness from the Knoop indentation test. Table 6 indicates the average of values obtained for Vickers and Knoop indentation tests for both wire arc and cold spray deposited samples.

Table 5 (a). Hardness values measured by each indent from Vickers hardness tests.

Vickers Indent	*Cold Spray*	*Wire Arc*
1	*53.7*	*46.5*
2	*56.7*	*46.1*
3	*52.1*	*42.3*
4	*52.3*	*45.9*
5	*52.5*	*46.5*
6	*56.6*	*47.3*
7	*53.2*	*41.3*
8	*54*	*46.1*
9	*59.8*	*46.5*
10	*57.7*	*46.1*
11	*53.4*	*46.2*
12	*55.3*	*44.1*
13	*50.6*	*43.7*
14	*53.5*	*45.1*
15	*54.9*	*45.6*

Table 5 (b). Hardness values measured by each indent from Knoop hardness tests

Knoop Indent	*Cold Spray*	*Wire Arc*
1	*56.1*	*42.6*
2	*54.5*	*44.6*
3	*53.9*	*38.7*
4	*53.5*	*40.1*
5	*53.3*	*44.8*
6	*54.5*	*41.8*
7	*54.8*	*38.6*
8	*49.2*	*44.2*
9	*53.1*	*41.1*

Table 6. Micro hardness test results by averaging results from Vickers and Knoop hardness tests

Deposition Technique	*Vickers Hardness (HV)*	*Knoop Hardness (HK)*
Cold Spray	*54.42±2.43*	*53.65±1.91*
Wire Arc	*45.28±1.70*	*41.83±2.41*

The hardness values of both wire arc and cold sprayed Al-Zn coatings are much smaller than the hardness of pure aluminum or zinc materials. Existence of pores, voids and splat boundaries in thermally sprayed coatings deteriorates mechanical properties. The obtained results indicated that cold spray samples has shown a higher hardness than wire arc deposited samples even though Zn-20Al have higher hardness and elasticity than Al-25Zn. It can be concluded that cold spray technique can produce coatings with higher quality compared to the conventional wire arc spraying technique. Taking to the account the previous results obtained from object oriented finite element; cold spray samples exhibit higher mechanical properties with lower porosity level.

2.3.1.3 Porosity

Table 7 shows the estimated porosity level for all the three trail materials which have been coated on the steel substrate including copper, Al-Bronze as investigated before and Al-Zn results as measured in this quarter.. The results showed ~7% porosity for wire arc sprayed Al-Zn coating which was relatively higher compared to those of HVOF deposited copper coating (~3%) and HVOF deposited Al-bronze (~5.5%) which were investigated before.

Table 7. Porosity measurement of the thermally sprayed coatings.

Materials	*HVOF Copper*	*HVOF Al-Bronze*	*Wire arc AL-Zn*
Porosity Area %	*3±0.5*	*5.5±0.7*	*7±0.6*

2.3.2 *Microstructural characterization before and after corrosion tests*

The aim of this section was to better understand the effectiveness of the thermal sprayed and cold sprayed coatings in term of corrosion behavior and also blocking the deleterious elements such as Cl- to penetrate into the interior layers of the coatings. To this end, the coatings were subjected to the microstructural characterization techniques such as Scanning Electron Microscopy (SEM), Electron Diffraction Spectroscopy (EDS), X-ray powder diffraction (XRD), and image based finite element analysis using Object Oriented Finite (OOF) software. The SEM was also equipped with a Nanotrace EDS detector with a NORVAR light-element window. The accelerating voltage used for EDS was 15 keV to investigate the elemental distribution of the coatings.

2.3.2.1 SEM Image Analysis

For HVOF deposited Al-Bronze coatings which had been studied in previous project (Project No. DTPH56-13-H-CAAP05), the SEM micrographs taken from the cross-section of the coatings before and after corrosion were shown in Figures 12 (a, b) and for the wire arc sprayed Al-Zn coating, the SEM images were shown in Figures 13 (a, b). It could be concluded that corrosion products significantly were formed on the surface of the HVOF deposited Al-bronze and the wire arc sprayed Al-Zn coatings after corrosion. The dark gray areas presented very close to the surface of the coating were observed after corrosion which did not exist in the SEM micrograph of the HVOF deposited Al-bronze and the wire arc sprayed Al-Zn coatings before corrosion. These areas could be associated to the corrosion products formed after exposing to the NaCl solution.

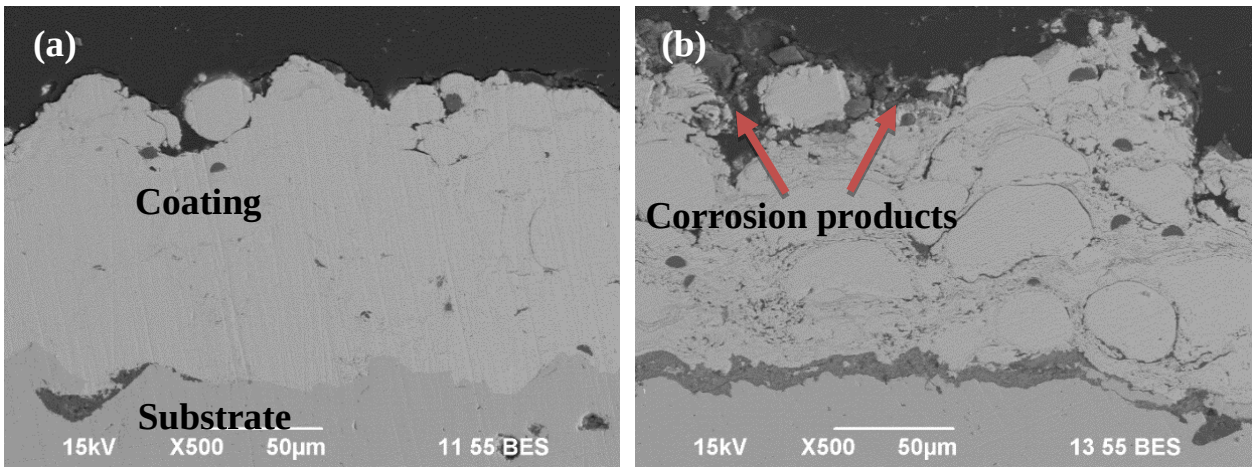

Figure 12. SEM micrographs of the HVOF deposited Al-bronze coating (a) before and (b) after corrosion.

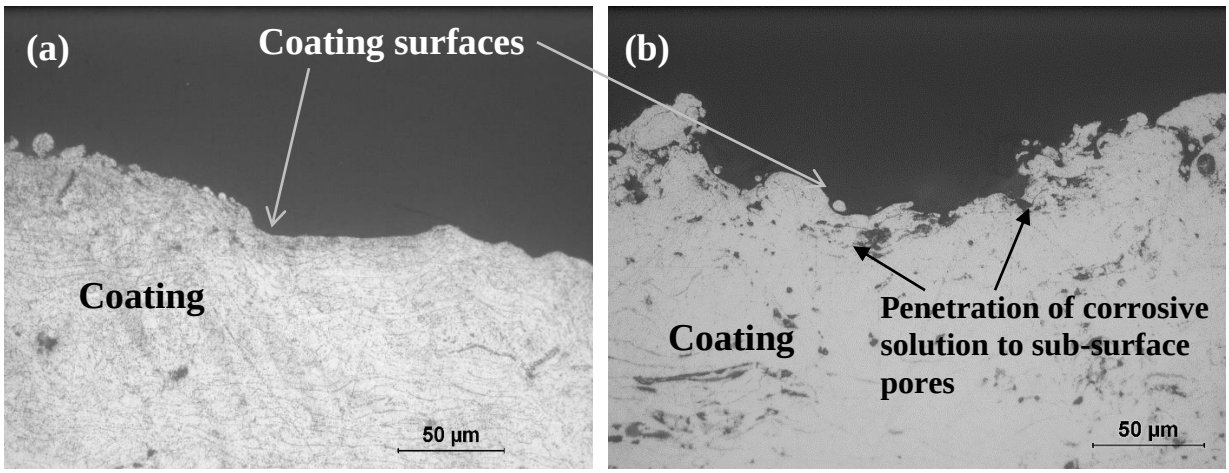

Figure 13. SEM micrographs of the Wire arc deposited Al-Zn coating (a) before and (a) after corrosion

Figures 14 (a, b) show the SEM images from for cold sprayed Al-Zn coating and the wire arc deposited Al-Zn coating. The points used for the EDS measurement were also indicated in Figure 9. From Figure 9, it can be seen that solid particles were not mixed in cold sprayed coating, while wire arc deposited one exhibit a mixture of aluminum and zinc.

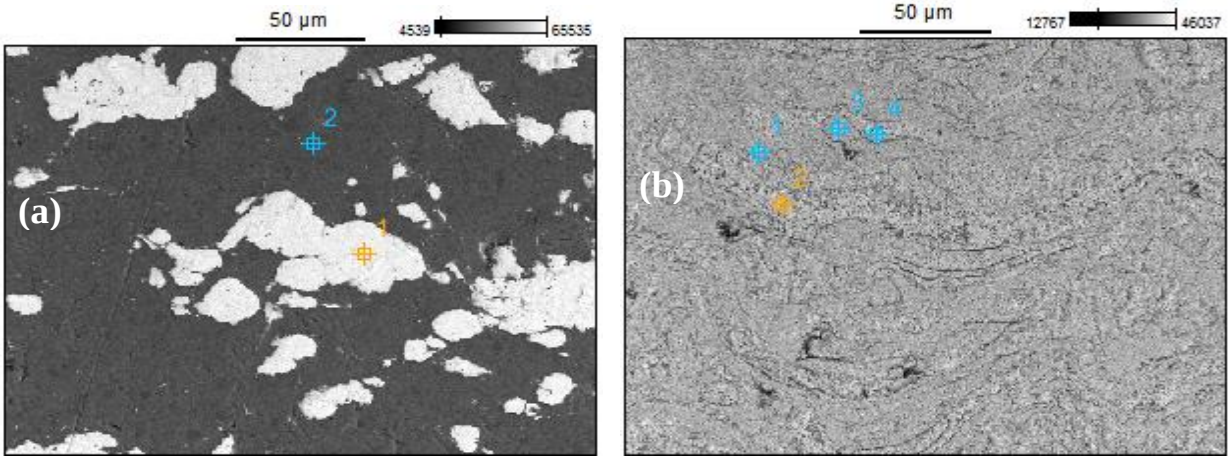

Figure 14. SEM image of (a) cold spray and (b) wire arc deposited samples

2.3.2.2 EDS Mapping Analysis

The elemental distribution in the coatings' microstructures was studied by EDS mapping technique and were presented in Figure 15. The major objective of EDS mapping was to detect the depth of the penetration of the deleterious elements, preferably Cl-, to estimate the effectiveness of the coating to act as a barrier to hinder diffusion of such a d detrimental elements in to the coatings.

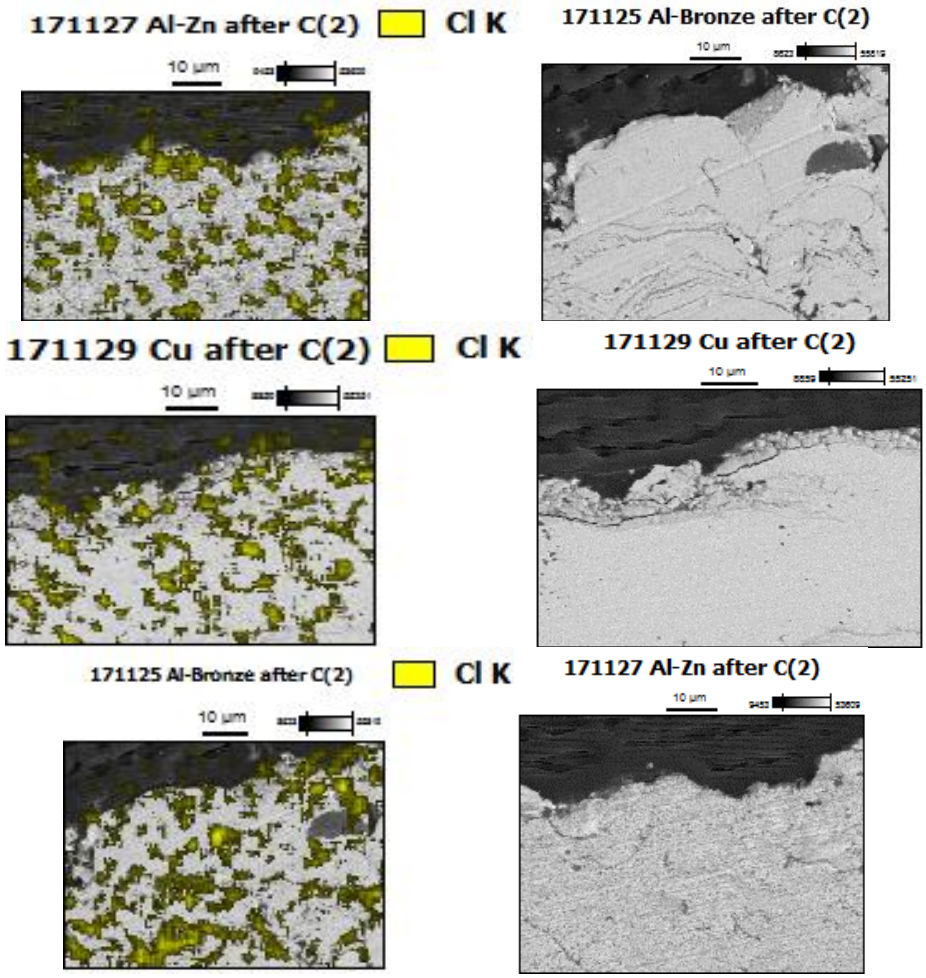

Figure 15. EDS maps of Cl- element penetrated in a variety of thermally sprayed coatings after corrosion experiment in this project.

According to the EDS results, chlorine had diffused more in to HVOF deposited Al-Bronze compared to Cu and Al-Zn coatings. That could be due to relatively high level of porosity detected in this coating. The other EDS map shown in Figure 11, demonstrated the penetration depth of the Na

element inside the coatings. This value for the Al-Zn coating had the lowest value as it appeared as very small area which was overlapping with the Zn map. As it can be seen from the images in Figure 16, Al-Zn acted less effective compared to the other coatings in terms of blocking the sodium elements inside the coating.

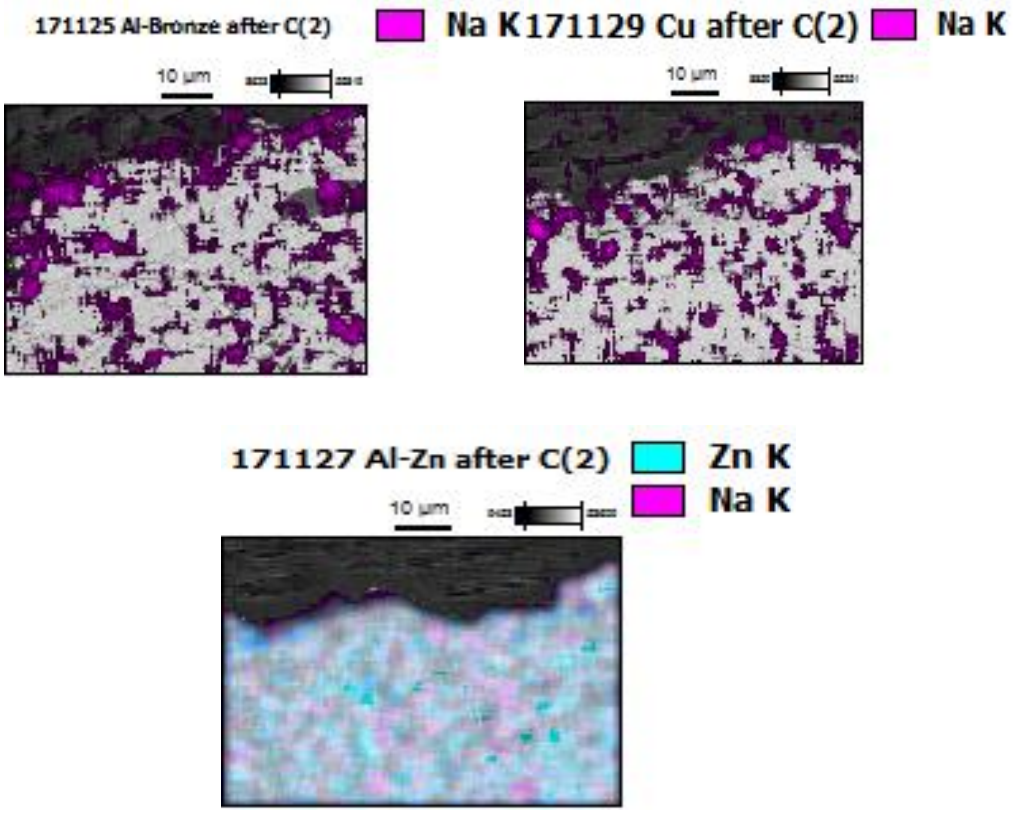

Figure 16. EDS maps of Na+ element penetrated in the thermal sprayed coatings.

The composition of the coatings before and after corrosion were also been evaluated by using a Rigaku Ultima IV diffractometer (Cu Kα radiation, voltage 40 kV, current 44 mA, and a fixed incident angle of 1.5 degree in a parallel beam geometry). Table 8 shows the results of the EDS measurements. The EDS was performed on multiple micrographs and results indicated a composition of Al-25Zn for cold sprayed sample and Zn-80Al for wire arc coating.

Table 8. Composition of cold sprayed and wire arc sprayed Al-Zn coatings from EDS.

Point	*Al (weight %)*	*Zn (weight %)*
Cold Spray 1	*0.81*	*99.19*
Cold Spray 2	*100.00*	*0*
Wire Arc 1	*21.61*	*78.39*
Wire Arc 2	*14.36*	*85.64*
Wire Arc 3	*18.88*	*81.12*
Wire Arc 4	*6.13*	*93.87*

2.3.2.3 XRD Analysis

After analyzing the XRD pattern of wire arc sprayed Al-Zn coating as shown in Figure 12, before corrosion, it was observed that the coating was mainly composed of Aluminum and Zinc. After corrosion as also seen in Figure 17, some other peaks belonged to aluminum oxide and zinc oxide detected, which were formed as the result of the passivation process of the surface. Presence of these

oxides were also identified in the earlier report considering the Tafel curve obtained after corrosion of the Al-Zn coating in 3.5% NaCl solution.

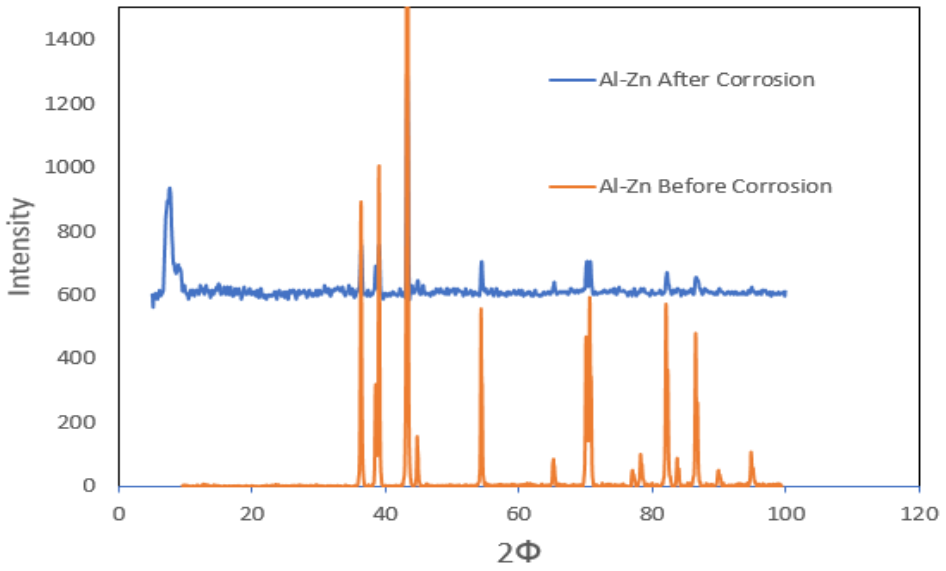

Figure 17. X-Ray pattern of wire arc sprayed Al-Zn coatings before and after corrosion.

XRD-pattern of the HVOF sprayed copper coatings which was also deposited earlier in this project exhibited some dissimilarity when comparing before and after corrosion conditions in this coating. The XRD pattern shown in Figure 18 demonstrated that copper oxide was the main composition appeared after corrosion whilst it was not detected in the coating structure before the corrosion experiments.

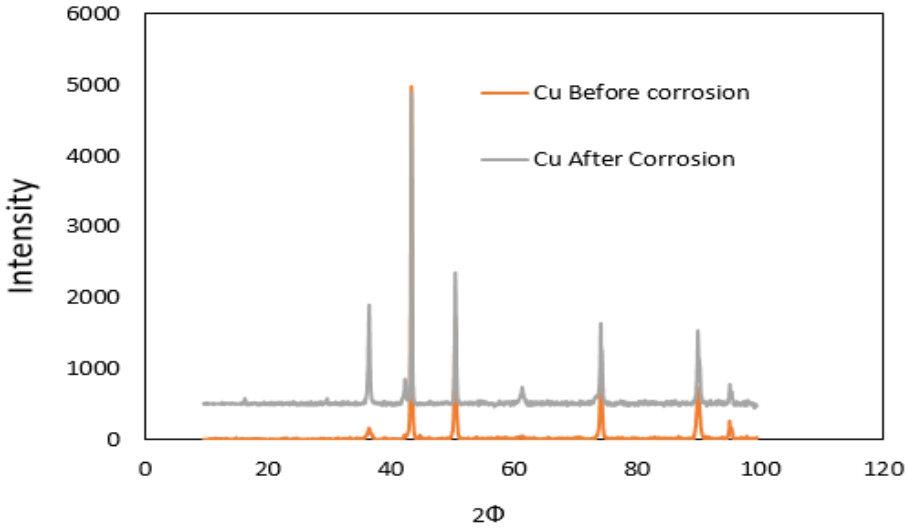

Figure 18. X-Ray pattern of HVOF sprayed Copper coatings before and after corrosion.

HVOF deposited Al-bronze was mainly contained $AlCu_3$ and Ni3ZnC0.7 before corrosion as it is shown in Figure 19. After exposed to the corrosive environment, there were more materials such as $AlCu_3$, Cu_2O, and FeO(OH) were identified in the Al-bronze coating.

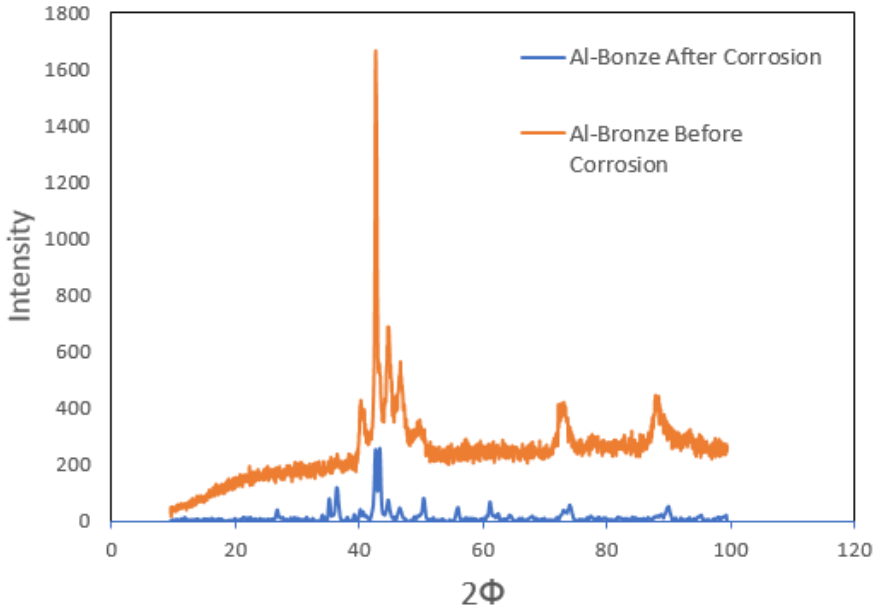

Figure 19. X-Ray pattern of HVOF sprayed Al-bronze coatings before and after corrosion.

All those experiments confirmed effectiveness of wire arc sprayed Al-Zn coating in corrosion prevention on steel substrate and its better quality compared to previously produced coatings.

2.3.2.4 Image based Finite Element Analysis using OOF Software

2.3.2.4.1 Wire Arc Sprayed Coating

Due to the dependency of the mechanical, physical, and electrochemical properties of coatings on microstructural features such as pores, voids, and splat boundaries, it is important to account for these features in finite element models of coating behavior. A schematic of the microstructure of a wire arc sprayed Al-15Zn coating is shown in Figure 20. The Object Oriented Finite (OOF) element analysis program, developed at the Center for Computational and Theoretical Materials Science (CTCMS) at US National Institute of Standards and Technology (NIST), enables complex two dimensional microstructures to be modeled using images of the actual microstructures. This analysis technique has been employed extensively to numerically simulate mechanical and thermo-physical properties of coatings and composite materials in recent years. Version 2.1.14 of OOF was used for image based numerical simulation.

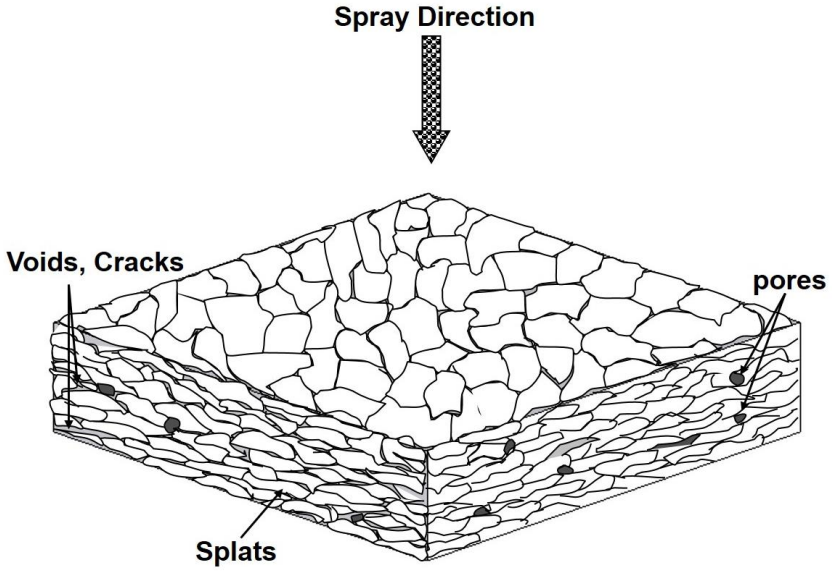

Figure 20. Schematic of microstructure of a Wire Arc sprayed Al-Zn coating.

In the first step several micrographs were taken from randomly selected positions along the polished cross-section of the wire arc sprayed Al-15Zn coatings. Figure 21 shows an optical micrograph of the cross-section of the as-sprayed coating. Next, two groups of pixels were created; Matrix and Pores based on the two different contrasts seen on the microstructure. Dark pixels on the image represent voids and porosities on the coating, while gray ones show the coating material Al-15Zn.

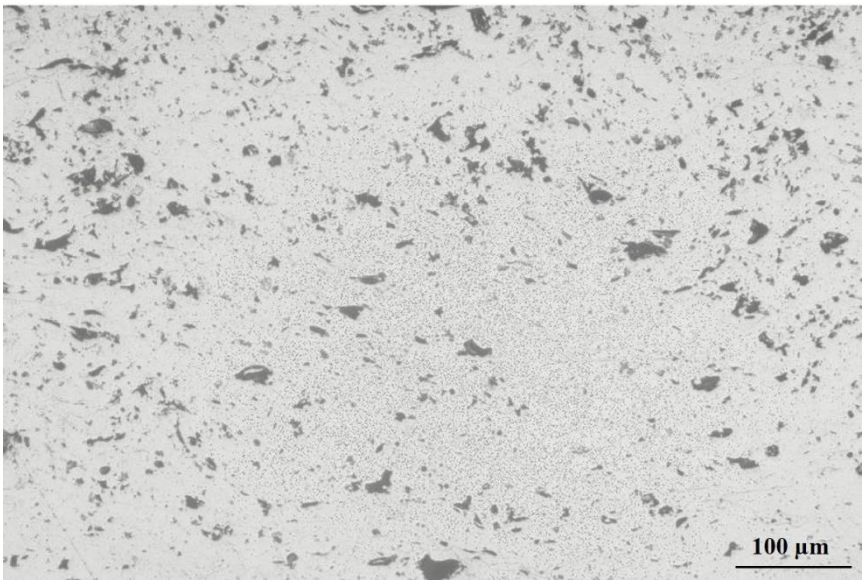

Figure 21. Optical microscopic image of Al-15Zn coating cross-section.

Then, different pixels were selected according to their color difference using RGB method. For this microstructure, a range of 0.2 color difference was suitable to distinguish pores and matrix pixels and assign them to their corresponding groups. In materials menu, elasticity property of each group was created by determining the values for E and ν, which for the matrix were 80 and 0.32, while for the pores they were defined as 1×e-09 and 0.32. For voids and pores, we can assume that the Poisson ratio is similar to the value for the matrix to avoid any incompatibility in the software, while the elastic modulus is set to a very small number since it cannot be set to zero. The elastic modulus for pure aluminum is around 70 GPa and it increases by adding zinc to aluminum, as for Al-6Zn it has reported to be around 73 GPa and for Al-9Zn the elastic modulus increased to 77 GPa. The elastic modulus of 80 GPa for the alloy Al-15Zn was selected according to this assumption. Figure 22 shows the processed image after dividing features to two different types of pixels. Assigned properties used for calculation by OOF are listed in Table 9.

Table 9. Mechanical properties of the wire arc Al-15Zn coating

Group	*Elastic Young's Modulus (GPa)*	*Poisson Ratio*
Matrix (Al-15Zn)	*80*	*0.32*
Pores (voids)	*1e-09*	*0.32*

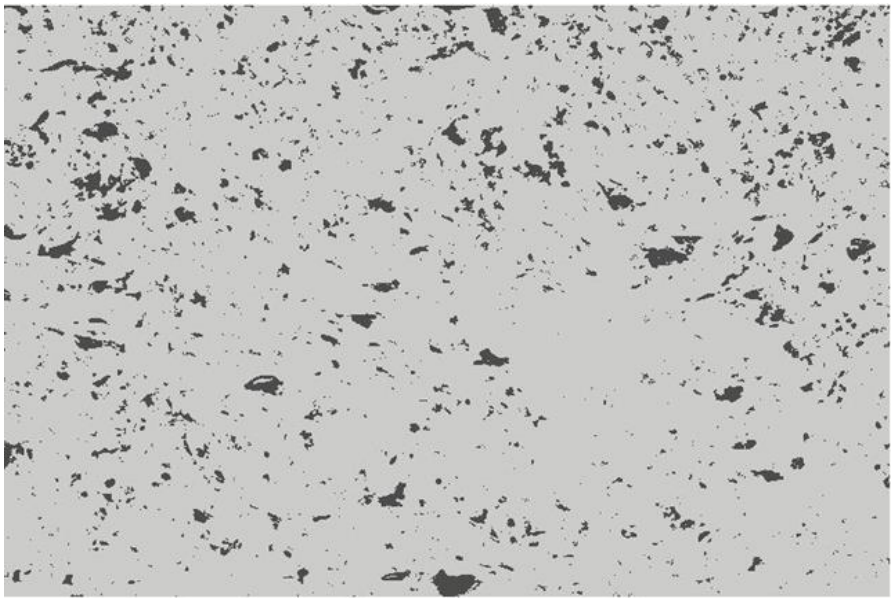

Figure 22. Modified image, Dark and gray pixels representing voids and matrix respectively.

In the next step, elements were defined on the processed image which resulted in creation of a structure which can be meshed for numerical solution. A skeleton structure was created on the micrograph with 210 x-elements and 140 y-elements. This skeleton was modified to increase the homogeneity of elements. It was performed by using different tools such as smooth, snap anneal, snap refine, to increase the smoothness of skeleton. It could produce 120,916 nodes, and total of 204,680 elements including 168,462 triangles and 36,218 quads ones with the homogeneity factor of 0.9886. The skeleton was meshed according the above mentioned condition. The final status of the produced skeleton is shown in the Table 10.

Table 10. Skeleton status created and modified by OOF.

Number of nodes	*Number of elements*	*Triangle elements*	*Quadratic elements*	*Homogeneity index*
120916	*204680*	*168462*	*36218*	*0.9886*

Figure 23 shows the meshed image ready for application of force or stress. The distribution of elements around different microstructural features are shown in inset image in this figure. As mentioned before, the accuracy of the simulation will be greatly improved by annealing process.

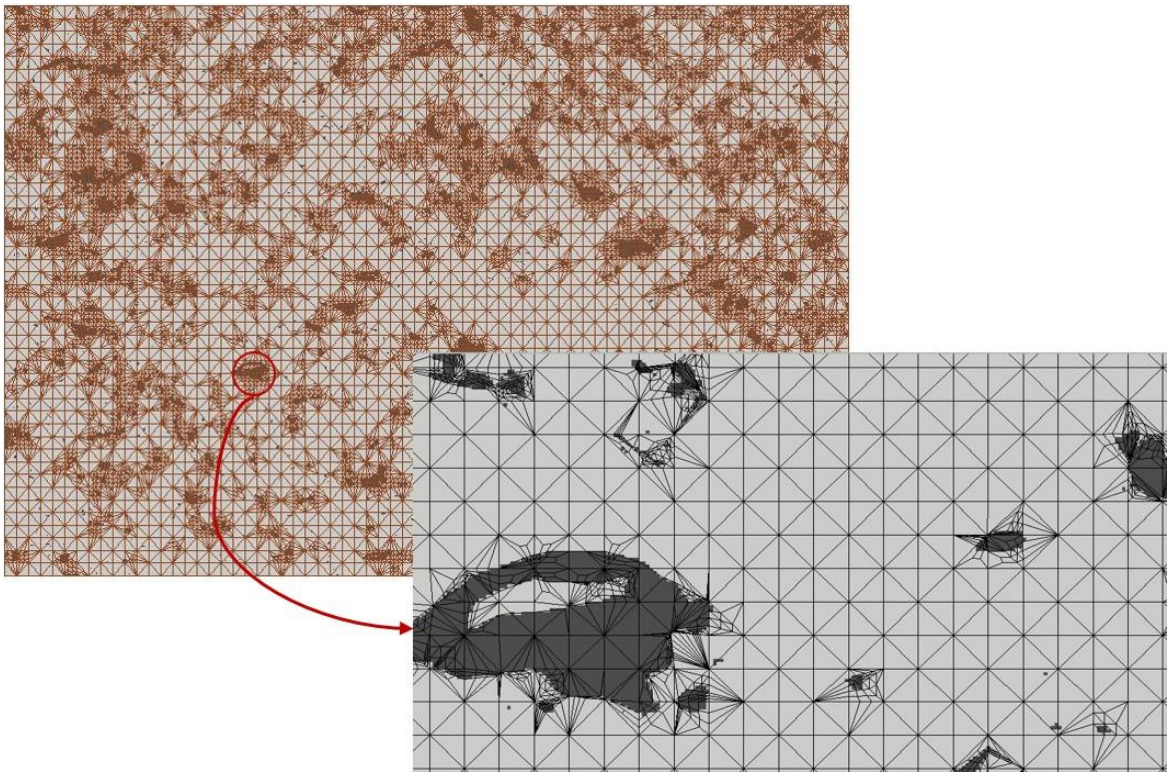

Figure 23. Skeleton and Mesh structure on the micrograph of Al-15Zn coating.

The FEA method used in this study was able to solve a Force Balance problem with a defined in-plane displacement. In boundary conditions section, we fixed the left and right sides of the image. A displacement less than the strain at yielding of bulk Al-15Zn should be applied to the boundary of the structure to avoid yielding of the coating. Considering the yield strength and Young's Modulus of pure aluminum, we can derive a yielding strain of 0.002. Therefore, it is safe to apply a displacement of 0.0002 to the right boundary and parallel to the coating plane. The opposing side is set to be fixed, while the top and bottom boundaries are set free. After solving the mesh, the average values of stress and strain in the x-direction over the entire mesh is calculated by FEA analysis. A report from a solved problem, including the average stress and strain from OOF program is shown in Figure 24.

Using the Equation (1), the Young's modulus of the Al-15Az coating could be estimated using object oriented finite element analysis. To achieve a more accurate magnitude of the Young's modulus, this process is repeated for other randomly taken micrographs as well.

$$E = \frac{\sigma_{xx}(1-\nu)}{\varepsilon_{xx}} = 46.7988\,GPa \qquad (1)$$

```
# Operation: Average
# Output: Geometric Strain[xx]
# Domain: EntireMesh
# Sampling: ElementSampleSet(order=automatic)
# Columns:
# 1. time
# 2. average of Geometric Strain[xx]
0.0, 9.68992248062e-08

# Operation: Average
# Output: Stress[xx]
# Domain: EntireMesh
# Sampling: ElementSampleSet(order=automatic)
# Columns:
# 1. time
# 2. average of Stress[xx]
0.0, 6.66877848788e-06
```

Figure 24. Reported solution by OOF from image analysis of one of the images.

The results show more than 40% reduction in the elastic modulus compared to a bulk of Al-15Zn which is mainly caused by the voids and porosities in the microstructure of the deposited coating. The results are listed in the Table 11.

Table 11. OOF finite element analysis results on two different micrographs.

Group	*Average Strain*	*Average Stress*	*Young's Modulus (GPa)*
Micrograph I	*9.6899e-08*	*6.6687e-06*	*46.7988*
Micrograph II	*1.1675e-07*	*7.5497e-06*	*43.9713*

2.3.2.4.2 Cold Sprayed Coating

Several micrographs were taken from randomly selected positions along the cross-section of the cold sprayed coating using optical microscopy. Figure 25 shows an optical micrograph of the as-sprayed coating.

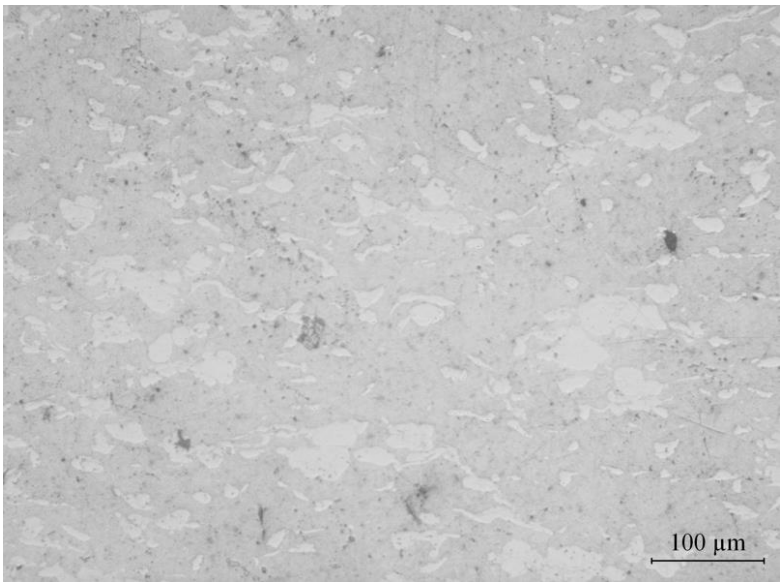

Figure 25. Optical microscopic image of Al-15Zn cold sprayed coating cross-section.

According to Figure 25, there are three different regions on the microstructure of the coating consisting of voids (black), zinc (light gray), and aluminum (dark gray). Therefore, three different groups are created and pixels from each region are added to their corresponding group. As mentioned in the earlier report, pixels are selected based on their contrast using RGB method in Pixel Selection menu. Table 12 shows the number of pixels and percentage of each group.

Table 12. Number of pixels and percentage of each group.

Group	*Number of Pixels*	*Percentage*
Al	*2322188*	*80.61*
Zn	*525085*	*18.22*
Pores	*33681*	*1.17*
Total	*2880800*	*100*

In the materials menu, values of E and ν are determined for each group based on the values from Table 13. Since the elastic modulus cannot be set to zero, a really small number such as $1\times e^{-9}$ GPa, is assumed for the elastic modulus of voids and pores.

Table 13. Mechanical properties of different regions for Al-15Zn cold sprayed coating.

Group	*E (GPa)*	*ν*
Al	*70*	*0.34*
Zn	*100*	*0.25*
Pores	*10-9*	*0.3*

Then, colors are assigned to each group to properly distinguish them from one another. Figure 26 shows the modified image.

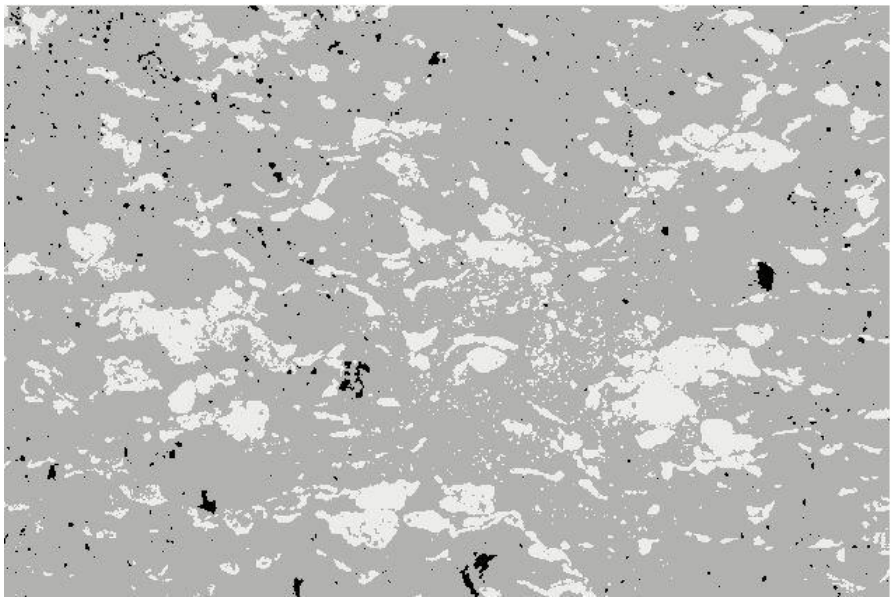

Figure 26. Modified image: black, dark, and light pixels representing voids, aluminum, and zinc, respectively.

In the next step, elements are created based on the modified image and produced an elemental structure for numerical simulation consisted of 210 x-elements and 140 y-elements. This skeleton is further modified to increase the homogeneity of elements. Modification process includes smooth, snap anneal, and snap refine which is shown in Figure 27. The final skeleton reached a homogeneity of 0.982.The OOF method can solve a Force Balance problem with defined boundary conditions and displacements. Fixed boundary is considered for the left side of the image, while displacement is applied on the opposite side of the image. Considering, the strain at yielding and Young's modulus of both pure aluminum and zinc, a displacement of 0.0002 would be satisfactory to avoid yielding of the coating. As for top and bottom of the image, boundary conditions are set free. After solving the problem, the OOF can report average values of stress and strain over the entire mesh shown. Average values of stress and strain in x-direction are shown in Figure 28.

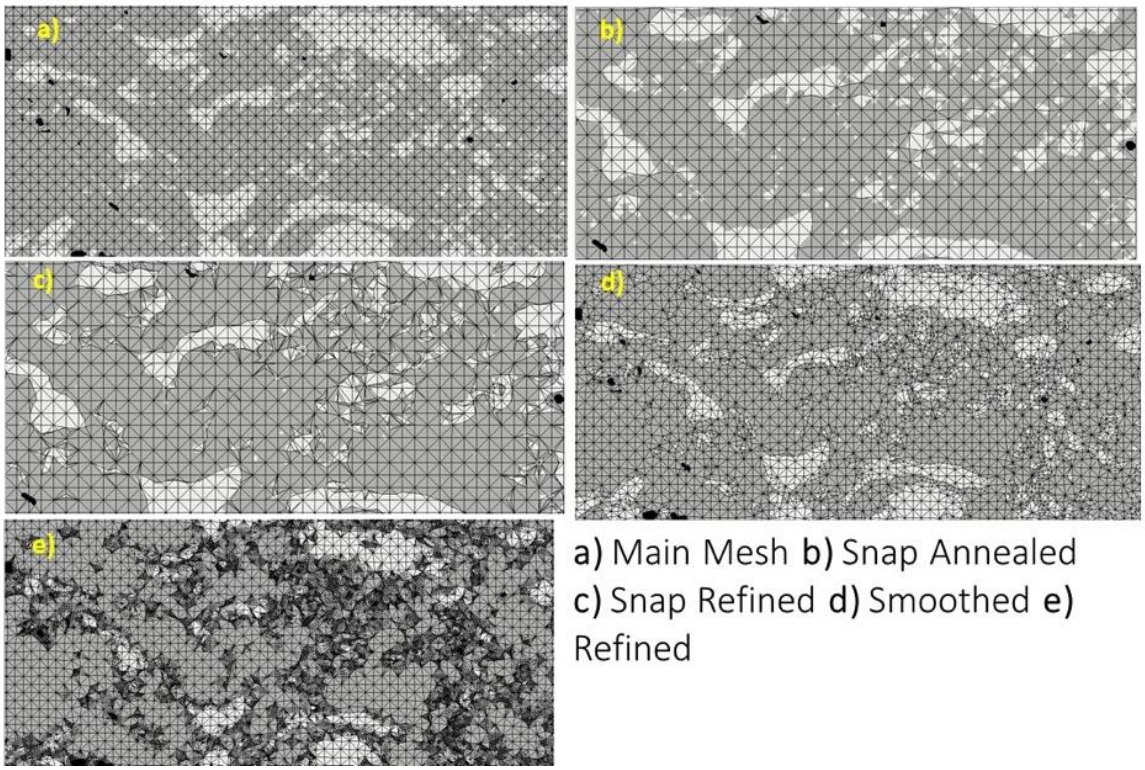

Figure 27. Image modification process.

```
# Operation: Average and Deviation
# Output: Geometric Strain[xx]
# Domain: EntireMesh
# Sampling: ElementSampleSet(order=automatic)
# Columns:
# 1. time
# 2. average of Geometric Strain[xx]
# 3. standard deviation of Geometric Strain[xx]
0.0, 9.61538461538e-08, 2.83474693705e-07
```

```
# Operation: Average and Deviation
# Output: Stress[xx]
# Domain: EntireMesh
# Sampling: ElementSampleSet(order=automatic)
# Columns:
# 1. time
# 2. average of Stress[xx]
# 3. standard deviation of Stress[xx]
0.0, 7.6482643062e-06, 1.61843833634e-06
```

Figure 28. Average values of stress and strain reported by OOF.

By substituting the average values into Equation (2), the Young's modulus of the cold sprayed Al-15Zn coating can be estimated using object oriented finite element analysis.

$$E = \frac{\sigma_{xx}(1-\vartheta)}{\varepsilon_{xx}} = 53.8499\ \text{GPa} \tag{2}$$

It should be noted that Equation (2) can be reorganized to find an average value of Poisson ratio as in Equation (3) below:

$$\vartheta = \frac{A_{Al}\vartheta_{Al} + A_{Zn}\vartheta_{Zn}}{A_{Al} + A_{Zn}} = 0.323 \tag{3}$$

To achieve more accurate results for estimating the elastic modulus of the coating, this process is repeated for other randomly taken micrographs over the coating. Table 14 lists the results of analysis on

two different micrographs which indicates that Al-Zn coating is weaker than zinc or aluminum in terms of elastic modulus, yet it has shown better properties than the wire arc coating analysis performed in the previous report.

Table 14. OOF results on two different micrographs.

Group	*Average Strain*	*Average Stress*	*Elastic Modulus (GPa)*
Micrograph I	*9.6153e-08*	*7.6482e-06*	*53.8499*
Micrograph II	*1.4367e-07*	*1.1505e-05*	*54.0544*

2.4.5. Corrosion performance for different coatings

To determine which coating materials and coating techniques has the best corrosion performance, laboratory electrochemical accelerated corrosion tests were performed. PVC pipes with inner a diameter of 1 inch and a length of 3 inches were fixed on top of the coating surface using Loctite epoxy adhesive. The PVC pipes were filled with 3.5wt% NaCl solution as electrolyte for electrochemical corrosion test. To prevent any leakage during the test, samples were cured 24 hours in room temperature to maximum the bounding strength of adhesive. Figure 29 showed the schematic of corrosion test and Figure 30 illustrates the actual test set-up in this study.

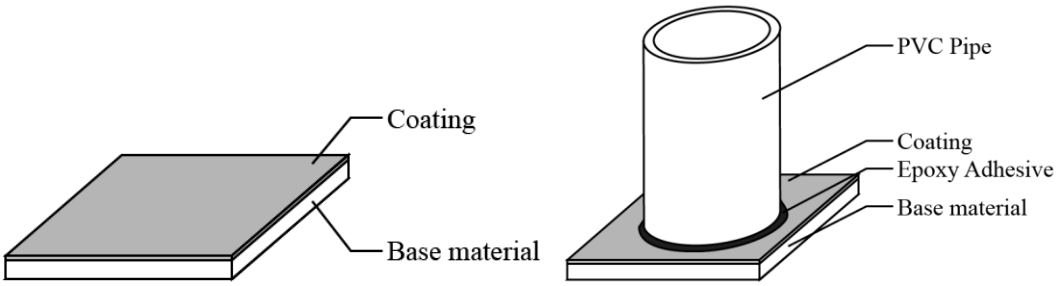

Figure 29. Schematic of sample layout.

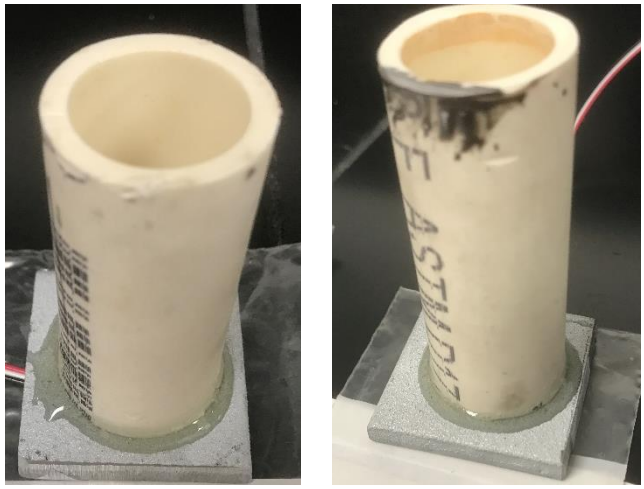

Figure 30. Samples before electrochemical test (left: Sample #1; right: Sample #2).

It was important to compare corrosion properties of cold sprayed Al-Zn with the one deposited by wire arc spray technique. Since the size of cold sprayed sample was relatively small, a PVC pipe was attached to the sample instead of standard tubes. After using epoxy to glue PVC pipe to the surface of the coated sample, a conductive wire was attached to the bottom of the sample to connect testing instrument. Figure 31 shows the inner diameter of the PVC pipe with attached connecting wires.

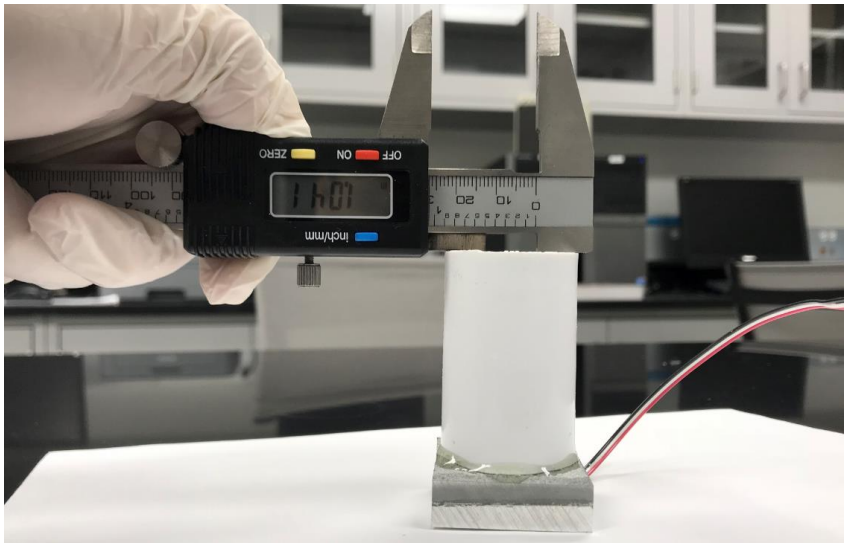

Figure 31. Inner diameter of the PVC pipe attached to sample to be tested.

Accelerated electrochemical corrosion test was carried out with a Gamry Reference 600 Potentiostat/Galvanostat/ZRA instrument. Figure 32 shows the detailed layout of samples, instruments, and their connection in between. As mentioned before, 3.5wt% NaCl solution was filled in PVC pipe as electrolyte. Working electrode was first connected to a generic electric wire, and the wire was attached to the bottom side of sample for better connectivity (due to thickness of the samples, clips of working electrode cannot be applied to samples directly). Platinum was used as inert metal, and AgCl with KCl solution were used in reference bar. The reference bar was calibrated before test. White tapes were used to avoid reference bar and inert metal touching each other. For each sample, one Tafel test and one polarization test were conducted. The real picture of accelerated electrochemical corrosion test set-up in this study is shown in Figure 33.

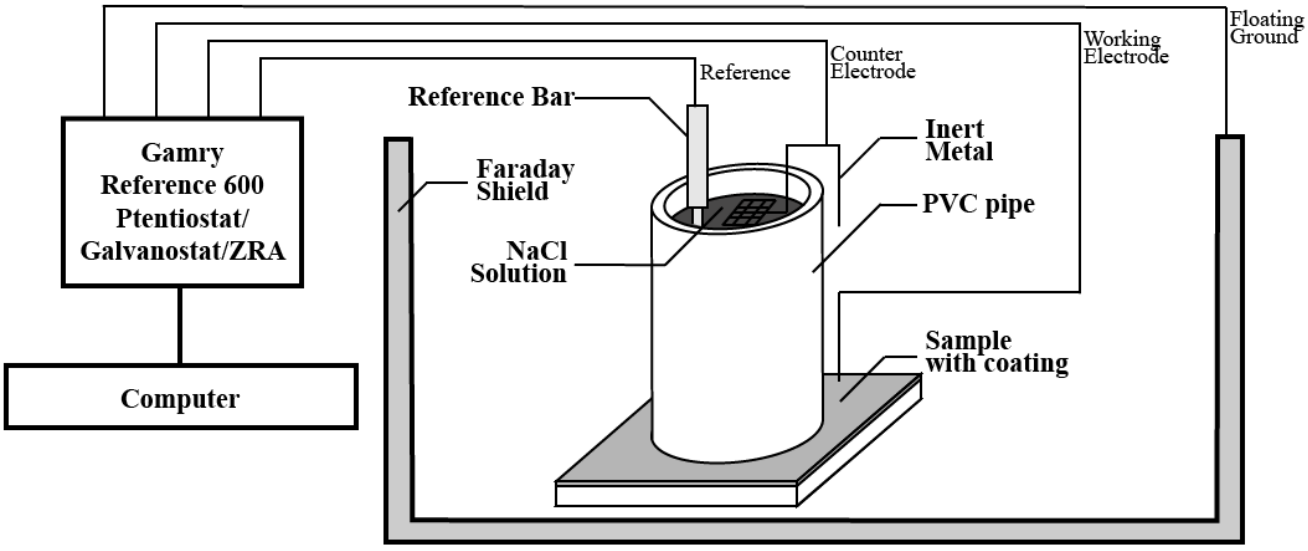

Figure 32. Schematic of the accelerated electrochemical corrosion test setup.

Figure 33. Accelerated electrochemical corrosion test setup.

Figure 34 shows a general Tafel test result with detailed markers. Tafel curve was drawn by applying an incremental potential (x-axis) over counter electrode and working electrode, and measuring the current (y-axis, in logarithmic scale) in this system. The lowest point of the curve indicated that anodic reaction and cathodic reaction reach an equilibrium. The corresponding potential at that lowest point was open circuit potential or corrosion potential. The curve left to corrosion potential part was cathodic range, and in right side of the graph anodic range could be found. Tafel fit was conducted on the linear part of both cathodic and anodic range. Thus, two straight lines representing cathodic and anodic current should be carried out. The corresponding current to the intersection of these two straight lines is corrosion current. The slope of anodic range (called Tafel parameter A), together with corrosion potential and corrosion current, serve as three major indicators for corrosion resistance in Tafel test.

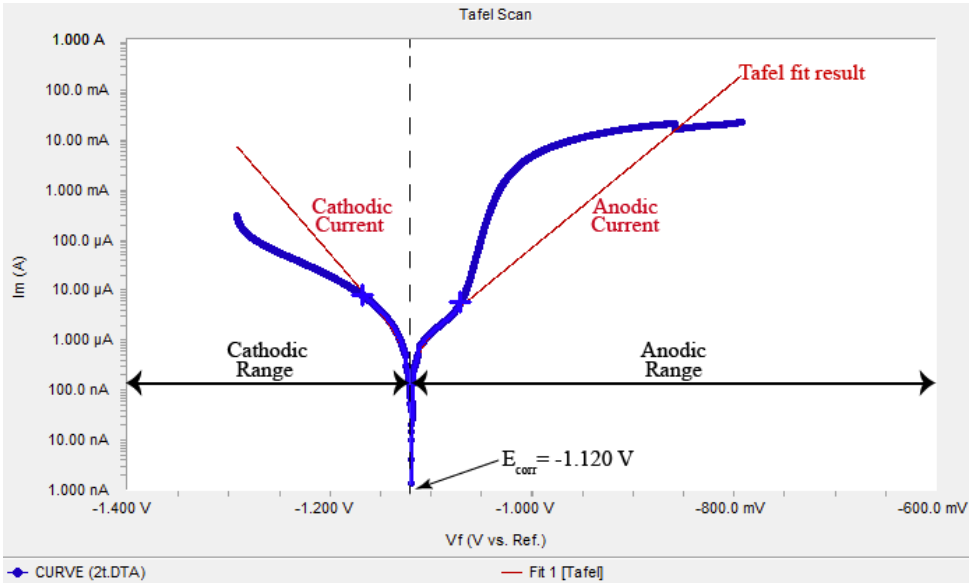

Figure 34. A general type of Tafel curve showing anodic and cathodic range.

By curve fitting on the linear part of both anode and cathode sides of the Tafel curve, the corrosion current could be calculated. With equation (5), corrosion rate could be assessed.

$$I_{corr} = \frac{\beta_A \beta_C}{2.303 R_p (\beta_A + \beta_C)} \quad (4)$$

$$\text{Corrosion Rate} = \frac{K W_E I_{corr}}{AD} \quad (5)$$

Figure 35 compared the Tafel graph of wire arc sprayed Al-Zn coating with other coating materials and the steel substrate material including the previously reported HVOF deposited copper coating and Al-Bronze. It can be seen that in Al-Zn coating the graph shifted to the more negative corrosion voltage (Ecorr) and lower corrosion current density (Icorr) compared to the bare steel sample. This was

expected and attributed to higher electronegativity of AL-Zn compared to the substrate which made the corrosion initiation took place at lower potentials. Figure 36 presents the electrochemical corrosion test result (Tafel curve) for the cold sprayed Al-Zn coating.

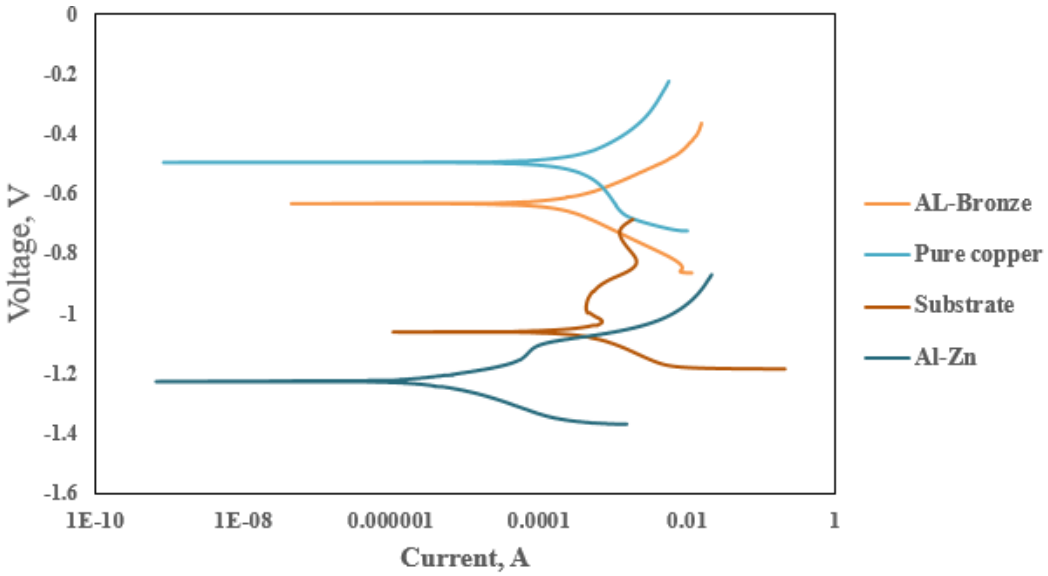

Figure 35. Tafel curves obtained for various thermally sprayed coatings in 3.5% NaCl solution. (The curve obtained from steel substrate is shown for the reason of comparison).

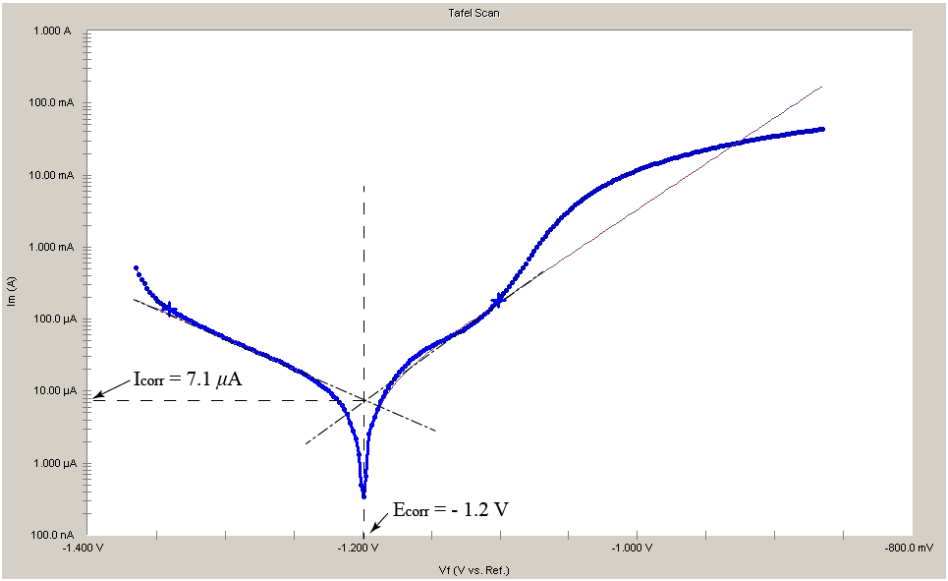

Figure 36. Tafel curve of tested sample.

The corrosion parameters resulted from the potentiodynamic polarization test have been listed in Table 15. The corrosion rate for cold sprayed Al-Zn is 0.595 mil/year compared to 0.66 mil/year for HVOF deposited Al-Bronze and 0.22 for HVOF deposited Cu. All these thermal sprayed metallic coatings have at least three times better than bare steel with corrosion rate higher than 1.82 mil/year. The cold sprayed Al-Zn coating has slightly higher corrosion rate than the arc wire sprayed Al-Zn coatings, which had a corrosion rate of 0.11 mil/year (ten times better than bare steel), in corrosion resistance aspect. It is worth mentioning that no optimization was applied to operational process parameters of spraying process and the coating was deposited only based on experience of the operators. As it can be seen in this table, Al-Zn coating showed very low value of corrosion current density (Icorr=0.736µA/cm^2). Overall, wire arc sprayed Al-Zn coating possessed the lowest corrosion rate of 0.11 mpy among the other materials produced and tested in this study. In an open water system,

a corrosion rate of around 1 mpy for steel is normal and if it has a corrosion rate of around 10 mpy, action should be taken right away. A corrosion rate of 0.11 mpy is well below the concerned rang of corrosion and the coating is able to protect the steel substrate well.

Table 15. Corrosion performance comparison between different coating materials.

Material	*Corrosion Potential, Ecorr (mv)*	*Corrosion Current Density, icorr (μA/cm^2)*	*Corrosion Rate (mill/year)*
Substrate	*-1062*	*638.3*	*1.82*
HVOF deposited Al-Bronze	*-632.7*	*0.641*	*0.66*
HVOF deposited Cu	*-495.1*	*1.956*	*0.22*
Wire Arc deposited Al-Zn	*-1173*	*0.736*	*0.11*
Cold sprayed Al-Zn	*-1200*	*7.1*	*0.595*

2.4 *Optimization of Coating Thickness (Task 2.4)*

To investigate the influence of thickness on coating quality and corrosion performance, wire arc coatings with different thickness were coated and studied. Figure 37 shows the wire arc sprayed Al-Zn (85 wt% Al—15 wt% Zn) coatings deposited on steel substrate coupons at different thicknesses. Steel substrate size were 38 mm (length) × 38 mm (width) × 6 mm (height). The thickness of coating was 2mm (Sample #1) and 0.1 mm (Sample #2). Deposition with different thickness were for comparison of coating thickness regarding mechanical and corrosion behaviors of the coatings. .

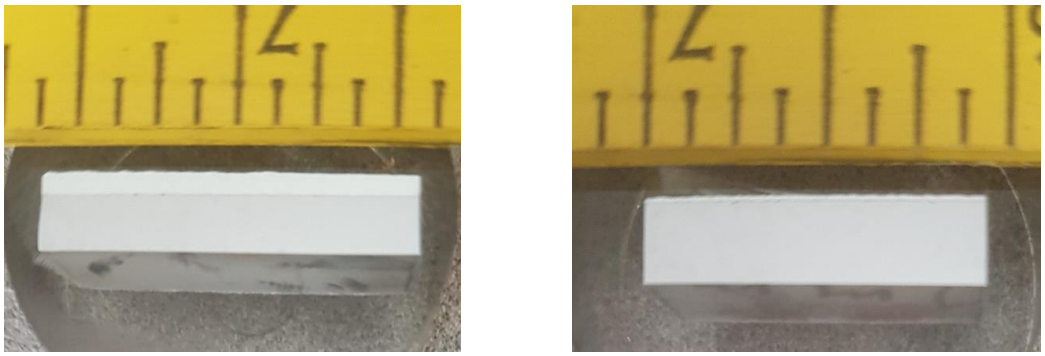

Figure 37. Mounted coating samples: Sample #1 (2mm, left) and Sample # 2 (0.1mm, right).

Figure 38 illustrates the optical micrographs taken from wire arc Al-Zn coatings with two different thicknesses (2mm and 0.1mm) sprayed on carbon steel substrates. Figure 38 indicated that both coatings were dense with no visible delamination in the interphase of the coating-substrate exhibiting good bonding between the coating and the substrate.

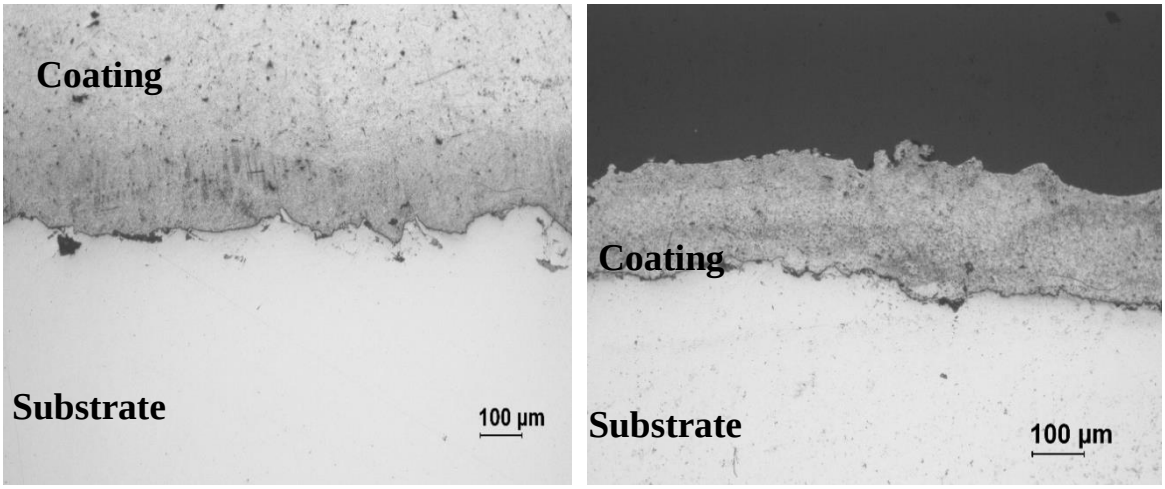

Figure 38. Optical micrographs of Wire arc sprayed Al-Zn coating on carbon steel substrate in (left) 2mm and (right) 0.1mm thicknesses.

To investigate the influence of coating thickness of the corrosion performance of the coating, laboratory electrochemical tests were performed and detailed as in the following sections. Figure 39 showed Tafel test results of Sample #1 and #2.

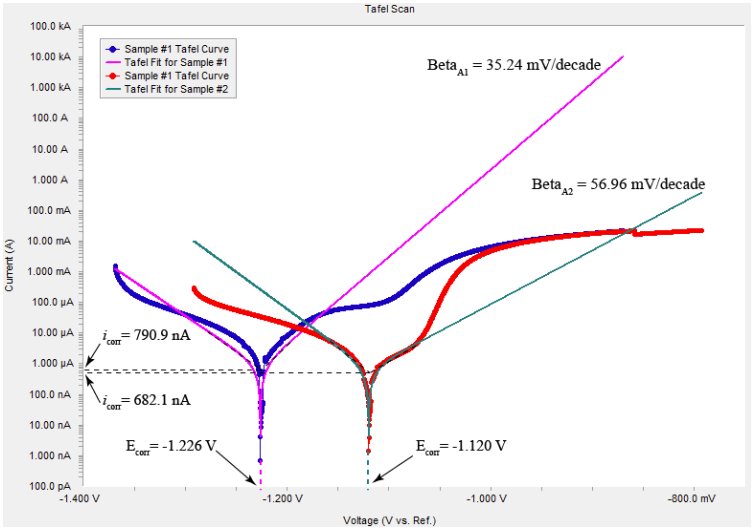

Figure 39. Tafel curve of Sample #1 and Sample #2.

Table 16 listed the corrosion rate of each sample and parameters that contribute to the corrosion resistance. The corrosion rates of both samples were close to each other, which were around 0.11 mpy range.

Table 16. Measured Corrosion Rate and Major Corrosion Resistance Indicators for Coated Samples

Sample Number	*Corrosion Rate (mil per year)*	*Corrosion Potential (V)*	*Corrosion Current (A)*	*Anode Tafel Parameter β_A (mV/decade) ×10-3*
Sample #1	*0.1151*	*-1.226*	*7.90 × 10-7*	*35.24*
Sample #2	*0.0993*	*-1.120*	*6.82 × 10-7*	*56.96*

Since, the unit of 1mpy=0.0254 mm/y, the Al-Zn coated sample with 0.1 mm thickness (Sample #2) has a corrosion rate of 0.0993mpy, which yields to 0.0025mm/y. Therefore, a thickness of 0.1mm thin of wire arc sprayed Al-Zn coating on top of base steel material could protect the steel substrate from corrosion for about 40 years. Sample #1 with 2 mm layer of coating has a corrosion rate of 0.1151mpy,

which yields 0.0029mm/y. A thicker coating of 2mm wire arc sprayed Al-Zn coating could protect the steel substrate again corrosion for over 690 years if no other external factors such as external damages are to be considered. Thus, for practical application, depends on the design life of the coatings and the pipes in service, the thickness of the coatings can be determined based on the initial expected corrosion rate. For a design service life of 100 years, a thickness of around 0.28mm (280μm) of wire arc sprayed Al-Zn coating is recommended if no sealing technology is applied.

Tables 16 also showed that the thickness of the coating will not significantly influence the corrosion rate of the coatings. However, the measured data in Table 16 indicated that a thinner coating (Sample #2) has slightly slower corrosion rate when compared to a thicker coating (Sample #1). Sample #2 which has a thinner coating has slightly better corrosion resistance because: 1) Sample #2 has less corrosion rate; 2) Sample #2 has a corrosion potential closer to zero, which indicates it is more difficult for corrosion formation to initiate on this sample; 3) Sample #1 has a lower corrosion current, which matches the calculated lower corrosion rate, indicating the corrosive chemical reactions have less reaction rate; and 4) Higher Tafel parameter β_A indicates that for each one decade increase in current, it requires more potential or energy, thus the corrosive chemical reaction rate tends to be lower. However, since only less than 15% difference was observed between Sample #1 and #2 and only one pair of samples were tested, we cannot yet conclude that for all arc-wired sprayed Al-Zn coatings, thicker coating yields better corrosion resistance. Thus, average corrosion rate is suggested to use for coating thickness design for practical application for conservative design purposes.

2.5 Coating Sealing Approaches (Task 2.5)

Soft coatings are proposed to be applied for sealing hard coatings to increase protection of coatings against corrosion. Epoxy (Duralco 4460 from Cotronics Corp.) have been investigated as sealing materials in this study. Figure 40 illustrates three samples prepared to investigate the sealing properties of soft coating. The three samples plates (noted as Sample #S1, #S2, and #S3) were made of A36 structural steel and the thickness of epoxy coatings were 1mm. The corrosion tests run nine months, resulting in 6,400 hours of monitoring time span. Figures 41 ~ 43 show the visual inspection results of all the samples on Day 30, Day 150, and Day 270. Visual inspections on the samples show that the soft coating generally had good sealing effect with possibility of localized damages for pitted corrosion. For 150 days, no obvious corrosion was observed under the soft coating. Cracks were made on the soft coating on 150 days of test to simulate the external damages. With external damages such as cracks on soft coatings, corrosion may occur as shown in the visual inspection after 270 days. It is obvious that the soft coating could reduce corrosion rate and could compliment hard coatings toward corrosion protection.

(a) (b) (c)

Figure 40. Visual inspection result at Day 1for: (a) Sample #S1, (b) Sample #S2, and (c) Sample #S3.

(a) *(b)* *(c)*

Figure 41. Visual inspection result at Day 30 for: (a) Sample #S1, (b) Sample #S2, and (c) Sample #S3.

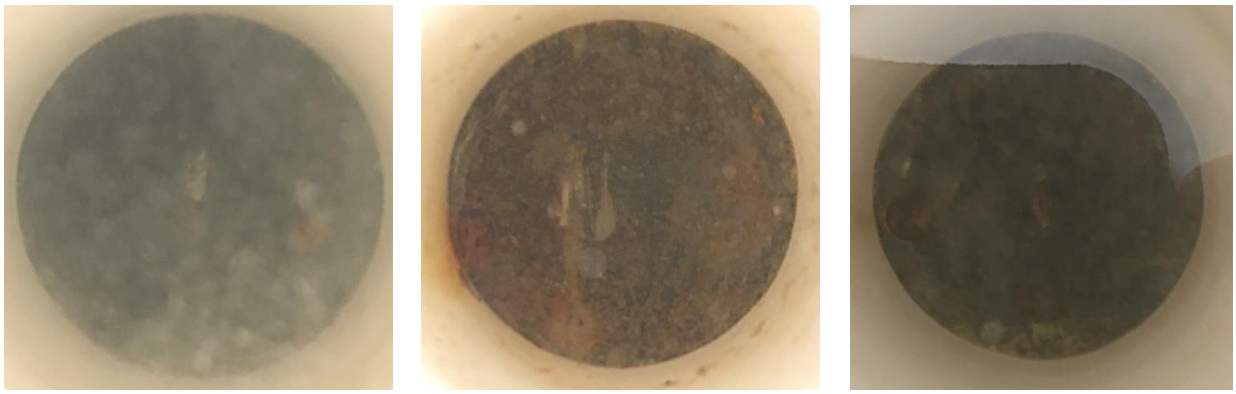

(a) *(b)* *(c)*

Figure 42. Visual inspection result at Day 150 for: (a) Sample #S1, (b) Sample #S2, and (c) Sample #S3.

(a) *(b)* *(c)*

Figure 43. Visual inspection result at Day 270 (Jun 18th, 2017) for: (a) Sample #S1, (b) Sample #S2, and (c) Sample #S3.

2.6 Cathodic Protection Improvements (Task 2.6)

The pipe-to-soil potential is the voltage difference between a buried metallic pipe and the soil surface. The cathodic protection will require a protective current with at least -0.85 volts measured between the pipe and a saturated copper-copper sulfate half-cell, which is called the pipe-to-soil potential. Figure 44 shows how to measure the soil-to-pipe potential in the field [15].

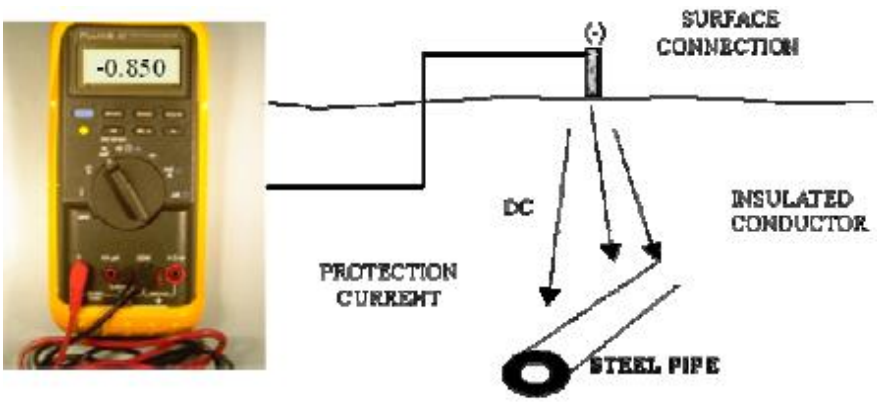

Figure 44. Field measurement example for pipe-to-soil potential[15].

Different coating materials have different soil-to-metal potential, and Table 17 listed of the potentials which typically measured in nature soil conditions[15] for the materials similar or close to the ones used in this study.

Table 17. Soil-to-Metal Potentials for Various Materials [15]

Metals	*Potentials (Volts)*	*Required Additional Cathodic Current (Volts)*
Mild steel (clean)	*-0.5 ~ -0.8*	*At least -0.35*
Mild steel (rusted)	*-0.2 ~ -0.5*	*At least -0.65*
Copper (Cu), Bronze	*-0.2*	*At least -0.65*
Pure aluminum	*-0.8*	*At least -0.05*
Aluminum alloy (5% Zinc)	*-1.05*	*Not needed*
Zinc	*-1.1*	*Not needed*

From Table 17, it can be seen that, for a clean steel substrate, an additional current of -0.35 V is required for cathodic protection; for HVOF coated Cu, an additional current of -0.65 V is needed; for HVOF coated Al- Bronze, an additional current between -0.05 ~ -0.65 V may be needed; and for wire arc deposited and cold spayed Al-Zn, no additional current is needed for cathodic protection. If less cathodic protection is a demand, wire arc or cold sprayed Al-Zn coatings will be the fit candidates for pipeline coatings with no dependence on additional cathodic protection.

3 Pipeline Corrosion Risk Management Using an In-line Assessment System (Task 3, Completed)

3.1 Quantitative Corrosion Assessment Using the Embedded Fiber Optic Sensors (Task 3.1)

3.1.1. Theoretic Study

By embedding fiber optic sensors, specifically, fiber Bragg grating (FBG) sensors, inside coatings or adhesives as shown in Figure 45(a), the sensor senses strain in the coating or adhesives induced by expansions from corrosion products as seen in Figure 45(b). Initiation and formation of pitting corrosion results in sudden increase in volume and "lift up" of both the adhesive and the FBG sensor, which may result in delamination and detachment of them from steel plate.

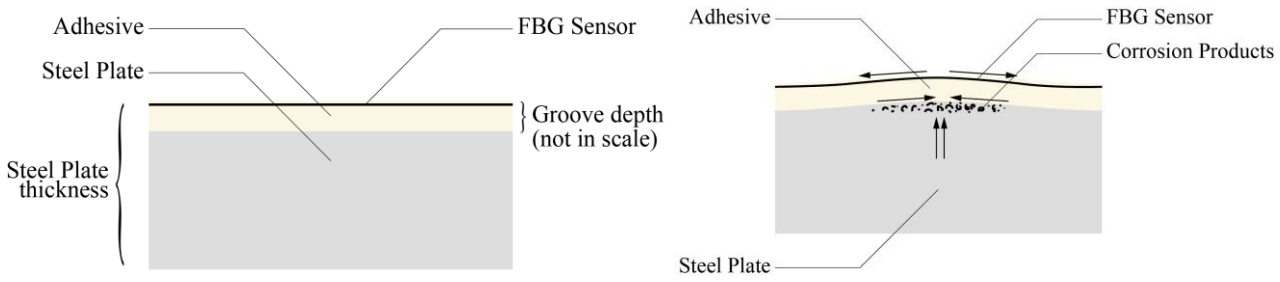

Figure 45. (a) Cross-section of the steel with sensors embedded inside coatings and (b) Lift-up effects of corrosion products.

In the case of pure pitting corrosion the coatings or adhesive act as a simple supported beam as the middle part of it detaches from steel plate while the side part is still attached to steel plate. The lift-up phenomenon can serve as a displacement acted in the middle of the beam (shown in Figure 46).

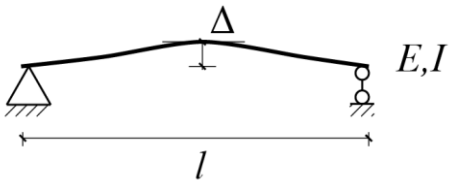

Figure 46. Simplified model of lift-up effects of corrosion products.

In steel, corrosion products have an average of 6 times in volume occupation of the original material. However, studies showed the porosity of corrosion product is around 30% ~ 50%. Thus, if the space around corrosion reaction is limited, part of the pores could be eliminated, the total increase in volume in compacted space scenarios would be less than ones in open space scenarios. The displacement (Δ) in model could be around 1% ~ 5% of total span.

On the other hand, uniform corrosion will have more complicated impact on the interaction between steel and coatings or adhesive, resulting in a different boundary condition for the sensor. Thus, the pattern of sensor's reading for pitting corrosion or uniform corrosion inside the coating will be different which could reveal the corrosion pattern through monitoring.

The strain on the embedded FBG sensor induced by the pit corrosion in the middle of span can then be calculated as:

$$\varepsilon = \frac{\sigma}{E} = \frac{My}{EI} = \frac{ly}{2EI} \cdot F \qquad (6)$$

where E is the Young's modulus of adhesive, σ is the stress on the sensor, M is the moment induced by the concentered force, I is the moment of inertia of the adhesive section, l is the span of sensor, and y is

the vertical distance between the surface and the location of the sensor, which is assumed to be half of the height of cross-section in this analysis. Thus, the displacement in middle span can be calculated as:

$$\Delta = \frac{Fl^3}{48EI} = \frac{l^3}{48EI} \cdot F \tag{7}$$

Let $k_1 = ly/(2EI)$, and $k_2 = l^3/(48EI)$. Then relationship between the strains on FBG sensors and the corrosion induced displacements can be described as a linear relationship as:

$$\varepsilon = k_1 \cdot F = \frac{k_1}{k_2} \cdot \Delta = \frac{24y}{l^2} \cdot \Delta \tag{8}$$

Let $k_3 = \frac{k_1}{k_2} = 24y/(l^2)$, thus, it is clearly that the strains on the FBG sensor is linearly proportional to the corrosion induced displacements in the middle span, which is only related to the location of the embedment of the sensor and the length of the sensor. This result matches the simulation result performed with ANSYS in the last quarter, which is shown in Table 4. In the simulated simple-supported beam system, it can be obtained in this analysis, $k_3 = k_1/k_2 = 6.1$.

From geometry, it obvious that the total volume change of corrosion products (V) have a linear relationship with the corrosion induced displacement (as volume increased linearly corresponding to the increase in height), which can be described as

$$V = k_4 \cdot \Delta = l\Delta/2 \tag{9}$$

The corrosion rate (CR) is the derivative of the total mass reduction of the steel material, or the mass increase, m, of the corrosion products, which is linearly proportional to the density, D, of the corrosion products and their volume, V, change with respect to time, which can be explained as below:

$$\mathrm{CR} = \frac{dm}{dt} = D\frac{d(V)}{dt} = k_5\frac{d(V)}{dt} \tag{10}$$

From equations (9) ~ (11), and let $K = k_4k_5/k_3 = Dl^3/24y$, the relationship between corrosion rate and strains monitored by the FBG sensor can be described as:

$$\mathrm{CR} = K\frac{d\varepsilon}{dt} = K \cdot A \cdot \frac{d\lambda}{dt} \tag{11}$$

Since $d\varepsilon/dt$ is linearly proportional to the slope of the Bragg wavelength change, dλ, with an coefficient of A, and k_1, k_2, and k_3 will stay constant when the simple-supported beam system remains unchanged, the corrosion rate can be calculated directly from the Bragg wavelength change curve slope with properly calibrated scaling factor K·A.

To validate the theoretical model for corrosion detection using the embedded optical fiber sensor, a numerical simulation of a simple support beam model was performed using ANSYS as seen in Figure 47. A set of displacement values from 3% to 15% (increased by 3%) of total span was applied. The span of beam is 1/8 inch, as same as the length of pitting corrosion in the accelerated corrosion test. The cross section of beam is 1/16 in width by 1/8 in depth determined by cross section area of the pre-fabricated groove on the steel plate. The Young's modulus of beam is 504 psi at room temperature (80 ^{o}F), based on physical property of Durabond 954 adhesive using linear interpolation.

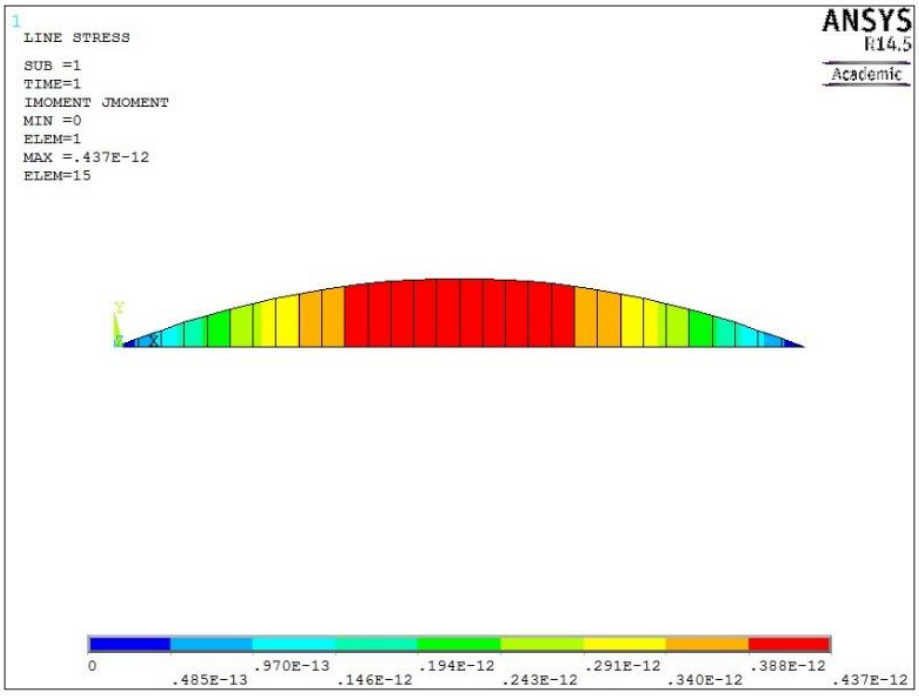

Figure 47. Numerical simulation result of simplified model.

Table 18 lists the simulation results of the average strain in the beam which a FBG sensor monitors along the grating length direction. A linear relationship could be established between the displacement and strain due to increase in volume of corrosion products.

Table.18. Average strain value result at the upper edge of beam of simulation.

Displacement (of total span)	*3%*	*6%*	*9%*	*12%*	*15%*
Strain ($\mu\varepsilon$)	*18.3*	*36.5*	*54.8*	*73.0*	*91.3*

3.2 Experimental Study

To better understand the corrosion monitoring system and validate the theoretical and numerical hypothesis of quantifying the corrosion assessment, in total of four steel plate samples named Sample #1 and #2, Sample #A and #B were prepared by embedding four FBG sensors inside Durabond 954 (from Cotronics Corp). Stainless steel based adhesive was used as filling material to create a space-restricting environment as shown in Figure 48.

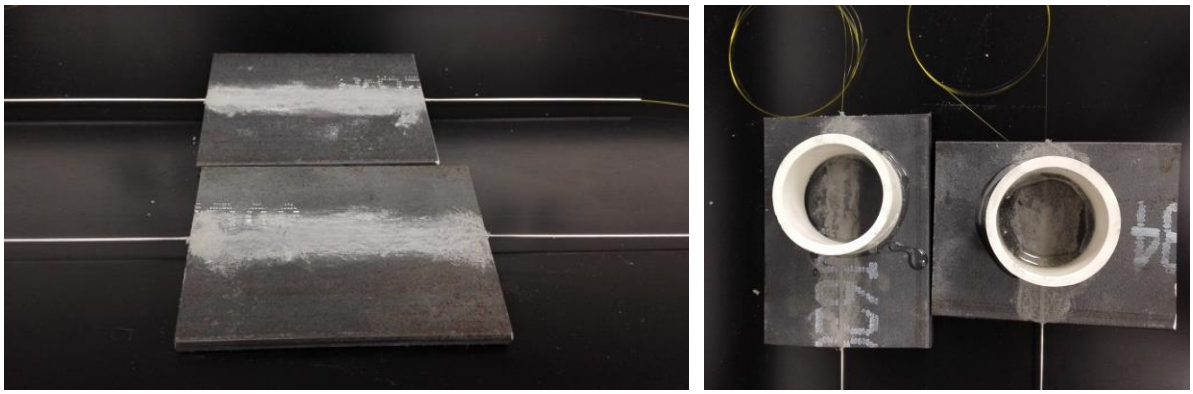

Figure 48. Steel plate sample embedded with FBG sensor.

Accelerated corrosion tests were then performed on the two samples with embedded FBG sensors by emerging them in PVC tubes filled with 3.5wt% sodium chloride (NaCl) solution for 21 days. Figure 49 presents the detail experimental setup. The center wavelength changes of the two samples

with embedded sensors had been recorded continuously for the 21 days with a sampling frequency of 10Hz. Besides, a reference sensor for eliminating the temperature effect was located.

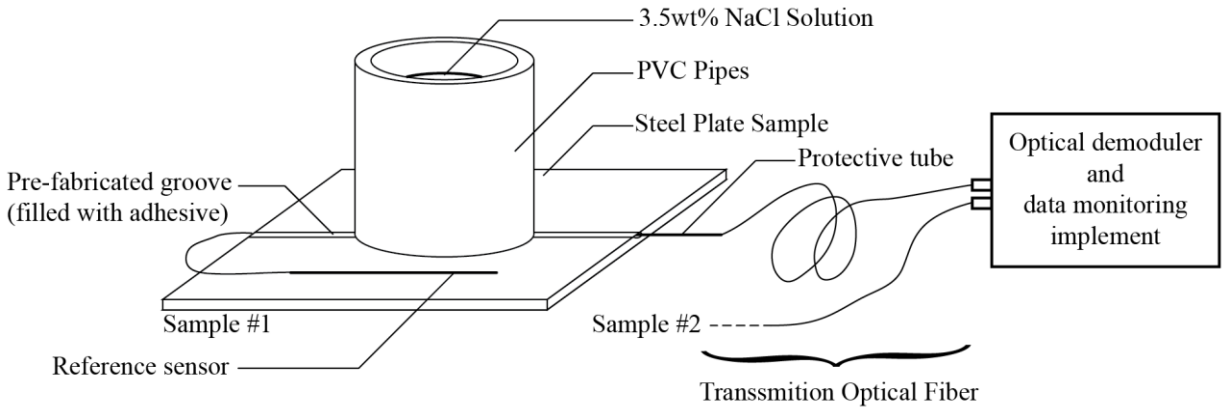

Figure 49. Schematic of an accelerated corrosion test set-up.

For Sample A and B, after the monitoring for two days, it was found that the performance of adhesive in water as shown in Figure 50 was unacceptable when compared to previous experiments. Water could easily penetrate into adhesive, causing strain release, it resulted in no Bragg wavelength change induced by corrosion. Figure 51 shows the monitored the Bragg wavelength of the two sensors with weak adhesives. It can be seen from Figure 49 that soon after adding 3.5wt% NaCl solution into the attached PVC pipe (recorded as the beginning of the experiment), the compression induced by adhesive started to release very quickly. After that, the residual strain on the FBG sensor will only come from the original compression strain induced by the curing of adhesive. It confirms that the adhesive fractured quickly after the adding of water and the breakage of the adhesive released the confinement on the embedded sensor. Thus, there is no Bragg wavelength change after the adhesive breakage. This phenomenon validated our previous hypothesis assumed for the principles of the sensor that the strains induced by the corrosion observed from the embedded fiber optic sensors come from the confinement of the adhesive or the coatings. If coating or adhesive is broken, the restrain will be released, and the strain monitored by fiber optical sensor will start to decrease, resulting noticeable Bragg wavelength change. Therefore, new adhesive have been ordered in rest experiments to guarantee a better performance.

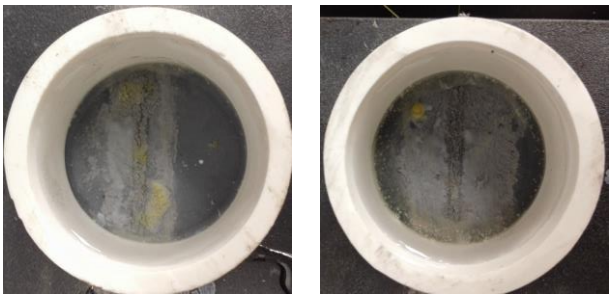

(a) Sample A *(b) Sample B*

Figure 50. Steel plate samples after 2 days for both samples.

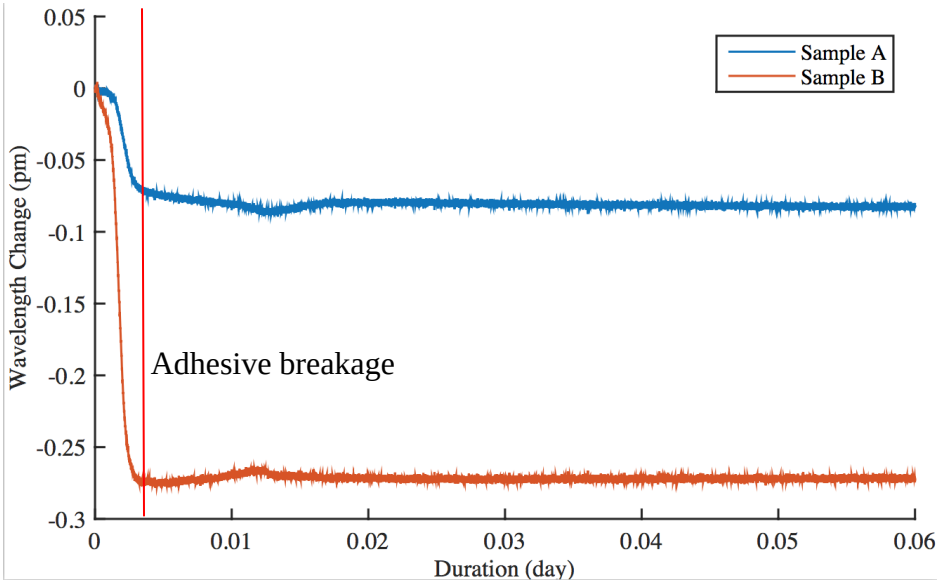

Figure 51. Bragg wavelength change curve for Sample A and Sample B.

For Sample #1 and #2, Figures 52 and 53 exhibit changes in wavelength reading during the 21-day of testing, with two conditions where temperature effects are taken to the account and eliminated, respectively. From Figure 53, it can be clearly seen that two samples have shown two different corrosion signal patterns. For Sample #1, the center wavelength of the FBG sensor increased almost linearly for the first three days. The wavelength of FBG sensor on Sample #1 changed 55 pm (from -5 pm to 50 pm) within first 2 days of experiment. It could be an indication of pitting corrosion due to the sudden corrosion occurrence. For Sample #2, the center wavelength of the FBG sensors did not show sudden changes but gradual reductions in wavelengths. Less than 20 pm of center wavelength change was found in Sample #2. It indicates a potential uniform corrosion pattern. Thus, the center wavelengths of the FBG sensor could qualitatively identify corrosion pattern as well as with the growth of corrosion.

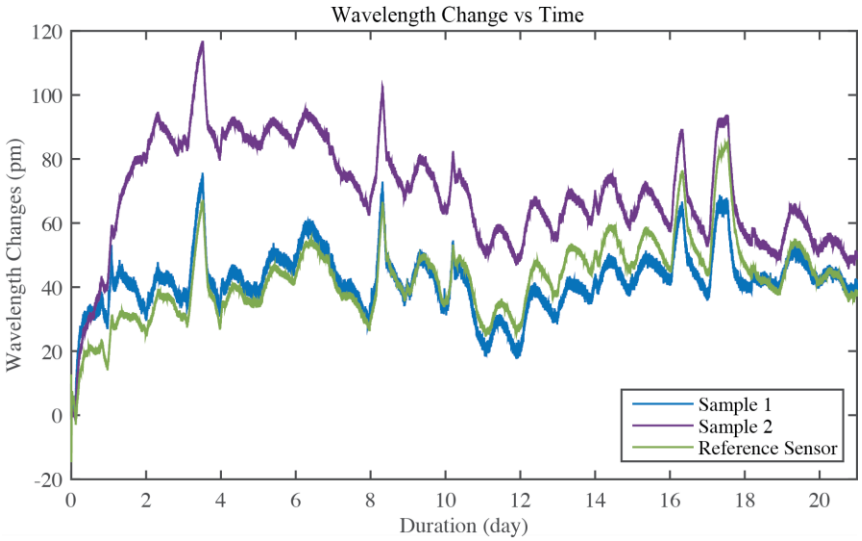

Figure 52. Wavelength change during the 21-day from accelerated corrosion test before eliminating temperature effects.

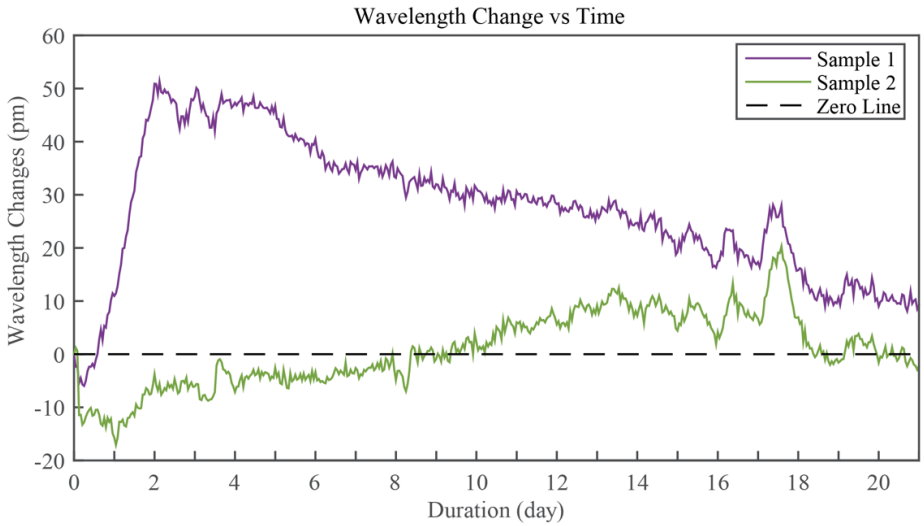

Figure 53. Wavelength change during the 21-day from accelerated corrosion test after eliminating temperature effects.

Visual inspection of two samples clearly exhibited two different corrosion patterns as shown in Figure 54 and Figure 55. Only one corroded spot has been found in Sample #1, indicating a pitting corrosion pattern, whereas, in Sample #2 a uniform corrosion pattern was detected, validating the qualitative assessment of corrosion pattern from the sensor readings. In addition, comparison between the sensor's reading for Sample #1 in Figure 53 with the numerical simulation results listed in Table 18 are in good agreement in the first three days of experimental result. This result could serve as a validation of proposed model. After 3 days, the center wavelength changes start to fluctuate around at 50 pm as steel plate got further corroded, while the simulation result still showed an increase in strain value (from 54.8 με at 9% of total span to 91.3 με at 15% of total span). This could be caused by inaccurate boundary condition and displacement applied on the model.

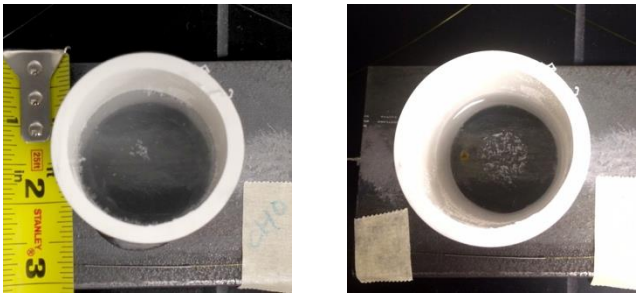

Figure 54. Visual inspection for accelerated corrosion test of Sample 1 (Left: day 1, right: day 7).

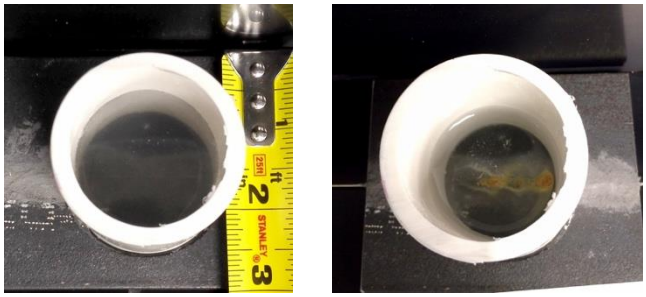

Figure 55. Visual inspection for accelerated corrosion test of Sample 2 (Left: day 1, right: day 7).

Based on a typical pitting corrosion shown in Figure 54 and 55, the two assumptions before modeling were verified. Thurs, the Bragg wavelength change rate in first two days is (with curve fitting method):

$$\frac{d\varepsilon}{dt} = 35.19 \text{ pm/day}$$

Uncoated steel generally has an average corrosion rate of 1.5 mill/year. So the scaling factor K would be

$$K = \text{CR} \cdot \left(\frac{d\varepsilon}{dt}\right)^{-1} = 0.0426$$

Thus, the scaling factor K can be used to develop system integration for an in-line corrosion assessment system in next section.

3.2. System Integration for an In-line Corrosion Assessment

To integrate the system with the coatings for an in-line corrosion assessment, the coating with most corrosion resistance, the wire arc sprayed Al-Zn coating and the soft coating as sealing are selected to be used to develop an effective system integration.

3.2.1 System Integration in Wire Arc Spraying Al-Zn Coatings

Three samples were tested in the laboratory for the system integration using the same experimental setup as previously presented in Section 3.2. The three samples were wire arc sprayed Al-Zn hard coating at different thicknesses: 1.5 mm and 2mm. All three coatings were deposited on A36 structure steel. The size of the samples was 50 mm × 50 mm. As shown in Figure 56, samples were noted as Sample #A1, #A2, and #A3. The coatings on Sample #A1 and #A2 had thickness of 2mm, and the coating on Sample #A3 had a thickness of 1.5mm. Before the accelerated corrosion test was conducted, PVC pipes were attached on top of each coated sample using epoxy by the same method as tests described in previous quarterly reports to keep consistency, as shown in Figure 57. The overall integrated system for the accelerated corrosion test is shown in Figure 58. The accelerated corrosion test has run for two weeks and the NaCl solution used in the test has a NaCl concentration of 3.5wt%.

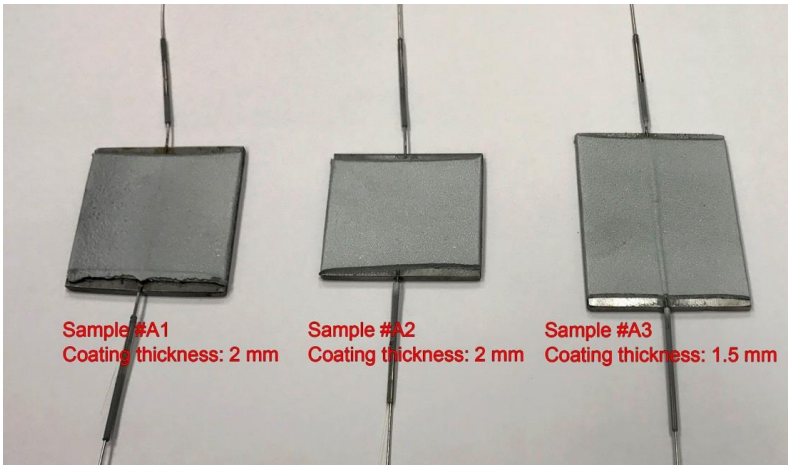

Figure 56. Three Al-Zn coated samples with FBG sensor embedded before test.

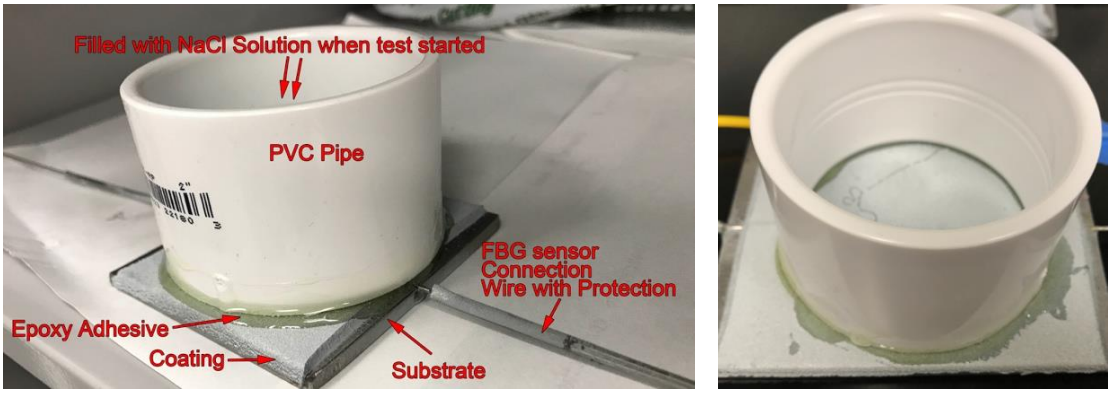

Figure 57. Sample attached with PVC pipe before corrosion test.

Figure 58. Integrated system in accelerated corrosion test setup.

Figure 59 presents the data collected from embedded FBG corrosion monitoring systems together with the data collected from the temperature compensation sensor during the two-week period (14 days). The data after temperature compensation is shown in Figure 60.

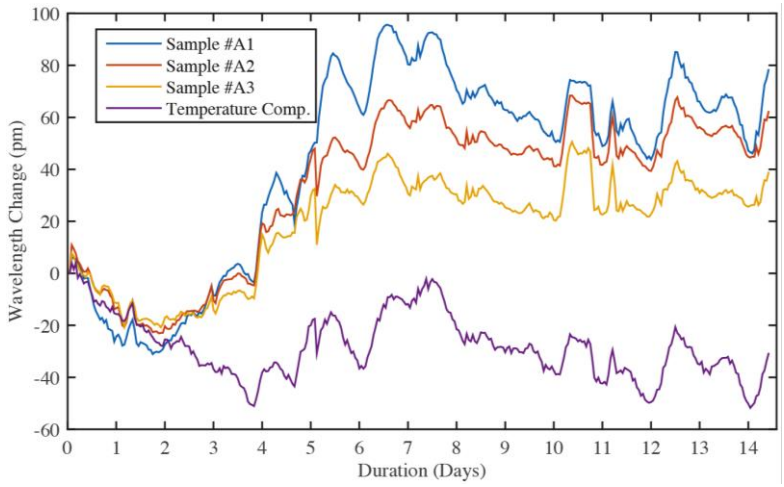

Figure 59. Bragg wavelength changes collected from FBG sensors with Al-Zn hard coating without eliminating temperature effect.

From Figure 60, the corrosion rate for each coated sample could be calculated by using the methods developed previously and reported in the past quarterly reports, and the detailed calculation results were shown in Table 19 and Figure 61. Corrosion rates listed in table were calculated with scaling factor calibrated with electrochemical corrosion test.

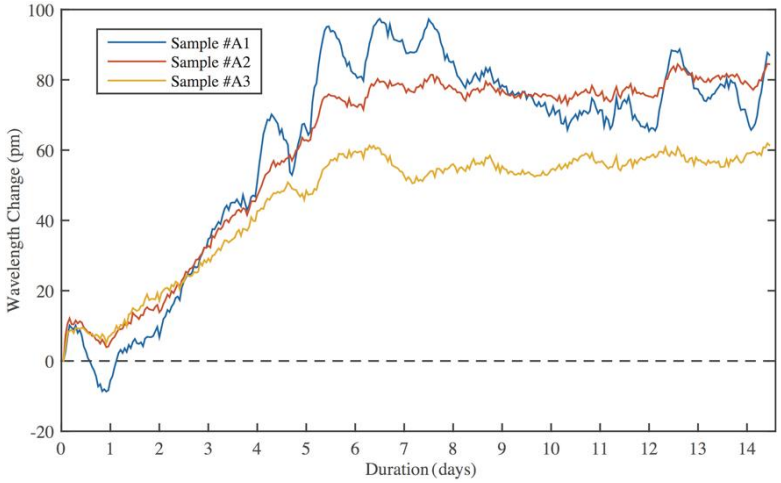

Figure 60. Bragg wavelength changes collected from FBG sensor with Al-Zn hard coating after eliminating temperature effect and de-noising.

Table 19. Corrosion rate calculation for tested samples.

Sample number	*Initial point for corrosion rate calculation*	*End point for corrosion rate calculation*	*Interval between initial point and end point*	*Corrosion rate*
Sample #A1	*-8.33 pm (23 hrs)*	*45.99 pm (86 hrs)*	*2.63 day*	*0.14 mil/year*
Sample #A2	*3.91 pm (22 hrs)*	*74.71 pm (135 hrs)*	*4.71 day*	*0.10 mil/year*
Sample #A3	*5.10 pm (22 hrs)*	*48.69 pm (115 hrs)*	*3.88 day*	*0.08 mil/year*

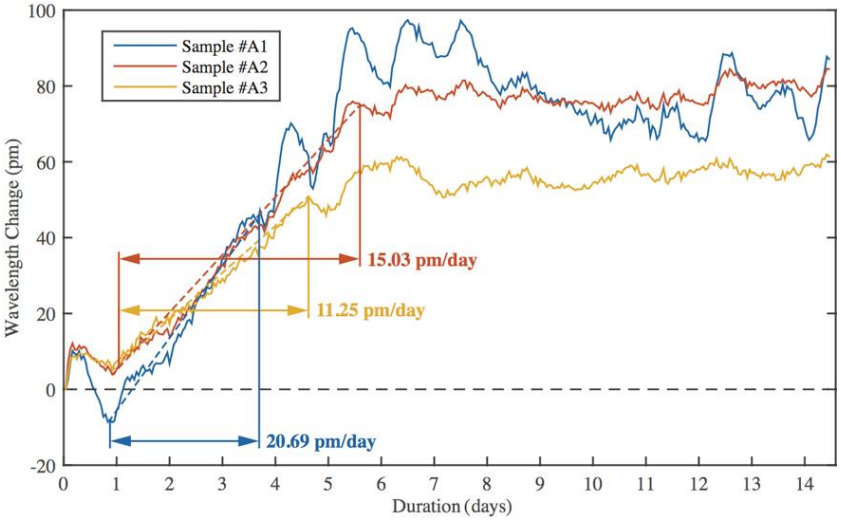

Figure 61. Corrosion rate of three coated samples shown on graph.

Visual inspection results from three tested samples indicated that at second day of the test as seen in Figure 62, corrosion started to be found on Sample #A2 and #A3, and at the fifth day, more corrosion could be found on all samples.

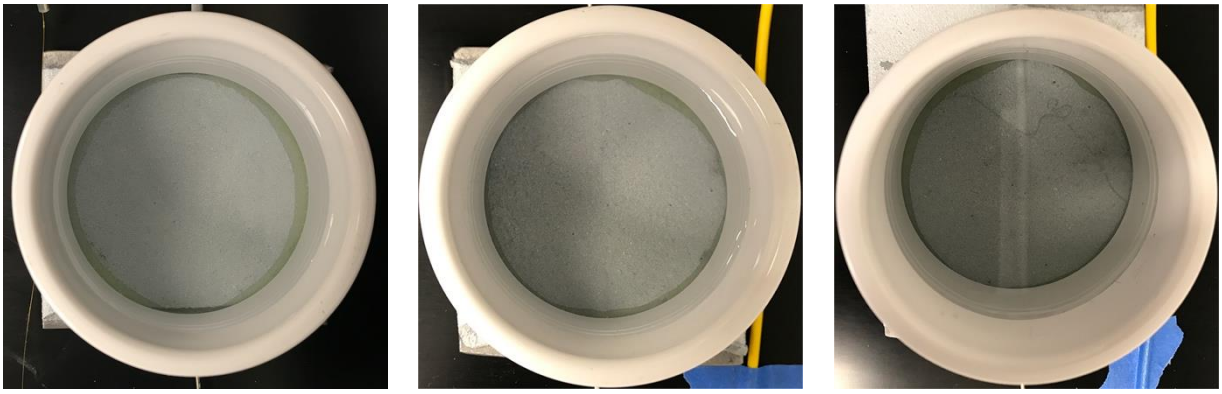

(a_1) Day 0 of Sample #A1 *(a_2) Day 0 of Sample #A2* *(a_3) Day 0 of Sample #A3*

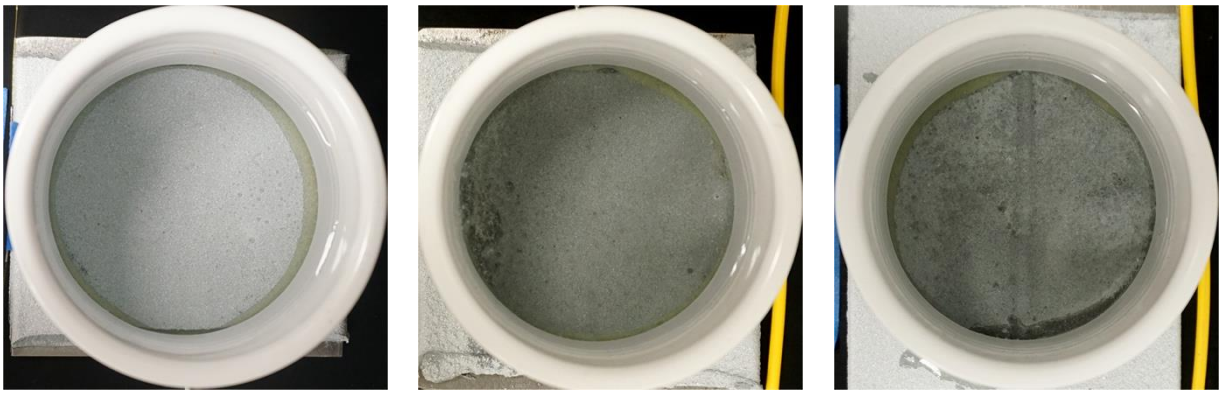

(b_1) Day 2 of Sample #A1 *(b_2) Day 2 of Sample #A2* *(b_3) Day 2 of Sample #A3*

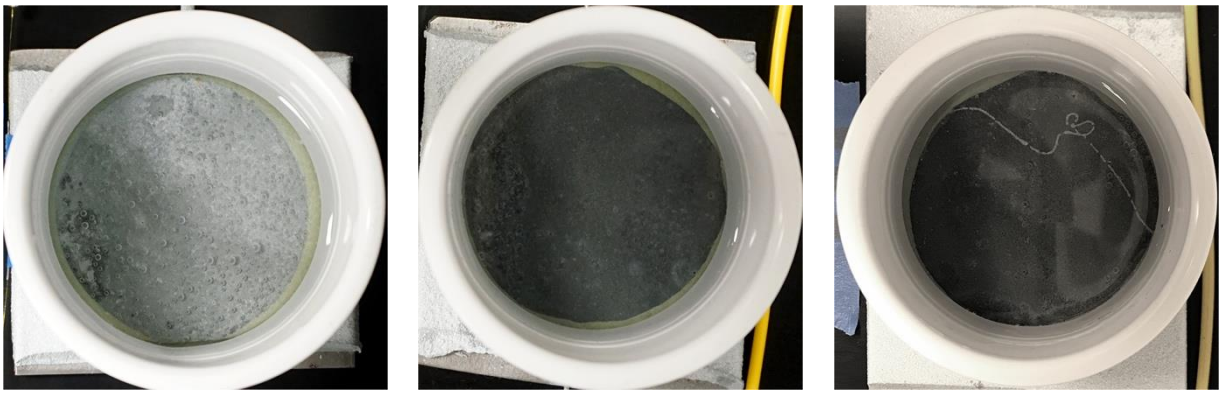

(c_1) Day 5 of Sample #A1 *(c_2) Day 5 of Sample #A2* *(c_3) Day 5 of Sample #A3*

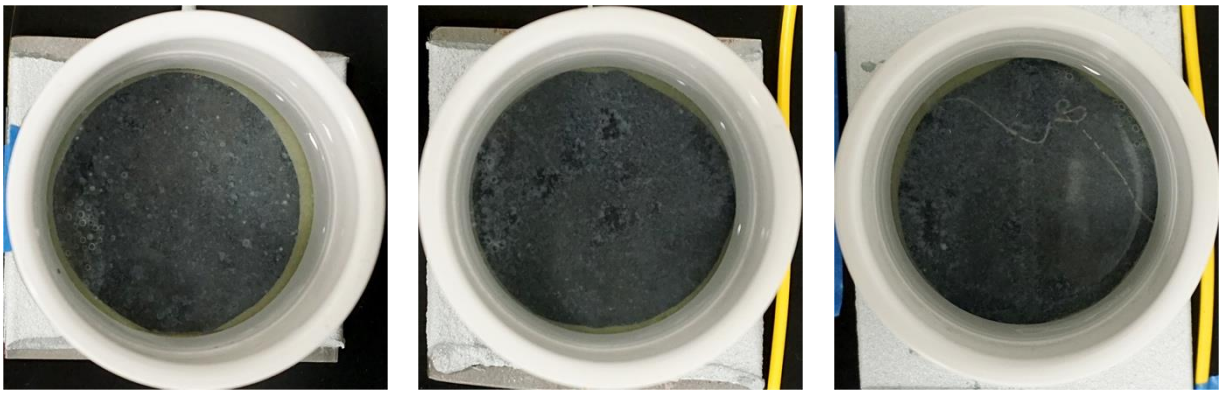

(d_1) Day 14 of Sample #A1 *(d_2) Day 14 of Sample #A2* *(d_3) Day 14 of Sample #A3*

Figure 62. Visual inspection of three samples in accelerated corrosion test.

Taking a close look at the changes of curves in Bragg wavelength of FBG sensors as shown in Figure 61 compared with visual inspection results in Figure 62, reveals that several inner coating cracks could be distinguished by the embedded sensor from Day 4 as shown in Figure 63. After each crack,

the Bragg wavelength of the FBG sensor firstly dropped for a short period, then increased rapidly, suggesting the corrosion rate increased phenomenally, until a new crack was formed and then a new corrosion cycle started. Table 20 showed the corrosion rate of Sample #A1 before each coating crack.

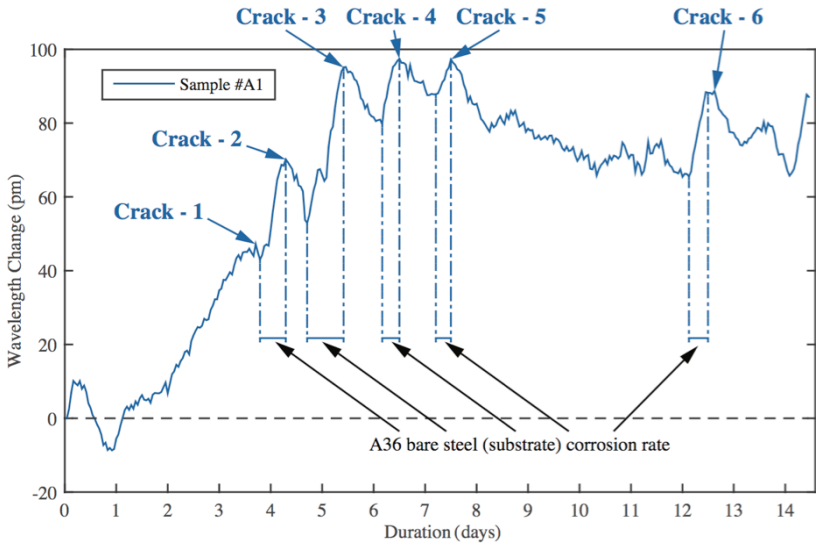

Figure 63. Change of wavelength curves in FBG sensor due to existence of the cracks.

Table 20. Corrosion rate after micro crack formation in hard coating.

Corrosion event	*Initial point for corrosion rate calculation*	*End point for corrosion rate calculation*	*Interval between initial point and end point*	*Wavelength Change Slope*
Sample #A1 at Crack # 2	*44.22 pm (92 hrs)*	*68.69 pm (101 hrs)*	*0.38 day*	*0.44 mil/year*
Sample #A1 at Crack #3	*52.93 pm (113 hrs)*	*94.00 pm (129 hrs)*	*0.67 day*	*0.42 mil/year*
Sample #A1 at Crack # 4	*79.76 pm (148 hrs)*	*97.38 pm (156 hrs)*	*0.33 day*	*0.36 mil/year*
Sample #A1 at Crack # 5	*87.79 pm (173 hrs)*	*97.25 pm (180 hrs)*	*0.29 day*	*0.22 mil/year*
Sample #A1 at Crack # 6	*65.54 pm (291 hrs)*	*88.41 pm (299 hrs)*	*0.33 day*	*0.47 mil/year*

Results from Table 20 indicated that the corrosion rate was drastically increased after formation of cracks in the coating from 0.22 mil/year to 0.47 mil/year. Compared with the initial corrosion rate in Table 19, the fact that Table 20 showed a higher corrosion rate could suggest a combined effect from the coating and its substrate after the occurrence of micro cracks.

From Figure 63 and Table 19, we could find the three tested samples with wire arc Al-Zn hard coating had very consistent performance on accelerated corrosion test. Their calculated corrosion rates were very close (ranging from 0.08 mil/year to 0.14 mil/year with a standard deviation of 0.03 mil/year), which are showing an overall better corrosion resistance compared with the Al-Bronze (Sulzer Diamalloy 1004) hard coating coated by HVOF technique (average: 0.50 mil/year) tested previously.

3.2.2 System Integration in Soft Coatings

Followed by the theoretical study performed in Section 3.2, the concept was further extended to fiber optical sensors embedded in soft coating. The relationship between corrosion rate and the strain induced by corrosion products could be described as follow:

$$\mathrm{CR} = K\frac{d\varepsilon}{dt} \tag{12}$$

In Equation (12), K is a parameter related to the coating material and thickness. Ideally, since the theoretical model of the corrosion assessment system would remain in same formation regardless of the change of coating material, even if soft coating instead of hard coating is used in the system, the formula used for calculating corrosion rate from collected strain data of fiber optical sensors would not change. However, a new calibration process is needed for getting correct K parameter. A corrosion test performed on the system with fiber optical sensor embedded in soft coating was carried out to validate this concept.

A36 structure steel was used as base material in the corrosion test, and layer of epoxy (Duralco 4461) was applied on surface of the base material as soft coating. Fiber optical sensor was located between base material and soft coating. After the soft coating layer was fully cured, a PVC pipe with a diameter of 2 inch was fixed on top of the location of sensor by Loctite heavy duty epoxy then filled with 3.5wt% NaCl solution to create corrosive environment for sensing area. To accelerate the corrosion process, a crack on soft coating was made 1 mm besides the sensor, as shown in Figure 64. The crack allows NaCl solution pass through soft coating much faster.

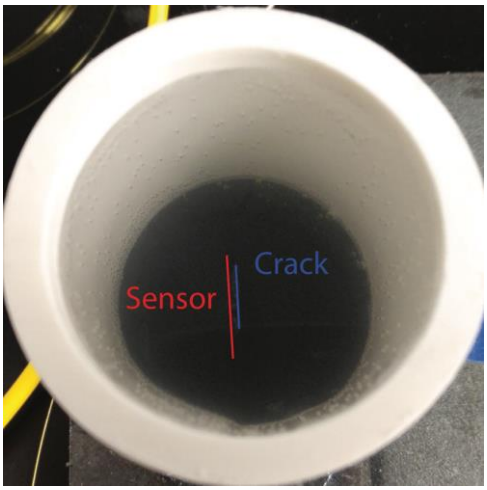

Figure 64. Corrosion experiment set up for steel plate sample with soft coating (Sample #1).

The experiment was finished in 13 days, as a stable strain level was observed after an increase and a decrease were observed in the first 3 days. Figure 65 shows the test results of Bragg wavelength changes versus test time obtained from the embedded fiber optical sensor for the sample.

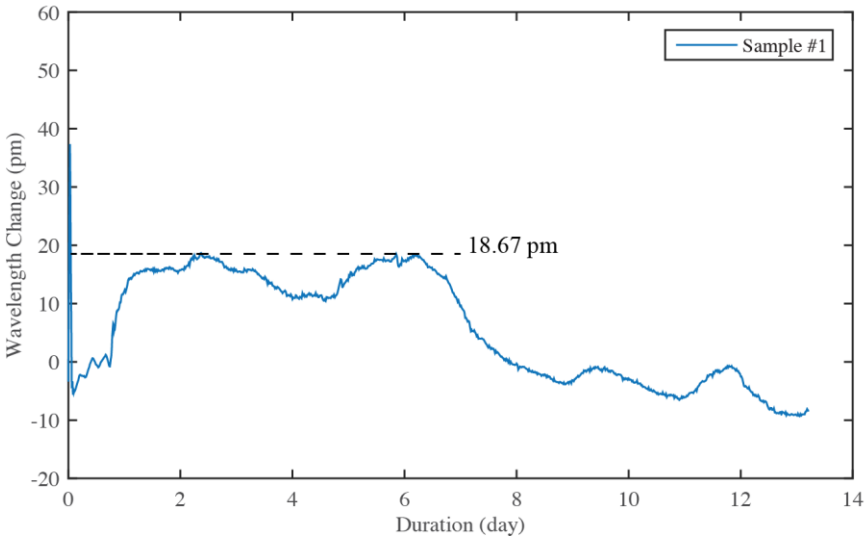

Figure 65. Bragg wavelength change curve of Sample #1.

It can be observed from the Bragg wavelength changes in Figure 65 that highest wavelength change was reached on the second day at 18.67 pm. The wavelength kept staying at same level for 4 days, then started to drop at the day 6. This wavelength change trend indicated the corrosion type should be a pitting corrosion (localized corrosion), and the visual inspection results as showed in Figure 54 to support this inference.

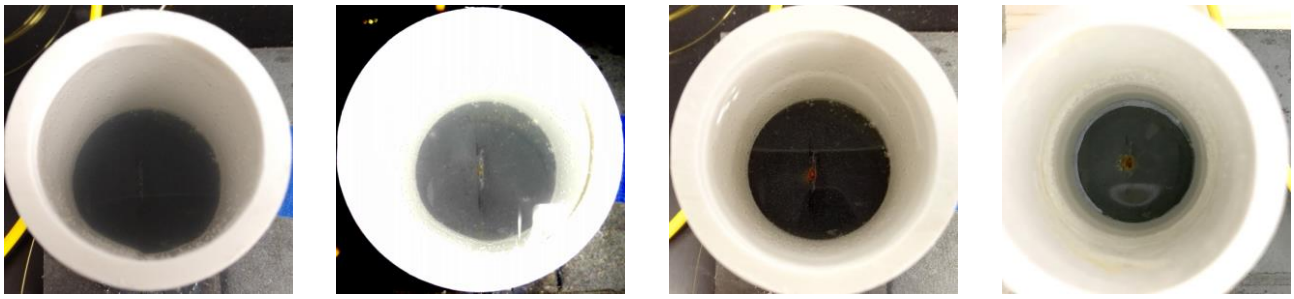

(a) Day1 *(b) Day 2* *(c) Day 3* *(d) Day 6*

Figure 66. Visual inspection of Sample #1.

Figure 61 indicates the Bragg wavelength change rate between the lowest and highest is 10.76 pm/day. Comparing to the data from last chapter, which is 35.19 pm/day as bare steel, it can be seen that the soft coating used in this experiment is able to slow down corrosion process even with a crack on it. However, as crack allows base material expose to oxygen and water in the beginning, the coating failed to protect base material from the initialization of corrosion.

Considering the fact that the selected soft coating was proven to be effective to decelerate and possibly delay the initialization of corrosion process and that fiber optical sensors as expected in soft coatings, an extended study for the corrosion products-adhesive interaction model was performed. In previously proposed model (shown in Figure 67), the correlation between corrosion severity (corrosion rate) and slope of collected data was well explained theoretically and verified by experiment data.

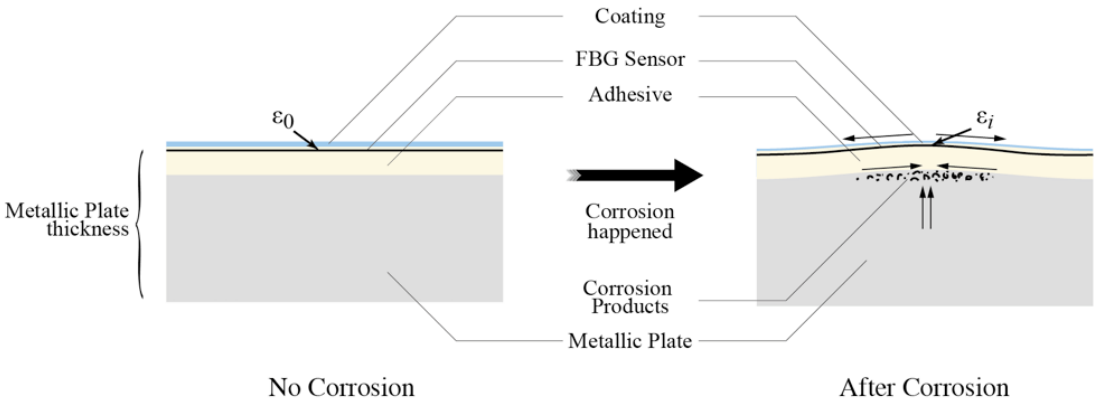

Figure 67. Structural model for corrosion monitoring system.

However, in a typical data collection from embedded corrosion monitoring system during experiments as presented in Figure 68, the previously proposed model fails to interpret the quasi-stable section (noted by blue arrow) following the initial wavelength increase (noted by grey arrow).

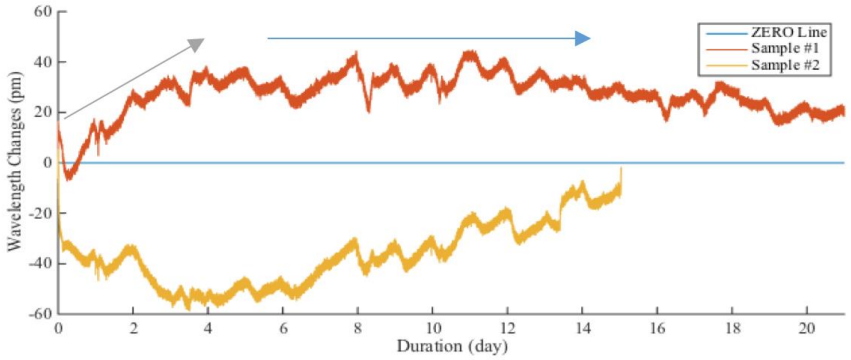

Figure 68. A typical data set collected from embedded sensors.

In order to better understand the further development of corrosion, modification of proposed theoretical model is required proposing 2D development of corrosion as shown in Figure 69.

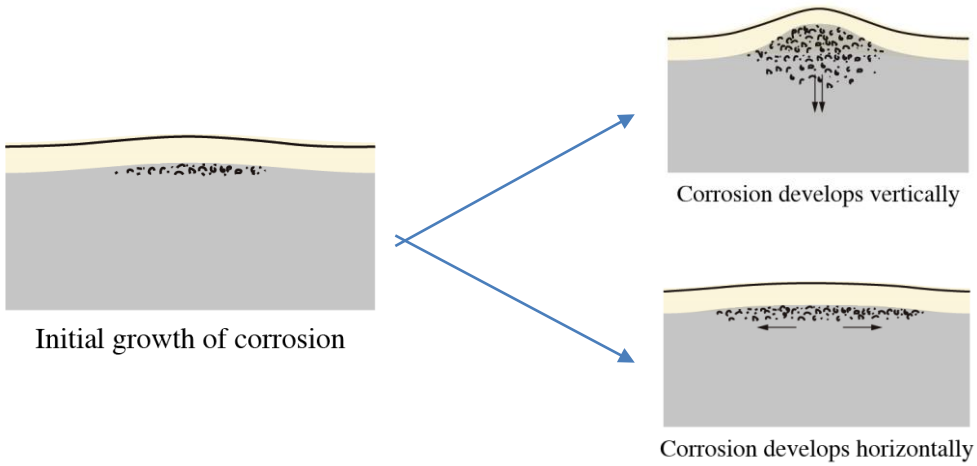

Figure 69. Improved theoretical model for corrosion monitoring system.

The modified model for the growth of corrosion will be divided into two parts: i) vertically developed corrosion induced strains; and ii) horizontally developed corrosion induced strains. In previously proposed model, only the strains induced by vertically developed corrosion was considered.

Simulation results in Figures 70 (a, b) showed that the simulation results using ANSYS software with considering only vertical pressure induced by corrosion on the embedded sensor. It ends up with infinite increase in wavelength over time, which does not correspond to the experiment results.

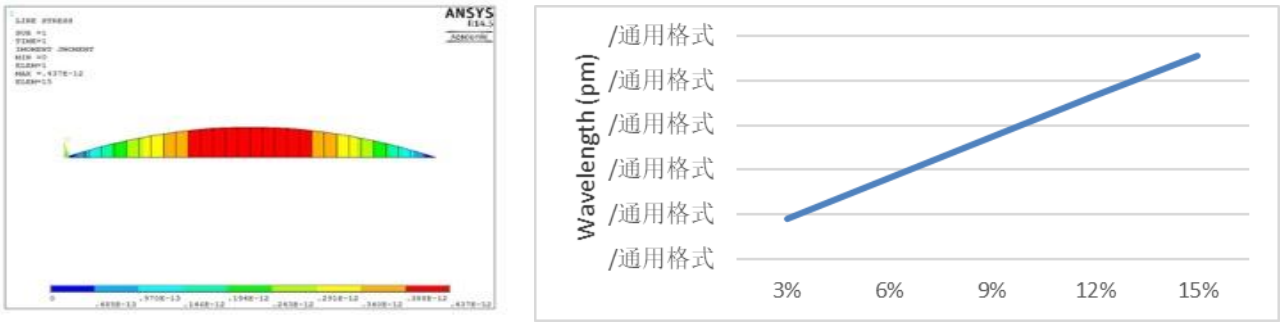

(a) Strain distribution *(b) Strain vs sensor wavelength changes*

Figure 70. Simulation result for model considering only vertically developed corrosion.

Apart from vertically developed corrosion, horizontally developed one could also influences the horizontal range of corrosion that sensor can detect in addition to the amount of strains that sensors could detect. Figure 71 illustrates an image after corrosion experiment on a sample with embedded fiber optic sensor. It can be clearly seen that when the corroded length exceeds the sensor length, only partial of corrosion products directly contribute to the strain value detected by FBG sensor.

Figure 71. Photo showing corrosion developed beyond the length of FBG sensor.

Figure 72 exhibits simulations using ANSYS taking to the account only horizontally developed corrosion indicating that will the horizontally growth of the corrosion would also cause adhesive detach from base metal in lengthened range in addition to corrosion product production, which further results in strain release. This contributes to the decrease of center wavelength change in embedded sensors.

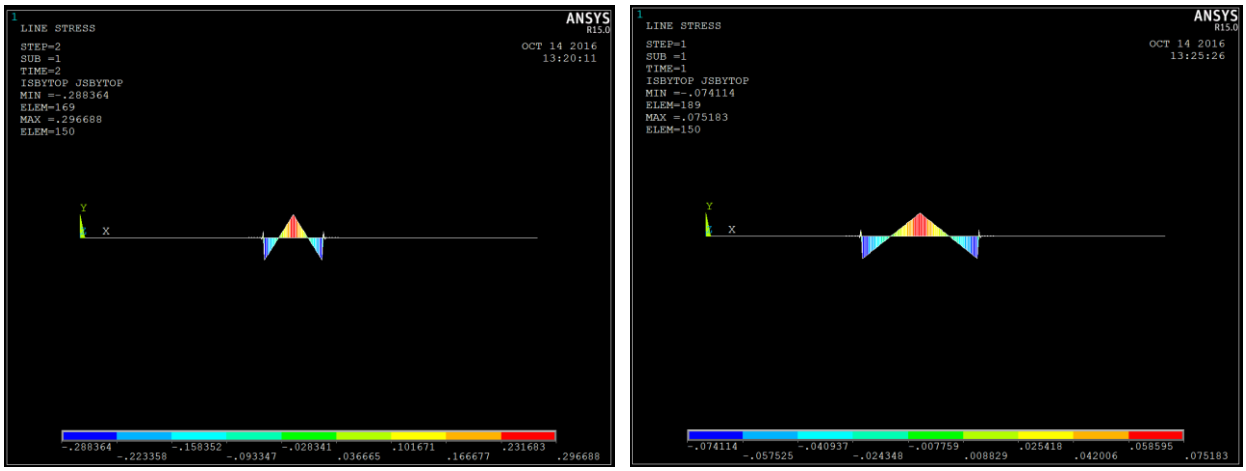

(a) *(b)*

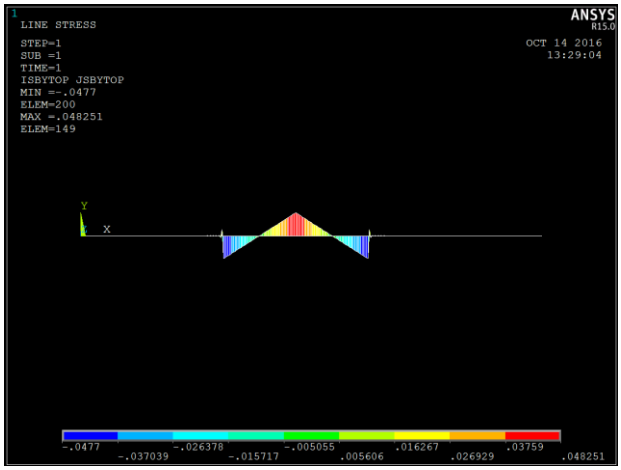

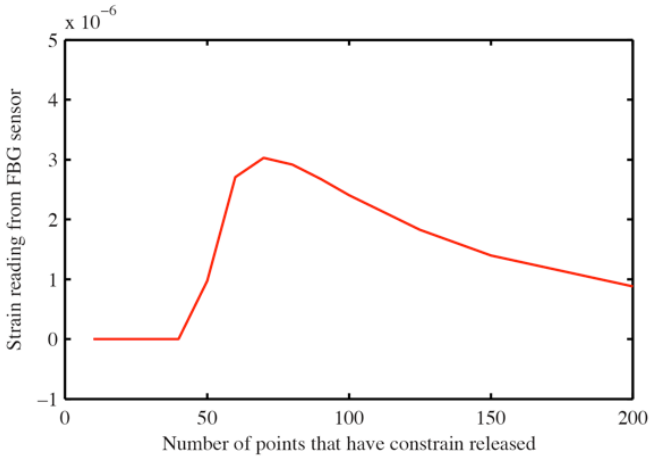

(c) *(d)*

Figure 72. Simulation result for model considering only horizontally developed corrosion, Strain distribution with corrosion < FBG length (b) Strain distribution with corrosion = FBG length, (c) Strain distribution with corrosion > FBG length, and (d) Strains on FBG vs horizontal corrosion.

Both vertically and horizontal developed corrosion effects were considered to explain fully for the corrosion process on embedded FBG sensors. Figure 73 illustrates the simulation results with both vertically and horizontal developed corrosion effects considered. The simulation results showed very close trend when compares to the experimental data (also shown in Figure 73), proving that modified model well represents the actual corrosion progress under the coating of a practical situation. Thus, the modified theoretical model with both horizontal and vertical corrosion considered will be used in corrosion assessment.

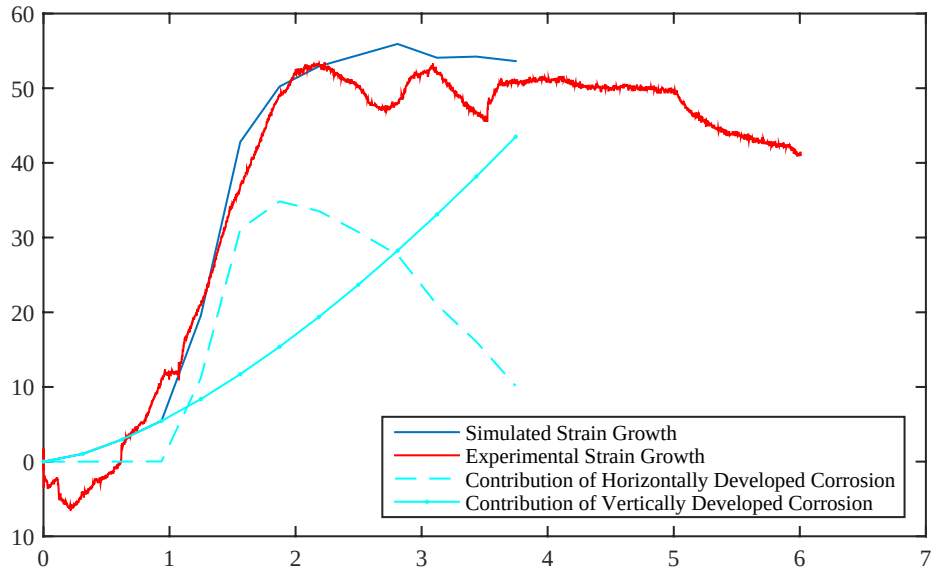

Figure 73. Simulation result considering both vertically and horizontally developed corrosion.

Three more samples with soft coatings were prepared and accelerated corrosion tests were conducted on them in this quarter (shown in Figure 74 and Figure 75).

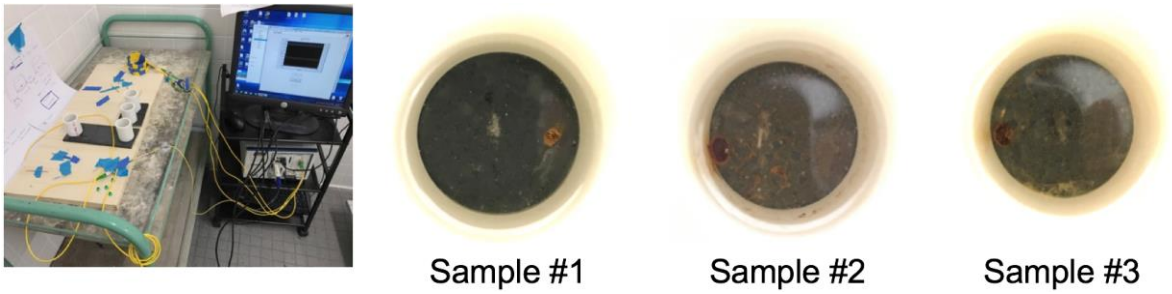

Figure 74. Accelerated corrosion test on three samples with soft coating (Photos of samples taken on the 7th day as test started).

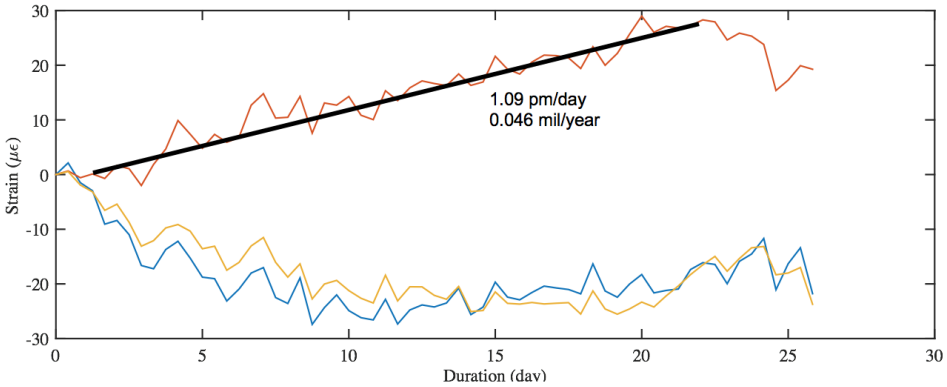

Figure 75. Data collected from embedded corrosion monitoring system.

In previous part, an accelerated corrosion test was also conducted on a sample with soft coating and a pre-made flaw on applied soft coating to shorten the corrosion initialization. The reported corrosion rate of it was 10.76 pm/day. From Figure 63, it could be seen that without any flaw the soft coating can lower the corrosion rate furthermore to 1.09 pm/day. As no significant corrosion has developed on top of the sensor, the accelerated corrosion test is still ongoing as the day this report been drafted.

3.2.3 Comparison between Soft Coating and Hard Coatings

For soft coating, Figure 76 shows the data collected from embedded corrosion monitoring system together with the data collected from the temperature compensation sensor. Figures 40 ~ 43 show the visual inspection results of all the samples on Day 30, Day 150, and Day 270.

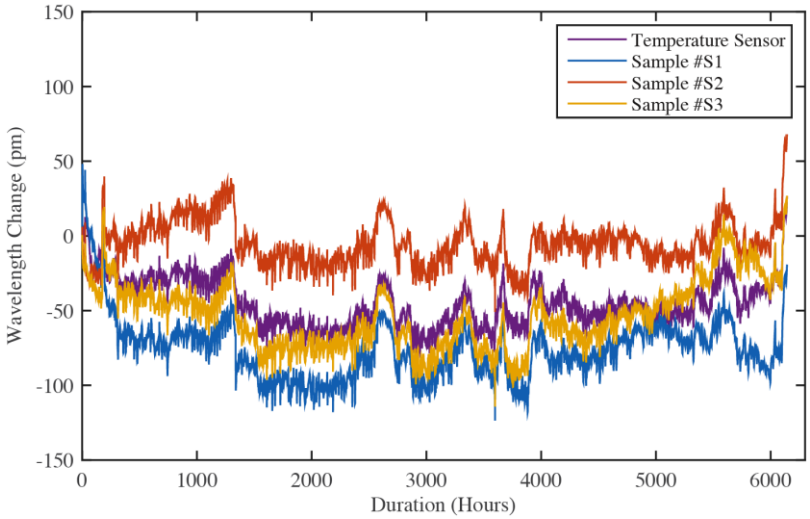

Figure 76. Bragg wavelength changes collected from FBG sensor without eliminating temperature effect and de-noising.

Figure 77 presents the monitored data after temperature compensation for all the three samples. It can be found from this figure that in soft coating, the monitored wavelength approaching stable state roughly around 700 hours (29 days) for Sample #S1 and 1000 hours (42 days) for Sample #S2 and Sample #S3. Comparing this result to previous results from accelerated corrosion tests conducted on samples coated with hard coatings as seen in Figure 78, which normally required less than 4 days. It is obvious that the soft coating slowed down corrosion development more efficiently.

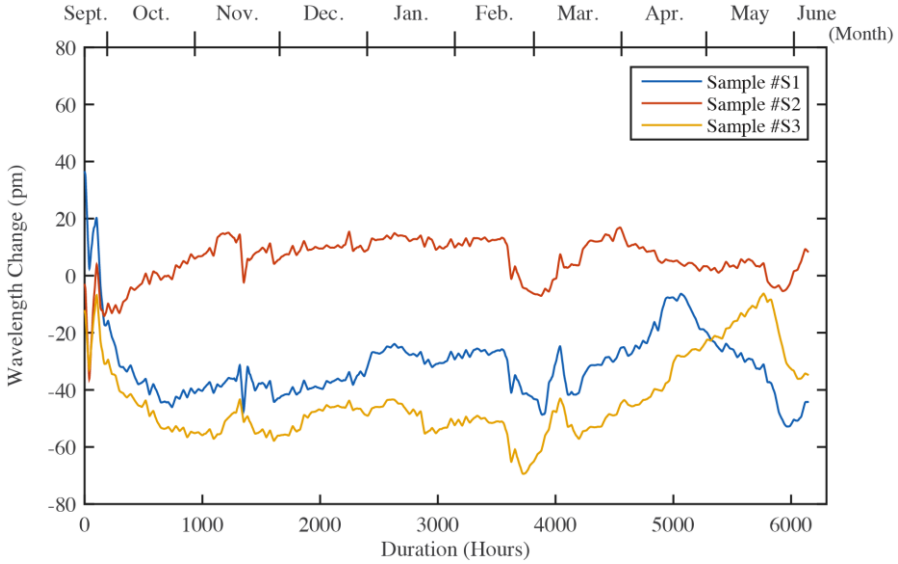

Figure 77. Bragg wavelength changes collected from FBG sensor with soft coating after eliminating temperature effect and de-noising.

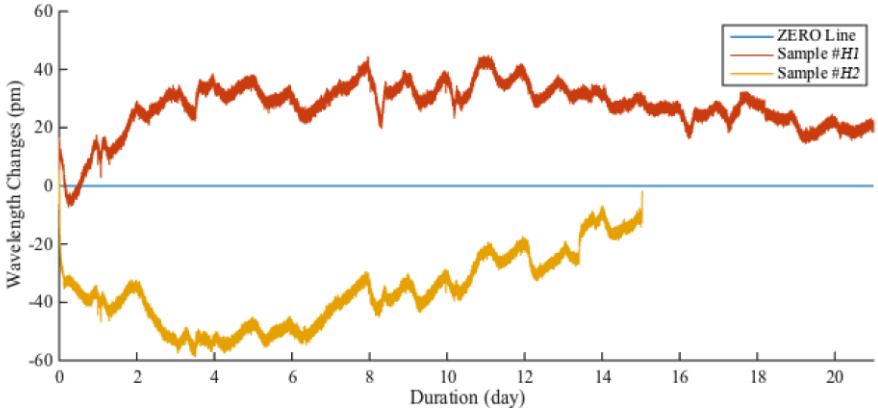

Figure 78. Bragg wavelength changes collected from accelerated corrosion test conducted on samples coated with hard coating.

If the corrosion analysis for soft coating is analyzed based on the findings from the hard coatings as shown in Figure 78 (Sample #H1 was pitting corrosion and Sample #H2 was uniform corrosion), the curve pattern in this figure indicated that Sample #S2 had a pitting corrosion on top of the embedded sensor because its wavelength change increased immediately after corrosion started and Sample #S1 and Sample #S3 would have a uniform corrosion propagation because their wavelength change decreased after corrosion started. However, the visual inspection results from Figures 62 could not support this assumption since all samples showed pitting corrosion development instead of uniform corrosions beneath the soft coatings. This finding means that we cannot use the same assumptions as made for hard coating to analyze the corrosion behavior of soft coatings. Systematic analysis of soft coatings needs to be performed separately for corrosion analysis using embedded sensing systems.

The possible reason for wavelength changes with soft coating having a different pattern even with the same type of corrosion pattern could be a result of very different bonding strength between soft and

hard coatings. In a hard coating with high bonding strength, when a pitted corrosion occurs, only small portion of coating near the corroded area were detached from base material, resulting in concentrated stress and significant increase of wavelength from the embedded sensors.

On the other hand, soft coatings generally have less bonding adhesion at the coating interface comparing to hard coatings. When pitting corrosion occurred under soft coatings, it was more likely that a relatively larger portion of coating near the corroded area were detached from base material, which is known as a delamination. This phenomenon would first decrease the overall stress level around the embedded sensors, leading to a decrease in wavelength. With the corrosion progressing, it would gradually increase the amount of corrosion products which filled up the free space and increase the overall stress around the embedded sensors. As a result, the center wavelength of the embedded fiber optic sensor would have a decrease followed by an increase as observed in the monitored data. It's worth noticing that the soft coatings normally have lower porosity compared to hard coatings, so corrosion would develop much slower with application of soft coating when there were no external damages. Thus, the wavelength increase was much slower when soft coating is applied. Under soft coating, the center wavelength of sensor embedded in Sample #S1 increased about 20 pm in 4 months,; compared to 40pm changes of center wavelength of sensor embedded in Sample #H2 in 11 days under hard coating as in Figure 78.

This phenomenon could be further confirmed after cracks on top of sensors were intentionally made on each sample on Day 150 (February 20th, 2017) as shown in Figure 79. A decrease on center wavelengths of the embedded fiber optic sensors could be found on Day 150, followed by an increase after 10 days. When crack occurred, there would be more coating delamination, leading to a decrease in center wavelengths of sensors. However, because the cracks broke the barrier between base material and outer environment, the corrosion of the base material would increase and corrosion products would start to fill up the free space beneath the soft coating. As a result, the wavelength of the embedded sensors would increase until the coating was penetrated by the corrosion products, the wavelength change curve decreased again. In the visual inspection result in Figure 12 for hard coatings, it was clear that large portion of soft coatings were delaminated in Sample #S1 (middle part), Sample #S2 (right part), and Sample #S3 (bottom-right part). Clearly, the embedded fiber optic sensors successfully and effectively captured the entire corrosion progress of the steel materials coated soft coatings including the early stage of corrosion, coating delamination progressing, crack initiation, and coating breakage.

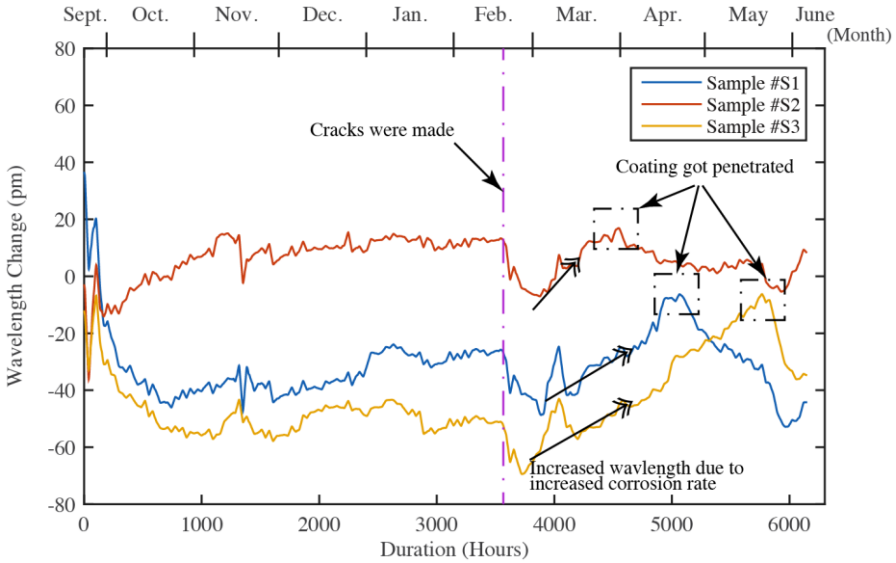

Figure 79. Bragg wavelength changes with detailed time tags marked

3.3 Development of A Model for Corrosion Risk Management (Task 3.3)

Since the most widely applied risk management framework is the relative risk rating with scoring table model. Our main focus of integrating the corrosion monitoring system into this scoring table is the corrosion part of the model, in which the coating condition weighted 15 points out of 100 points. There are four level of coating conditions defined in the model: 1) good, 2) fair, 3) poor, and 4) absence; and each level grants a score of 15 points, 10 points, 5 points, and 0 point, respectively. However, with a data driven corrosion monitoring system that could monitor the coating condition, the score could be granted continuously from 0 to 15 points without given certain levels, as 0 point for no coating and 15 for good coating condition control.

With the corrosion monitoring system, for any given time noted as ti, the corrosion rate (noted as ri) at time ti is known. So the total corroded depth (noted as Dt) in time t could be shown as follow:

$$D_t = \int_0^t r_i dt \tag{13}$$

In coating design, the original coating thickness (noted as Do) is known. So the coating condition score (Scc) in the model could be determined as:

$$S_{cc} = \frac{(D_o - D_t)}{D_o} \times 15 = 15 \cdot (1 - \int_0^t \frac{r_i}{D_o} dt) = 15 \cdot (1 - \int_0^t p_i dt) \tag{14}$$

where $p_i = r_i / D_o$ stands for the percentage corrosion rate to the original coating thickness. When applying the corrosion monitoring system on site, with collected corrosion rate data (ri), the percentage corrosion rate (pi) could be updated time to time, and the coating condition score could be updated in real-time basis. Pipeline operators could see the score dropping from 15 points as the coating being corroded. When pipes got further corroded and the pipeline's overall relative risk rating increased to a certain value, the pipeline operator may choose to take certain action to counter the potential failure, such as renew the coating.

4 Experimental Validation for the Smart Thermal Spraying Coating System (Task 4, Completed)

4.1 Full-size Laboratory Experimental Validation for Soft Coating (Task 4.1 and 4.2)

To validate the capability of proposed corrosion monitoring system, full-size laboratory tests were set up. The pipes used in the test are NPS 6 SCH 40 pipes of 10 inches length, shown in Figure 80.

(a) *(b)* *(c)*

Figure 80. Physical dimensions of the pipes used for future test.

Three types of soil with different compositions and different moisture contents of 20% (Group 1), 30% (Group 2), and 50% (Group 3) will be used to simulate dry, medium, and wet soil condition. The soil samples will be prepared following the U.S. EPA standard 68-C4-0022. In each group of soil, two pipes sections will be buried.

On each pipe, to locate the corrosion on a steel pipe, more than three FBG sensors are estimated to be needed and they should not be on a straight line. Thus, in the full-size pipe test, there were four FBG sensors embedded inside the coatings as shown in the Figure 81. Each FBG sensor is capable of detecting corrosion, and with four FBG sensors, the corrosion will be able to be localized. For each pipe, the exact FBG sensor placing location would be slightly different due to the FBG sensor packaging using the stainless steel tubes. However, all location of the FBG sensors were precisely measured for each pipe in order to accomplish corrosion localization goal. Soft coating would be applied when the FBG sensors were all attached to the pipes with mold.

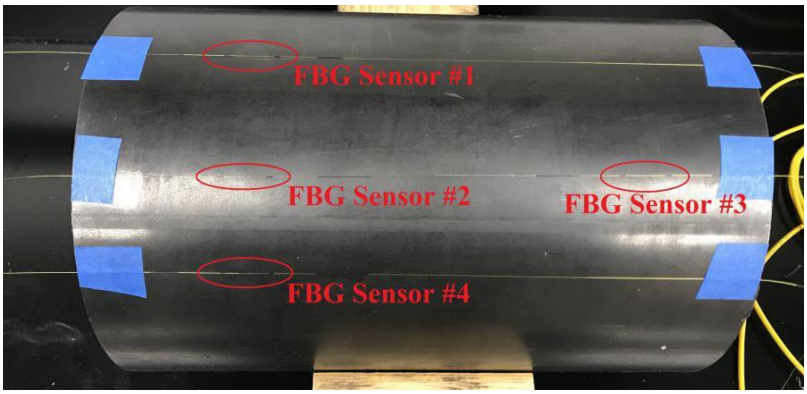

Figure 81. Pipe with FBG sensors installed and ready for deposition of coating.

The blue tapes in Figure 76, were only used for fixing the location of FBG sensors, and since they were on the edge of the pipe and not going to react chemically with other material, they would not affect the testing environment. After applying the soft coating on the surface of the pipe as shown in Figure 82, the pipe was placed in sand with 20% moisture content. The sand fully covered the pipe to simulate the real application environment and the FBG sensors were connected to integrator for data collection as shown in Figure 83.

Figure 82. Steel pipe sample coated with soft coating being put in box filled with sand.

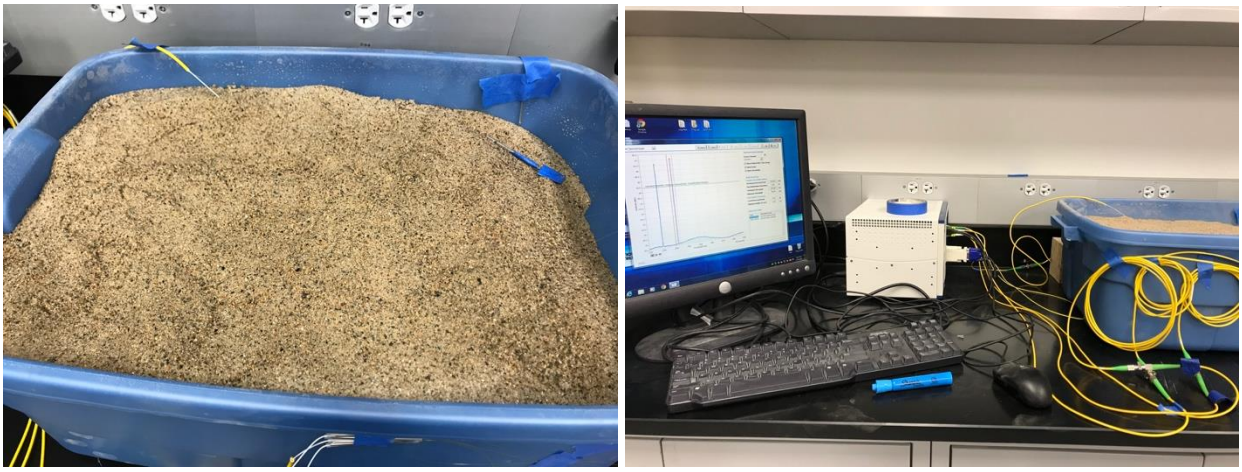

Figure 83. Experiment setup for the steel pipe sample coated with soft coating.

The distances between four embedded sensors were shown in Figures 84 to 86. The distance between Sensor 1 and Sensor 3 is 2 inches, Sensor 2 and Sensor 3 is 7 inches, and Sensor 3 and Sensor 4 is 1.75 inches.

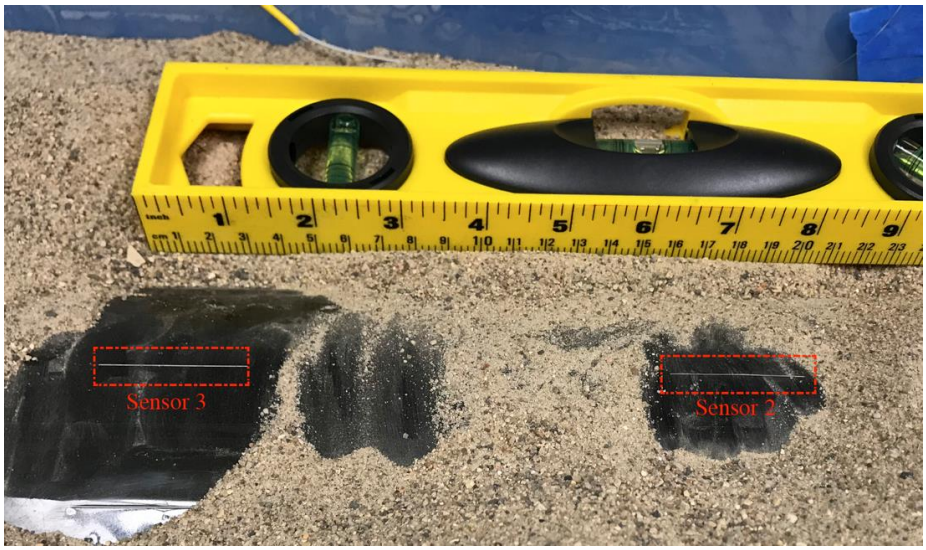

Figure 84. Distance measurement between Sensor 2 and Sensor 3.

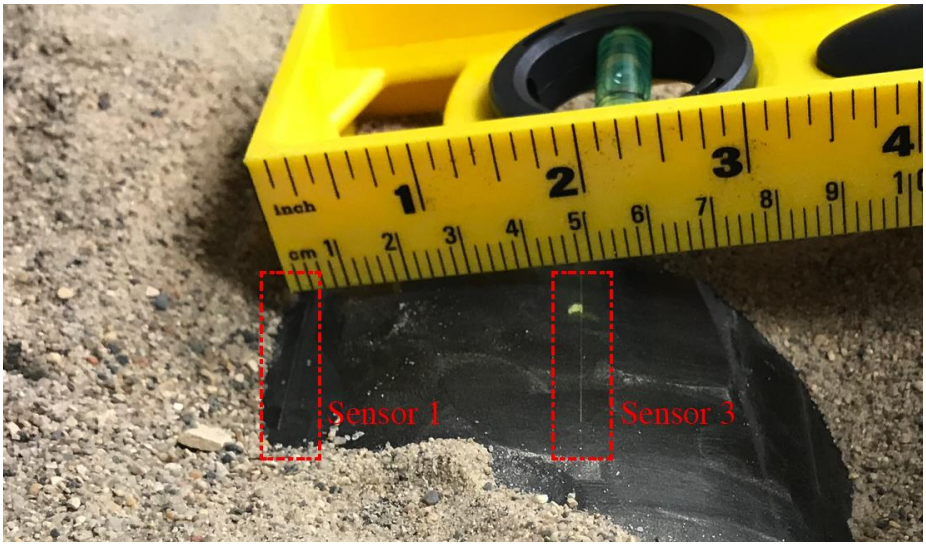

Figure 85. Distance measurement between Sensor 1 and Sensor 3.

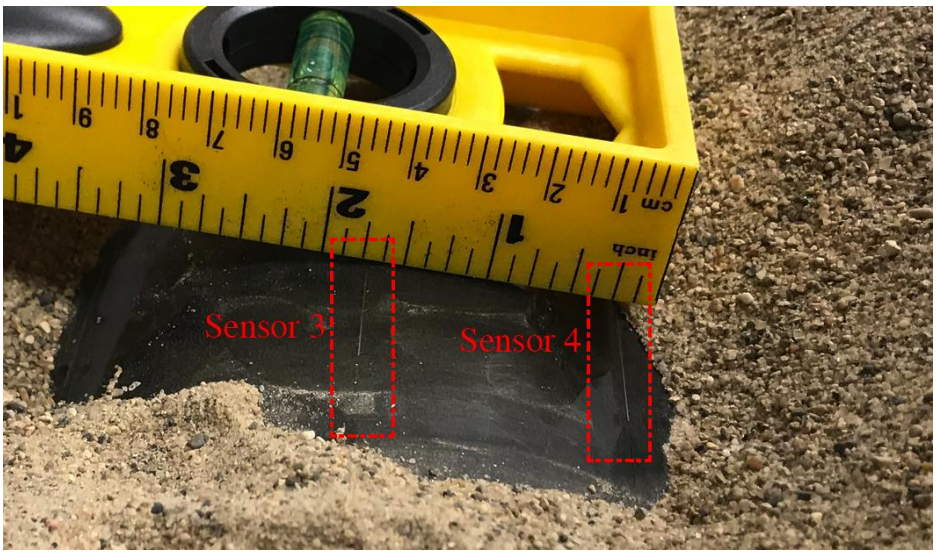

Figure 86. Distance measurement between Sensor 3 and Sensor 4.

Temperature sensor was located in sand to compensate the temperature effect on FBG sensors. Experiment was started at 2:00pm on May 14th, 2018 and ended at 8:00am on Jun 20th, 2018, which had a total duration of 882 hours. In order to accelerate the corrosion and emulate the coating crack damage, a crack of 0.75 inch in length was made near Sensor 3 around 11:00am on Jun 12th, 2018. The crack location was shown in Figures 87 to 89.

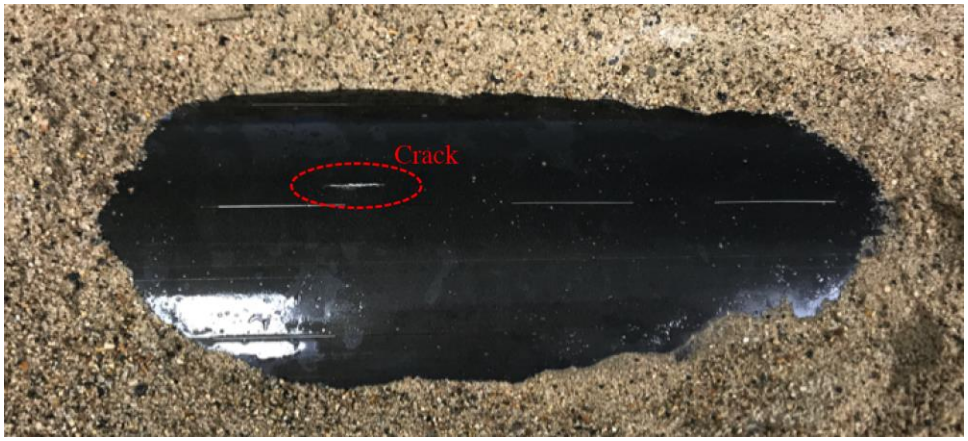

Figure 87. A crack is intentionally made to mock the actual crack happened on coating.

Figure 88. Distance measurement between crack and Sensor 2/Sensor 3.

Figure 89. Distance measurement between crack and Sensor 1/Sensor 3.

The collected data was shown in Figure 90. After temperature compensation, all data collected by the four FBG sensors were has also presented in Figure 91. It can be seen that a dramatic wavelength drop after crack was made on the soft coating, which was expected as our previous results have proven the same effect for multiple times. In addition, after the initial sudden drop the lowest wavelength change value varied from Sensor 1 to Sensor 4. As Sensor 3 had the lowest wavelength change value (highest in absolute value), Sensor 1 and Sensor 4 had the second lowest wavelength change value and their value were close to each other, and Sensor 2 had the highest wavelength change value (lowest in absolute value). All these values variations could serve as an indicator to locate the corrosion. By combining the longitudinal and transverse distance from the crack to each sensor, the straight-line distance between the crack and distance could be found, which are 2.03 inches, 6.01 inches, 1.07 inches, and 2.37 inches for Sensor 1 to 4, respectively. The wavelength changes as shown in the graph, could confirm that corrosion was occurred near Sensor 3. The distances from corrosion to Sensor 1 and Sensor 4 are similar to each other and the corrosion is located further from Sensor 2 due to the lowest absolution wavelength change value.

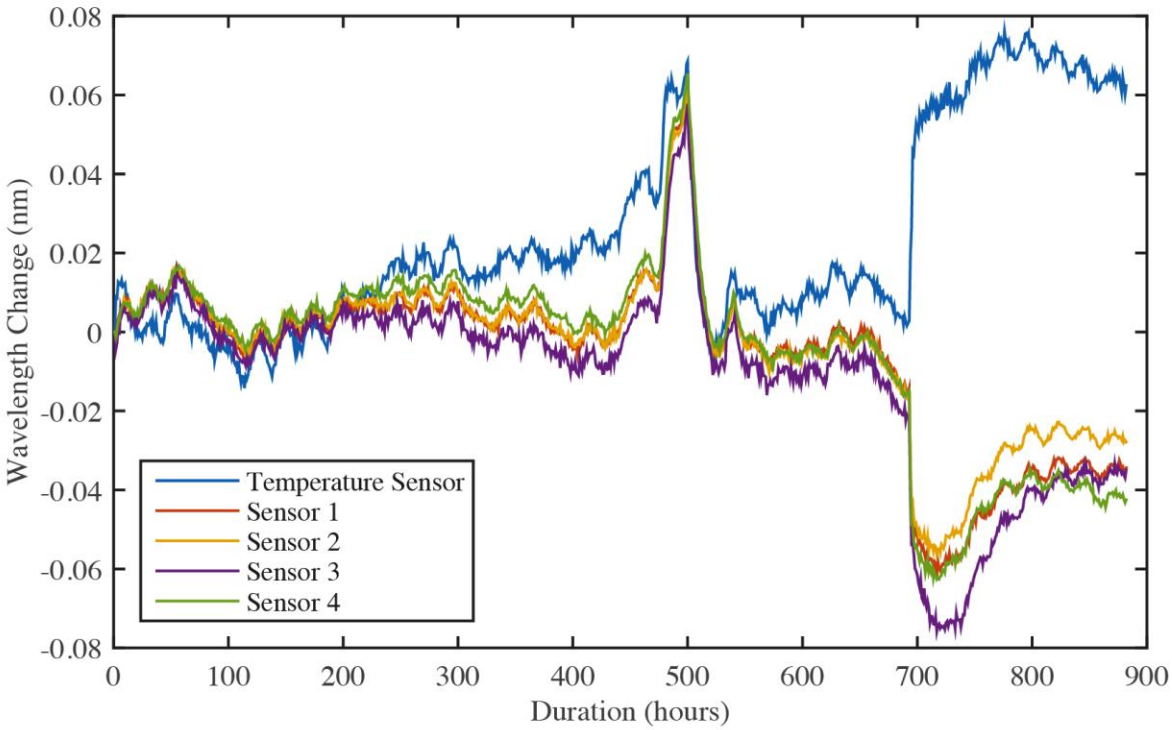

Figure 90. Data collected by FBG sensors before eliminating the temperature effect.

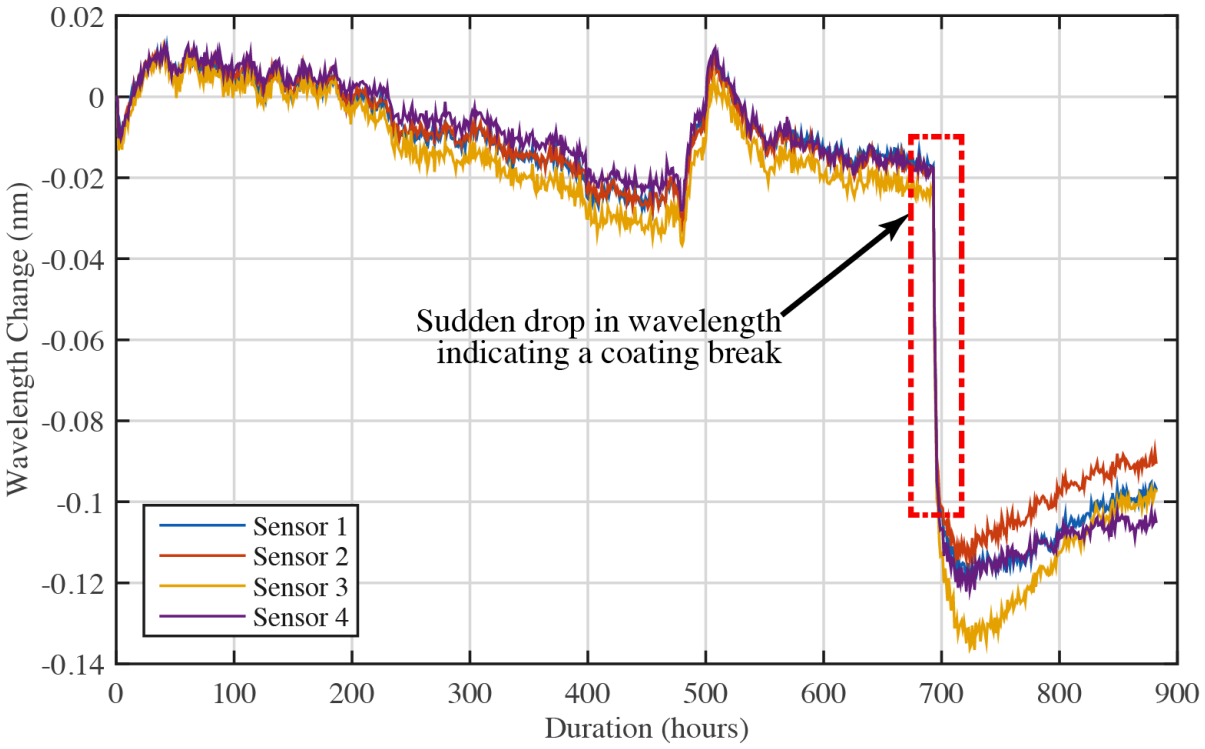

Figure 91. Data collected by FBG sensors after eliminating temperature effect.

In fact, corrosion was initialized from the inner surface of the pipe because of direct burring of the pipe samples under moist sand without isolating their inner surface, as seen on the left of Figure 92 and only a few pitting corrosions were noticed occurred on outer surface of the pipe as seen on the right of this figure.

Figure 92. Corrosion occurred on pipe samples coated using soft coating.

4.2 Full-size Laboratory Experimental Validation for Wire Arc Spraying Al-Zn Coating and Multiple Layer Coatings (Task 4.1 and 4.2)

Four full-size pipe samples were prepared for wire arc sprayed Al-Zn coating. Two samples were coated using wire-arc sprayed Al-Zn coating and one sample were coated using wire arc sprayed Al-Zn coating sealed by epoxy. For all the three samples, three FBG sensors were embedded in the coating of each sample. The distance between two sensors was 2.5 mm away from each other. Figure 93 shows the Al-Zn wire arc coated pipe samples. The coating was uniformly distributed on the outer surface of the pipe. The three sensors had wires connecting the sensors to the integrator from the top. Figure 94 shows the pipe sample coated by wire arc sprayed Al-Zn coating sealed by epoxy which is soft coating as multiple-layer coating.

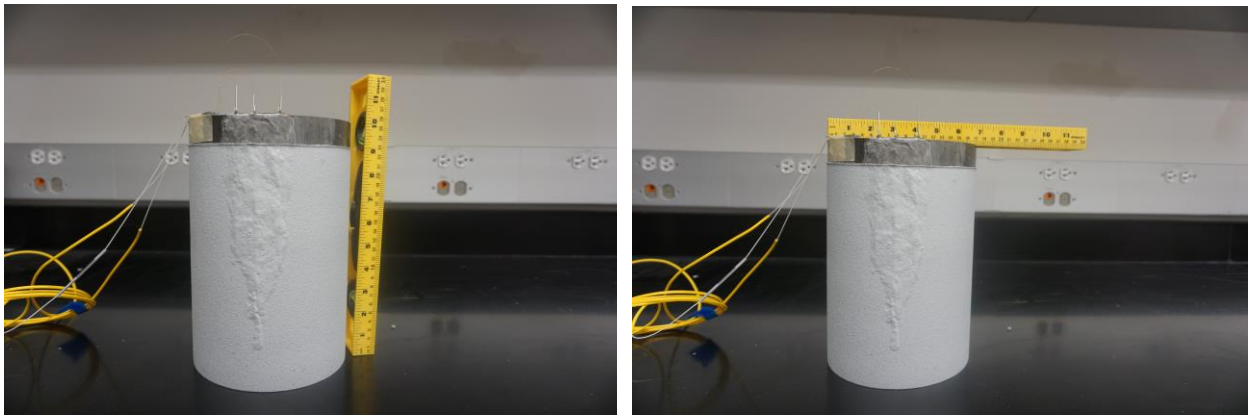

Figure 93. Pipe samples coated by wire arc sprayed Al-Zn coating.

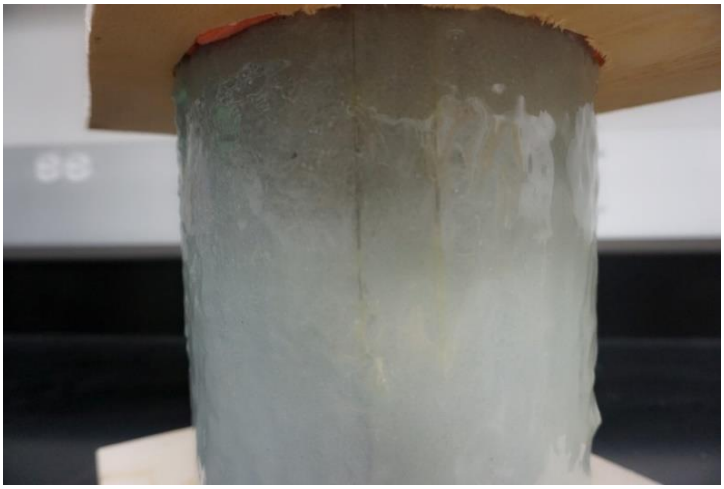

Figure 94. Pipe samples coated by multiple-layer coating with wire arc sprayed Al-Zn coating sealed by epoxy

To isolating the inner surface of the pipe from the surrounding moist soil to prevent any internal corrosion, the coated pipe samples were isolated by two wood board so that the soil could only be in contact with the outer surface of the pipe samples as seen on the left figure of Figure 95. The two wood boards were 25161 mm^2 wooden plates which were cut to fit into the size of the boxes to hold moisture sands. The circular hole on each wooden plate had a diameter a little larger than that of pipes. The pipe sample was placed through two parallel wooden plates. There was no uncoated area between those two wooden plates to make sure that whole testing sections were fully immersed in the moisture sand as seen in the fight figure of Figure 96. The gaps between pipes and wooden plates were filled with epoxy as shown in Figure 97. The prepared pipe samples were then placed inside a box for testing as shown in Figure 98.

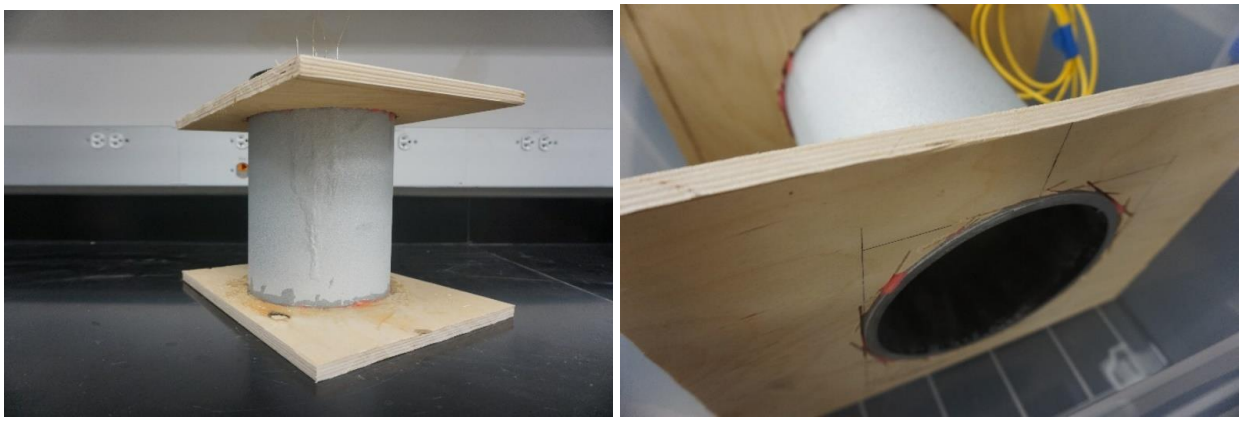

Figure 95. Coated pipe samples with wood board for isolating moisture soil from internal corrosion

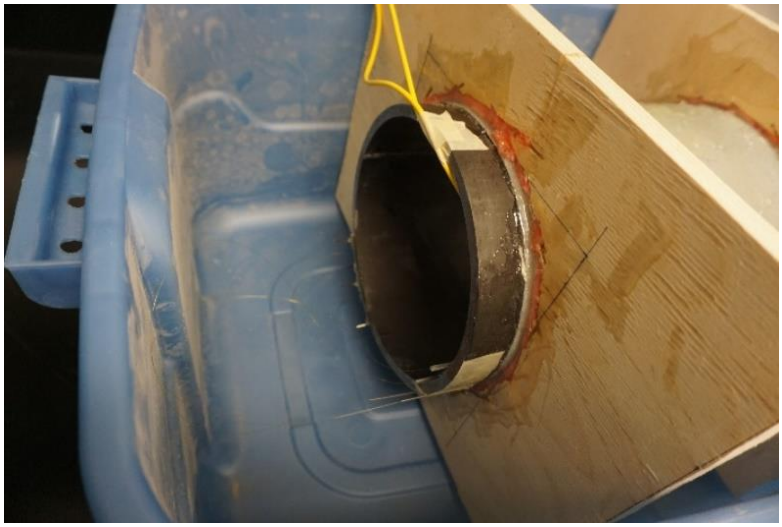

Figure 96. The gaps filled with epoxy.

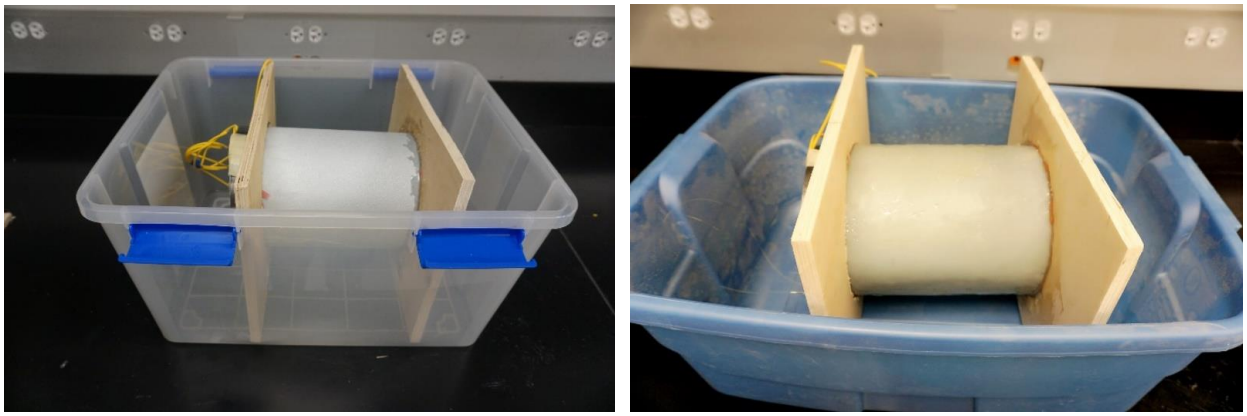

Figure 97. Pipe samples placed inside boxes for testing (left: wire arc sprayed Al-Zn coating, right: multiple-layer coating).

After placing pipes inside the boxes, they were completely covered by sand with 20% moisture content to simulate the underground environments where pipes are buried. Figure 98 show the final test setup, which the testing section of the pipe samples were fully buried under 20% moisture content sand.

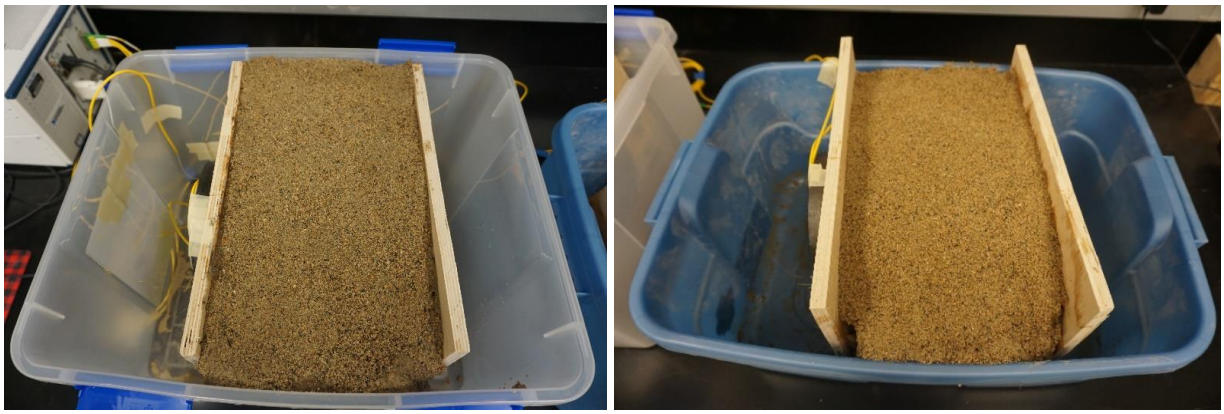

Figure 98. Final experiment set-up.

Temperature sensor was located in the same environment as samples to compensate the temperature effect on FBG sensors. Experiments were begun at 7:15pm on August 10th and ended on Nov 15th 2018 so that it can cover a longer duration of time for potential occurrence of some corrosion. Figure 99 shows the data collected.

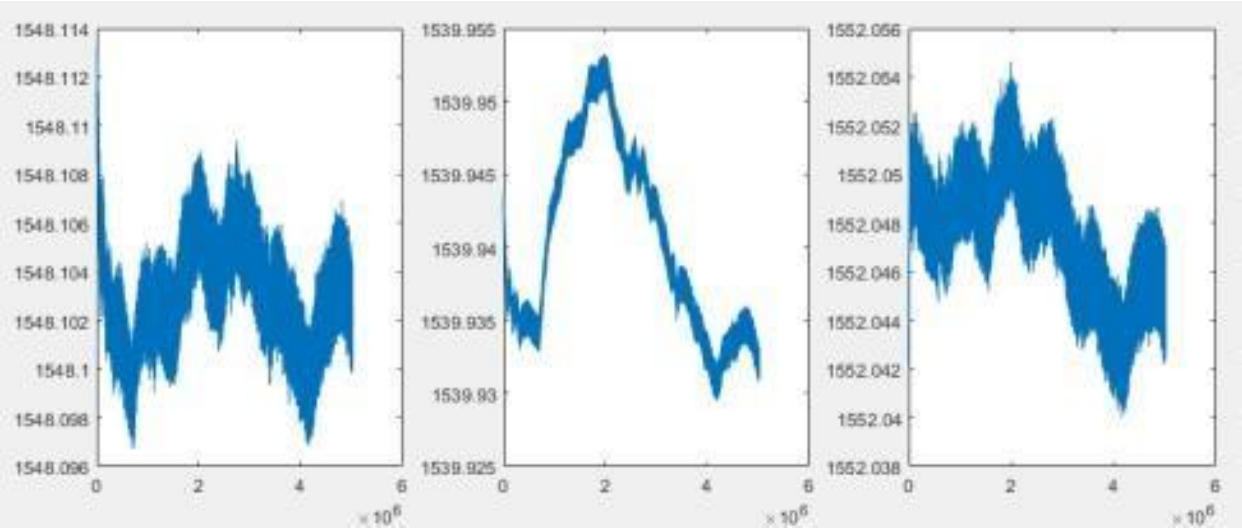

Figure 99. Data collected by FBG sensors.

5 Conclusions

Based on the report above, all the objectives aligned in the proposal were completed as detailed below:

1) The design criteria of thermal spraying coatings were studied through material selection, coating thickness and environmental conditions, sealing approaches, improvements in cathodic protection, and cost optimization. Wire arc and cold sprayed Al-Zn coatings were selected due to their superior mechanical property and corrosion resistance when compared to HVOF Cu and Al-Bronze coatings.
2) The in-line inspection sensor networks inside the coating to quantitatively assess the corrosion mitigation performance of the thermal spraying coating system were developed using embedded FBG sensors;
3) The performance of the developed coatings for corrosion mitigation was investigated using full-size laboratory experiments with various soil conditions;
4) Six graduate students (including four Ph. D. students and two master students) and two undergraduate students participated in this project. Among those students, two Ph. D. students were graduate with dissertations based on this project and got full-time jobs in related areas.

References

1. AWWA C203-97 and Addendum C203a-99, “Coal-Tar Protective Coating and Linings for Steel Water Pipelines – Enamel and Tape – Hot Applied,” AWWA, Denver, CO., 1997-1999
2. S. W. Guan, “100% Solid Rigid Polyurethane Coatings Technology and Its Application on Pipeline Corrosion Protection,” ASCE Journal of Pipelines, Vol. 1, pp.56-165, 2003
3. G. Munger and L. D. Vincent, “Corrosion Prevention by Protective Coatings,” Second Edition, NACE International, Huston, TX, 1999
4. AWWA C213-96, “Fusion-Bonded Epoxy Coating for the Interior and Exterior of Steel Water Pipeline,” AWWA, Denver, CO., 1996
5. AWWA C222-99, “Polyurethane Coatings for the Interior and Exterior of Steel Pipelines and Fittings,” AWWA, Denver, CO., 1999
6. P. Fauchais and A. Vardelle, Thermal Sprayed Coatings Used Against Corrosion and Corrosive Wear, Published by Intech, New York, USA, 2012

7. S. Kuroda and J. Kawakita, " Marine Exposure Tests of Thermal Sprayed Coatings in Japan," Thermal Spray 2003: Advancing the Science & Applying the Technology, (Ed.) C. Moreau and B. Marple, Published by ASM International, Materials Park, Ohio, USA, pp. 343- 352, 2003
8. F. J. Antunes, V. R. S. Sá Brito, I. N. Bastos, and H. R. M. Costa, "Characterization of FeCr and FeCoCr Alloy Coatings of Carbon Steels for Marine Environment Applications," Applied Adhesion Science, Vo. 1, No. 3, pp.1-10, 2013
9. J. Brodar, "Zinc Metallizing Protects Dam after 20 Years," Journal of Protective Coatings and Linings, pp. 49-55.D, 1995
10. Tordonato, Laboratory Evaluation of Metalized Coatings for Use on Reclamation Infrastructure, Bureau of Reclamation, Technical Service Center, Denver, Colorado, Technical Memorandum No. MERL-2012-1, May 2012
11. F. Azarmi and Y. Huang, "Composite Self-sensing Thermal Sprayed Coatings for Pipeline Corrosion Prevention and Mitigation," USDOT PHMSA, Contract No. DTPH56-13-H-CAAP05, Project #509, 10/01/2013-12/15/2015.
12. John A. Beavers and Neil G. Thompson. External corrosion of oil and natural gas pipelines. ASM Handbook, volume 13C, Corrosion: Environments and Industries, 2006.
13. Mark Yunovich and Steven Waters. External Corrosion Direct Assessment for Unique Threats to Underground Pipelines. Final Report of Pipeline and Hazardous Materials Safety Administration US Department of Transportation Washington, DC, November 2007.
14. PD6484: 1979 Commentary on Corrosion at Bimetallic Contacts and Its Alleviation, British Standards Institution.
15. Chattopadhyay R., (2001) Surface Wear: Analysis, Treatment, and Prevention (pub.) ASM Int. Materials Park, OH, USA, 307 p.
16. Davis J. R. (ed.) (2004) Handbook of Thermal Spray Technology (pub.) ASM Int. Materials Park OH, USA.
17. Corrosion guide, Book by Erich Rabald, 1951.
18. Material Selection for Corrosion Control, S. L. Chawla, R. k, Gupta, 1993.
19. X. Campaignolle, M. Meyer, F. Bernard, S. Karcher and S. Gastaud. Organic Coatings Aging Consequences On Under CP Buried Pipelines Corrosion Protection -Simulated Defects. NACE 2004; paper No. 04036.
20. C. Manfredi and J.L. Otegui. Failures by SCC in buried pipelines. Engineering Failure Analysis 2002; 9: 495–509.
21. Kamimura and H. Kishikawa. Mechanism of Cathodic Disbonding of Three-Layer Polyethylene-Coated Steel Pipe. Corrosion Science 1998; 54; No. 12.
22. Shiwei William Guan, Nick Gritis, Adam Jackson, and Peter Singh. Advanced onshore and offshore pipeline coating Technologies. China International Oil & Gas Pipeline Technology (Integrity) Conference & Expo, 2005.
23. Chriss Alliston, Jim Banach, and Joe Dzatko. Extending pipe life. World pipelines, Nov/Dec, 2002
24. Hydrogen Embrittlement: Prevention and Control, By Louis Raymond, Issue 962.
25. Pressouyre, G. M. in Current Solutions in Hydrogen Problems in Steels, C. G. Interrante and G. M. Pressouyre, Eds., American Society for Metals, Metals Park, OH, 1982, pp. 19-34.
26. ISO/DTR 20491, Fundamentals of Hydrogen Embrittlement in Steel Fasteners.
27. Handbook of Thermal Spray Technology, edited by Joseph R. Davis, ASM Thermal Spray Society.
28. C. Medkief Jr, A. Niergarth, and W. Parsons, "Risk management technique for design and operation of liquefied natural gas facilities," 1974.
29. C. B. Chapman, "Large engineering project risk analysis," IEEE Transactions on Engineering Management, no. 3, pp. 78-86, 1979.

30. J. F. Mayer, "Planning for minimum oil-spill risk: Estero Bay deepwater terminal and pipeline," in International Oil Spill Conference, 1975, vol. 1975, no. 1, pp. 287-291: American Petroleum Institute.
31. M. Devine et al., "Analysis and management of a pipeline safety information system. Final report," Oklahoma Univ., Norman (USA). Office of Research Administration1974.
32. M. Pate-Cornell, "Risk analysis and risk management for offshore platforms: lessons from the Piper Alpha accident," Journal of Offshore Mechanics and Arctic Engineering. Transactions of the ASME, vol. 115, no. 3, pp. 179-190, 1993.
33. D. J. Hovey and E. J. Farmer, "Pipeline accident, failure probability determined from historical data," Oil and Gas Journal;(United States), vol. 91, no. 28, 1993.
34. P. Haastrup, "Overview of problems of risk management of accidents with dangerous chemicals in Europe," European Journal of Operational Research, vol. 75, no. 3, pp. 488-498, 1994.
35. W. K. Muhlbauer, "Pipeline Risk Management manual 2nd Edition [M]," ed: Gulf Profession Publishing Co, 1996.
36. S. Diller, "Risk assessment and cost-benefit techniques as management tools for oil spill prevention," WIT Transactions on Ecology and the Environment, vol. 27, 1998.
37. K. Cicansky and G. Yuen, "Risk Management at TransCanada Pipelines," in Proceedings, International Pipeline Conference–1, Sponsored by the American Society of Mechanical Engineers, 1998, pp. 9-14.
38. P. O. Gartland and J. E. Salomonsen, "A Pipeline Integrity Management Strategy Based on Multiphase Fluid Flow & Corrosion Modelling," in CORROSION 99, 1999: NACE International.
39. Z. Pingsheng, "Risk management and risk-based inspection for oil and gas pipelines," OGST, vol. 18, no. 2, pp. 13-18, 1999.
40. R. Kulkarni and A. Patwardhan, "Risk management for water and energy pipelines," Journal of occupational accidents, vol. 13, no. 1-2, pp. 121-133, 1990.
41. C. De Waard, U. Lotz, and D. Milliams, "Predictive model for CO2 corrosion engineering in wet natural gas pipelines," Corrosion, vol. 47, no. 12, pp. 976-985, 1991.
42. W. K. Muhlbauer, Pipeline risk management manual: ideas, techniques, and resources. Gulf Professional Publishing, 2004.
43. M. Singh and T. Markeset, "A methodology for risk-based inspection planning of oil and gas pipes based on fuzzy logic framework," Engineering Failure Analysis, vol. 16, no. 7, pp. 2098-2113, 2009.
44. S. M. Lavasani, Z. Yang, J. Finlay, and J. Wang, "Fuzzy risk assessment of oil and gas offshore wells," Process Safety and Environmental Protection, vol. 89, no. 5, pp. 277-294, 2011.
45. A. Tomic, S. Kariyawasam, and P. Kwong, "Effective Consequences Evaluation for System Wide Risk Assessment of Natural Gas Pipelines," in 2014 10th International Pipeline Conference, 2014, pp. V003T12A019-V003T12A019: American Society of Mechanical Engineers.
46. L. Lu, W. Liang, L. Zhang, H. Zhang, Z. Lu, and J. Shan, "A comprehensive risk evaluation method for natural gas pipelines by combining a risk matrix with a bow-tie model," Journal of Natural Gas Science and Engineering, vol. 25, pp. 124-133, 2015/07/01/ 2015.
47. F. Khan, S. Rathnayaka, and S. Ahmed, "Methods and models in process safety and risk management: past, present and future," Process Safety and Environmental Protection, vol. 98, pp. 116-147, 2015.
48. R. G. Mora, P. Hopkins, E. I. Cote, and T. Shie, Pipeline Integrity Management Systems: A Practical Approach. ASME Press, 2016.

49. B. Inanloo, B. Tansel, K. Shams, X. Jin, and A. Gan, "A decision aid GIS-based risk assessment and vulnerability analysis approach for transportation and pipeline networks," Safety science, vol. 84, pp. 57-66, 2016.
50. Y. Guo, X. Meng, D. Wang, T. Meng, S. Liu, and R. He, "Comprehensive risk evaluation of long-distance oil and gas transportation pipelines using a fuzzy Petri net model," Journal of Natural Gas Science and Engineering, vol. 33, pp. 18-29, 2016.
51. K. F. Tiampo, S. McGinnis, Y. Kropivnitskaya, J. Qin, and M. A. Bauer, "Chapter 8 - Big Data Challenges and Hazards Modeling A2 - Michel, Gero," in Risk Modeling for Hazards and Disasters: Elsevier, 2018, pp. 193-210.
52. http://www.lme.com/- London Metal Exchange (2016)
53. Valerie Sauvant-Moynot, Serge Gonzalez, Jean Kittel. Self-healing coatings: An alternative route for anticorrosion protection. Progress in Organic Coatings 2008; 63:307–315.
54. B.R. Hou, J. Zhang, J.-Z. Duan, Y. Li and J.-L. Zhang, Corrosion of thermally sprayed zinc and aluminum coatings in simulated splash and tidal zone conditions, Corrosion Engineering, Science & Technology.
55. Regina M. H. Pombo Rodriguez, Ramon S. C. Paredes, Schereiner H. Wido b, Alfredo Calixto Comparison of aluminum coatings deposited by flame spray and by electric arc spray, Surface & Coatings Technology 202 (2007) 172-179.
56. Min-Su Han, Yong-Bin Woo, Seok-Cheol Ko, Young-Jae Jeong, Seok-Ki Jang, Seong-Jong Kim, Effects of thickness of Al thermal spray coating for STS 304, Trans. Nonferrous Met. Soc. China 19(2009) 925-929.
57. Eric Irissou, Jean-Gabriel Legoux, Bernard Arsenault, and Christian Moreau, Investigation of Al-Al2O3 Cold Spray Coating Formation and Properties, JTTEE5 16:661-668.
58. Weichao Gu, Dejiu Shen, Yulin Wang, Guangliang Chen, Wenran Feng, Guling Zhang, Songhua Fan, Chizi Liu, Size Yang, Deposition of duplex Al2O3/aluminum coatings on steel using a combined technique of arc spraying and plasma electrolytic oxidation, Applied Surface Science 252 (2006) 2927-2932.
59. I. C. Park, S. J. Kim, Cavitation Damage Behavior in Seawater for Al–Mg Alloy Arc Thermal Spray Coating with Mg Content, Acta Physica Polonica A, Vol. 129 (2016).
60. Y. Takeyoshi, S. Takase, Y. Shimizu, M. Sueyoshi, Y. Uchida, Corrosion Protection of Steel by Al-Mg Plasma Spray Coating, 217th ECS Meeting, Abstract #910, The Electrochemical Society.
61. Hong-Bok Choe, Han-Seung Lee, Jun-Ho Shin, Experimental Study on the Electrochemical Anti-Corrosion Properties of Steel Structures Applying the Arc Thermal Metal Spraying Method, Materials 2014, 7, 7722-7736.
62. H. Q. Yang, Z. J. Yao, D. B. Wei, W. B. Zhou, G. X. Yin & L. X. Feng, Anticorrosion of thermal sprayed Al–Zn–Si coating in simulated marine environments, Surface Engineering, (2014) 1743-2944.
63. American Welding Society: 'Corrosion tests of flame-sprayed coated steel: 19-year report; 1974, Miami, FL, American Welding Society.
64. Qiong Jiang, Qiang Miao, Fei Tong, Yi XU, Bei-lei Ren, Zhi-mei Liu, Zheng-jun Yao, Electrochemical corrosion behavior of arc sprayed Al−Zn−Si−RE coatings on mild steel in 3.5% NaCl solution, Trans. Nonferrous Met. Soc. China 24(2014) 2713−2722.
65. Qiong Jianga, Qiang Miaoa, Wen-ping Lianga, Feng Yingb, Fei Tonga, Yi Xua, Bei-lei Rena,Zheng-jun Yaoa, Ping-ze Zhang, Corrosion behavior of arc sprayed Al–Zn–Si–RE coatings on mild steelin 3.5 wt% NaCl solution, Electrochimica Acta 115 (2014) 644– 656.

66. Seong-Jong, Seung-Jun LEE, In-Ju, Seong-Kweon, Min-Su Han, Seok-Ki Jang, Cavitation and electrochemical characteristics of thermal spray coating with sealing material, Trans. Nonferrous Met. Soc. China 23 (2013) 1002-1010.
67. You Wanga, Wei Tian, Tao Zhang, Yong Yang, Microstructure, spallation and corrosion of plasma sprayed Al2O3-13%TiO2 coatings, Corrosion Science 51 (2009) 2924-2931.
68. K. A. Habib, J. J. Saura, C. Ferrer, M. S. Damra, E. Giménez, L. Cabedo, Comparison of flame sprayed Al2O3/TiO2 coatings: their microstructure, mechanical properties and tribology behaviour, Surf. Coat. Technol. 201 (2006) 1436-1443.
69. [E. Celik, I. Ozdemir, E. Avci, Y. Tsunekawa, Corrosion behavior of plasma sprayed coatings, Surf. Coat. Technol. 193 (2005) 297–302.
70. Sugehis Liscanoa, Linda Gila, Mariana H. Staiab, Effect of sealing treatment on the corrosion resistance of thermal-sprayed ceramic coatings, Surface & Coatings Technology 188–189 (2004) 135 – 139.
71. H. C. Chen, Z. Y. Liu and Y. C. Chuang, Degradation of plasma-sprayed alumina and zirconia coatings on stainless steel during thermal cycling and hot corrosion, Thin Solid Films, 223 (1992) 56-64.
72. C. Amaya, W. Aperador, J. C. Caicedo, F. J. Espinoza-Beltrán, J. Muñoz-Saldaña, G. Zambrano, P. Prieto, Corrosion study of Alumina/Yttria-Stabilized Zirconia (Al2O3/YSZ) nanostructured Thermal Barrier Coatings (TBC) exposed to high temperature treatment, Corrosion Science 51 (2009) 2994–2999.
73. M. Campo, M. Carboneras, M. D. López, B. Torres, P. Rodrigo, E. Otero, J. Rams, Corrosion resistance of thermally sprayed Al and Al/SiC coatings on Mg, Surface & Coatings Technology 203 (2009) 3224-3230.
74. Ahmet Gulec, Ozgur Cevher, Ahmet Turk, Fatih Ustel, Fevzi Yilmaz, Accelerated Corrosion Behaviors of Zn, Al and Zn/15Al Coatings on a Steel Surface, Materials and technology 45 (2011) 5, 477–482.
75. S. Kuroda and J. Kawakita, M. Takemoto, Marine Exposure Tests of Thermal Sprayed Coatings in Japan, ASM International, Materials Park, Ohio, USA, 2003.
76. S. Kuroda, J. Kawakita, M. Takemoto, An 18-Year Exposure Test of Thermal-Sprayed Zn, Al, and Zn-Al Coatings in Marine Environment, Corrosion Engineering Section.
77. Hideki Katayama, Seiji Kuroda, Long-term atmospheric corrosion properties of thermally sprayed Zn, Al and Zn–Al coatings exposed in a coastal area, Corrosion Science 76 (2013) 35–41.
78. B.-R. Hou, J. Zhang, J.-Z. Duan, Y. Li & J.-L. Zhang Corrosion of thermally sprayed zinc and aluminum coatings in simulated splash and tidal zone conditions, Corrosion Engineering, 1743-2782.
79. S. Matthews and B. James, Review of Thermal Spray Coating Applications in the Steel Industry: Part 2-Zinc Pot Hardware in the Continuous Galvanizing Line, JTTEE5 19:1277–1286.
80. D. J. Varacalle, Jr., D.P. Zeek, V. Zanchuck, E. Sampson, K.W. Couch, D. Benson, and G.S. Cox, Experimental Studies of Twin-Wire Electric Arc Sprayed Zinc/Aluminum Alloy Coatings, JTTEE5 7:513-520.
81. Lou miao, Lu yufeng, Ma chunlin, Hu yongle, Zhou meng, Yang huan, Study on Corrosion-resisting Properties of High-speed Arc Sprayed Zn-Al Alloy Coating in Caverns, Advanced Materials Research Vols. 399-401 (2012) pp 2072-2078.
82. Barbara A. Shaw, Angela M. Leimkuhler, and Patrick J. Moran, Corrosion Performance of Aluminum and Zinc-Aluminum Thermal Spray Coatings in Marine Environments, American Society for Testing and Materials, Philadelphia, 1987, pp. 246-264.

83. Yuxing Xiaoa, Xinhua Jiang, Yide Xiao, Liangli Ma, Research on Zn-Al15 thermal spray metal coating and its organic painting composite system protection performance, Procedia Engineering 27 (2012) 1644–1653.
84. O. Salas, O. Troconis de Rincon, D. Rojas, A. Tosaya, N. Romero, M. Sanchez, W. Campos, Six-Year Evaluation of Thermal-Sprayed Coating of Zn/Al in Tropical Marine Environments, International Journal of Corrosion Volume 2012, 11 pages.
85. Sheng Hong, Yuping Wu, Wenwen Gao, Jianfeng Zhang, and Yujiao Qin, Corrosion Behavior of Arc-Sprayed Zn-Al Coating in the Presence of Sulfate-Reducing Bacteria in Seawater, JMEPEG (2015) 24:4449–4455.
86. Champagne et al., novel zinc-based alloys, preparation and use thereof for producing thermal-sprayed coatings having improved corrosion resistance and adherence, Patent Number: 4,915,906.
87. S. Schuerz, M. Fleischanderl, G.H. Luckeneder, K. Preis, T. Haunschmied, G. Mori, A.C. Kneissl, Corrosion behavior of Zn–Al–Mg coated steel sheet in sodium chloride-containing environment, Corrosion Science 51 (2009) 2355–2363.
88. K. Bobzin, M. Oete, T. F. Linke and C. Schulz, Corrosion of wire arc sprayed ZnMgAl, Materials and Corrosion 2015, 66, No. 6.
89. Z. Zhu, Y. Liu, B. Xu, Adv. Mater. Res. 2011, 154–155, 1389.
90. C. Commenda, J. Pühringer, Microstructural characterization and quantification of Zn–Al–Mg surface coatings, Material Characterization 61 (2010) 943-951.
91. Liu Kuiren, Ma Pengcheng, Pu Nianwen, Chen Jianshe, Han Qing, Influence of silicon coating on the corrosion resistance of Zn-Al-Mg-RE-Si alloy, Journal of Rare Earths, Vol. 28, Spec. Issue, Dec. 2010, p. 378.
92. Y. Liu, B.-S. Xu, Z.-X. Zhu, X.-B. Liang & Y.-X. Chen, Microstructure and corrosion behaviour of arc sprayed Zn–Al–Mg–RE cathodic protection coatings on steel substrates, International Heat Treatment and Surface Engineering 2009 VOL 3, 1749-5156.
93. Liu Yan, Xu Bin-shi, Zhu Zi-xin, Li Zhuo-xin z, Ma Jie, New pattern Zn-AI-Mg-RE coating technics for steel structure sustainable design, Journal CSUT Vol. 12 Suppl 2 2005.